On the importance of meteorological parameters in processes affecting the chemical composition of the troposphere

Dissertation
zur
Erlangung des Doktorgrades (Dr. rer. nat.)
der Mathematisch–Naturwissenschaftlichen Fakultät
der
Rheinischen Friedrich-Wilhelms-Universität Bonn

vorgelegt von
M.Sc.
Tamara Emmerichs
aus
Moers

Jülich, Februar, 2022

Diese Arbeit ist die ungekürzte Fassung einer der Mathematisch-Naturwissenschaftlichen Fakultät der Rheinischen Friedrich-Wilhelms-Universität Bonn im Jahr 2022 vorgelegten Dissertation von Tamara Emmerichs aus Moers.

This paper is the unabridged version of a dissertation thesis submitted by Tamara Emmerichs born in Moers to the Faculty of Mathematical and Natural Sciences of the Rheinische Friedrich-Wilhelms-Universität Bonn in 2022.

Anschrift des Verfassers: Address of the author:

Tamara Emmerichs
Institut für Geowissenschaften, Abt. Meteorologie
Universität Bonn
Auf dem Hügel 20
D-53121 Bonn

1. Gutachter: Prof. Dr. Andreas Bott, Rheinischen Friedrich-Wilhelms-Universität Bonn

2. Gutachter: Prof. Dr. Dr. h.c. Andreas Wahner, Universität zu Köln

Tag der Promotion: 7. Juli 2022

Erscheinungsjahr: 2022

Contents

Abstract v

1 Introduction 1

2 Theoretical background 5
2.1 The global atmospheric chemistry model ECHAM/MESSy (EMAC) . 5
2.2 Tropospheric ozone and its precursors 14
2.3 Observation data 19

3 A revised dry deposition scheme for land-atmosphere exchange of trace gases in ECHAM/MESSy v2.54 22
3.1 Introduction 22
3.2 Methodology 23
3.3 Summary of the results 25

4 Impact of the revised dry deposition scheme 28
4.1 Changed dry deposition of ozone and OVOCs 28
4.2 Impact on the tropospheric composition 32
4.3 Discussion 36

5 Global modelling of water-radical complexes 38
5.1 Modified kinetics 38
5.2 Simulation results 40
5.3 Discussion 45

6 Global modelling of drought-stressed biogenic isoprene emissions 48
6.1 Model implementation 48
6.2 Simulation results 50
6.3 Discussion 55

7 Summary, discussion and outlook 57

Appendix 62

Bibliography 88

Acknowledgements 105

Abstract

Investigating the interaction of meteorology and chemistry in the troposphere is important for the identification of the processes which drive the evolution of tropospheric composition in a changing climate. It does not only improve the scientific understanding of the troposphere, which plays multiple roles in the Earth's climate. But these investigations also help to advance our predictions of air quality. Accounting for even more realistic meteorological influences on Surface-Atmosphere interactions becomes more desirable in Earth System modelling because global warming leads to more frequent and intense weather extremes. Chemistry-Climate models deliver an essential contribution to this research as they allow covering a wide range of interacting processes whose parametrisations vary in complexity. Thereby, the investigation of tropospheric ozone (O_3) is central, since enhanced O_3 exposure harms humans as well as vegetation. Also, it accounts for a relevant fraction of the radiative forcing. Most importantly, O_3 plays a key role in tropospheric chemistry involving radicals, nitrogen oxides (NO_x=NO+NO_2) and volatile organic compounds (VOC). Its evolution in the troposphere, especially at ground level, also depends significantly on exchange processes with vegetation.

Despite decades of research in this area, Chemistry-Climate models significantly overestimate tropospheric O_3 in the Northern Hemisphere (NH). However, these models generally have an incomplete representation of the O_3 formation and removal processes which are modulated by weather. The atmospheric chemistry model ECHAM5/MESSy (EMAC) used in this study is no exception. This thesis assesses how the inclusion of meteorological dependencies affects tropospheric chemistry and surface exchanges of O_3 and its precursors and ultimately changes the model prediction of tropospheric O_3 in EMAC.

First, dry deposition as a significant sink of trace gases, especially O_3, is considered here. The study focuses on the uptake of trace gases by vegetation, which happens to a considerable extent via the plant's pores (stomata). A roughly equally important uptake pathway has been proposed to be deposition to the wax covering of the leaves (cuticle). The default parameterisation for dry deposition in EMAC is hardly sensitive to local meteorological conditions (e.g., humidity) and barely represent non-stomatal deposition. In this study, a dry deposition scheme including these missing features is developed in EMAC, having an effect on O_3 and its precursors. The new scheme predicts a significant enhancement of trace gas' dry deposition, whose variation with local meteorology generally show more realistic results when compared to site measurements. However, the analysis also identifies the representation of local meteorology as a remaining significant source of uncertainty in dry deposition modelling. Additional model simulations focus on the accurate representation of

tropospheric chemistry by enabling a more complex chemical mechanism and advanced biogenic VOC emissions. This investigation additionally demonstrates the importance of enhanced dry deposition of oxygenated VOCs which are sufficiently soluble to be efficiently taken up by wet surfaces. This additional non-stomatal uptake lowers the burden of many trace gases, ultimately leading to a reduction of the surface O_3 model bias towards measurements. Second, the impact of water vapour forming complexes with peroxy radicals on the O_3 chemistry is explored. The formation of stable complexes affects the reaction kinetics, generally leading to a weaker radical propagation. To assess its global importance, the available kinetic data for three reactions, central to O_3 chemistry, is included in EMAC. Among the modified kinetics, the newly added formation channel of nitric acid (HNO_3) dominates, significantly decreasing NO_x and thus the formation of tropospheric O_3. Accounting for water-radical complexes overall lowers the tropospheric O_3 burden by 47 Tg a^{-1} (12 %) and the discrepancy of EMAC towards observations is significantly reduced. Third, the model representation of isoprene emissions, an important O_3 precursor, is extended with a currently missing dependency on soil moisture. Accounting for the drought stress on isoprene emissions confers a higher model sensitivity to meteorology. Globally, this yields a reduction of the annual emissions by 22 % leading to a decreased O_3 production. Overall, the thesis demonstrates how the inclusion of sensitivities to meteorology improve the model representation of various processes and the simulation of tropospheric O_3.

Zusammenfassung

Die Erforschung der Wechselwirkung zwischen Meteorologie und Atmosphärenchemie ist maßgeblich. Denn so können Prozesse identifiziert werden, die die Entwicklung der chemischen Zusammensetzung in dem sich verändernden Klima bestimmen. Damit wird nicht nur das wissenschaftliche Verständnis der Atmosphäre, die eine vielschichtige Bedeutung im Klimasystem der Erde hat, erweitert. Diese Forschung trägt auch dazu bei, die Vorhersage der Luftqualität zu verbessern. Da die globale Erwärmung zu häufigeren und intensiveren Extremwetterereignissen führt, wird die realistische Berücksichtigung von meteorologischen Einflüssen auf Wechselwirkungen zwischen Land und Atmosphäre in der Erdsystem-Modellierung erstrebenswerter. Chemische Klimamodelle liefern einen wichtigen Beitrag zu dieser Forschung, da sie es ermöglichen, eine große Bandbreite interagierender Prozesse darzustellen. Dabei ist die Untersuchung von troposphärischem Ozon (O_3) zentral, da eine erhöhte Ozonbelastung Menschen und Vegetation gefährdet. Außerdem ist dieses Gas für einen relevanten Anteil der Strahlungsbilanz der Erde verantwortlich. Aber vor allem besitzt O_3 aufgrund seiner hohen Reaktivität eine Schlüsselrolle in der Troposphärenchemie als Oxidationsmittel. Die Chemie involviert hauptsächlich Radikale, Stickstoffoxide (NO_x=NO+NO_2) und flüchtige organische Verbindungen (englisch: volatile organic compounds, kurz: VOC). Zusätzlich hängt die Ozonmenge in der Troposphäre, insbesondere in Bodennähe, signifikant von den Austauschprozessen mit der Vegetation ab.

Trotz jahrzehntelanger Forschung in diesem Bereich überschätzen chemische Klimamodelle troposphärisches O_3 in der nördlichen Hemisphäre (NH) maßgeblich. Die Modelle beinhalten jedoch generell eine unvollständige Darstellung der vom Wetter beeinflussten Ozonproduktions- und Abbauprozesse. Das globale Modell der Atmosphärenchemie ECHAM5/MESSy (kurz EMAC für „Atmospheric Chemistry Model“), welches in dieser Studie verwendet wird, ist dabei keine Ausnahme. Diese Doktorarbeit bemisst, wie die Einbindung von meteorologischen Abhängigkeiten die Troposphärenchemie und die Austauschprozesse von O_3 und dessen Vorläufergasen mit der Erdoberfläche beeinflusst und letztendlich die Vorhersage von O_3 in EMAC verändert.

Als Erstes wird der Prozess der trockenen Deposition, eine wichtige Senke für Spurengase wie O_3, betrachtet. Die Studie legt den Fokus auf die Spurengasaufnahme in der Vegetation, welche zu einem großen Teil durch die Pflanzenporen (Stomata) stattfindet. Ein vergleichbar relevanter Prozess ist die Ablagerung an der Wachsoberfläche der Blätter (Cuticula). Die Standardparametrisierung für trockene Deposition in EMAC ist kaum sensitiv für lokale, meteorologische Bedingungen (z.B. Feuchte) und repräsentiert trockene Deposition außerhalb der Stomata nur

eingeschränkt. In dieser Arbeit wird eine Parametrisierung entwickelt, welche diese fehlenden Eigenschaften beinhaltet. Das neue Schema simuliert eine signifikant, stärkere Spurengasaufnahme durch Pflanzen, dessen Variation mit der lokalen Meteorologie realistische Ergebnisse im Vergleich zu den Stationsmessungen zeigt. Die Analyse identifiziert jedoch die Modelldarstellung der lokalen Meteorologie als eine wesentliche, verbleibende Unsicherheit für die Modellierung von trockener Deposition. Weitere Modellsimulationen sind stärker auf die genaue Darstellung von Atmosphärenchemie ausgerichtet, wofür ein erweiterter Chemiemechanismus und verbesserte VOC Emissionen verwendet werden. Dadurch wird zusätzlich die Bedeutung einer höheren Deposition von oxidierten VOCs, die ausreichend wasserlöslich sind, demonstriert. Denn die Spurengasbelastung wird beträchtlich reduziert, welches schlussendlich die Übereinstimmung von simuliertem, bodennahem O_3 mit den Messdaten verbessert. Zweitens wird der Einfluss von Wassermolekülen, die Komplexe mit organischen Radikalen formen, untersucht. Die Bildung von stabilen Komplexen beeinflusst die Reaktionskinetik, das zu einer generell geringeren Verbreitung von Radikalen führt. Um die globale Signifikanz zu bemessen, werden die aktuell verfügbaren kinetischen Daten von drei für die Ozonchemie zentralen Reaktionen in EMAC eingebunden. Dabei dominiert der Einfluss der neu hinzugefügten Produktion von Salpetersäure (HNO_3), welche signifikant die Produktion von NO_x und folglich von O_3 in der Troposphäre reduziert. Die Berücksichtigung der Radikal-Wasserkomplexe senkt insgesamt die globale Ozonbelastung um 47 Tg a^{-1} (12 %) und verbessert so den Vergleich zu den Messdaten maßgeblich. Darüber hinaus wird die Modelldarstellung von Isoprenemissionen, einem wichtigen Ozonvorläufer, mit der zurzeit fehlenden Abhängigkeit zur Bodenfeuchte erweitert. Die Berücksichtigung von Trockenheit auf die Isoprenemissionen verleiht dem Modell eine höhere Sensitivität zur Meteorologie. Global führt dies zu einer jährlichen Reduktion der Emissionen von 22 %, welches eine geringerer Ozonproduktion zur Folge hat. Schlussendlich legt die Doktorarbeit dar, wie die Einbindung von meteorologischen Abhängigkeiten die Darstellung verschiedener Prozesse und schließlich die Simulation von troposphärischen O_3 mit EMAC verbessert.

1 Introduction

The chemical composition of the atmosphere is determined significantly by meteorology (Porter and Heald, 2019; Tawfik and Steiner, 2013) which has important implications for air quality. In fact, not only the tropospheric chemistry depends on main weather parameters such as temperature (e.g., Pusede et al., 2015) but also the bidirectional land-atmosphere exchange (of trace gases) is linked to the local meteorology (e.g., Ferracci et al., 2020; Fares et al., 2012). These relations become more relevant in the light of climate warming, where projections report an increase of meteorological extremes such as heat waves (Ridder et al., 2022; Hou and Wu, 2016).

Global atmospheric models have been a key tool for the past decades since they allow representing a large variety of processes and their interaction between different subsystems such as the atmosphere and biosphere. This tool helps not only to improve and to evaluate the current scientific understanding of atmospheric processes, tackling air pollution issues. It also allows assessing the impact of specific processes on the atmospheric composition and finally on the Earth system, here, even at a global scale. In this study, several of these interaction processes are investigated employing the global ECHAM5/MESSy Atmospheric chemistry model (Jöckel et al., 2010, EMAC). By being part of international intercomparison projects such as the Chemistry-Climate Model Initiative (CCMI), the model community also contributes to climate research which is transferred ultimately to recommendations for the public and politics. Compared to other models, EMAC stands out with the capabilities of complex atmospheric chemistry involving fully explicit kinetic schemes of multiphase oxidation, which is of particular interest for this study. One important air pollutant is tropospheric ozone (O_3) since high exposure near the surface (Planetary boundary layer: PBL) directly harm humans' health, leading to issues such as reduced lung functions (Fleming et al., 2018). Also, it has a relevant effect on plants damaging the process of photosynthesis, which alters the water-and carbon exchange of plants and ultimately lowers the ecosystem productivity limiting the human nutrition (Fowler et al., 2009). Besides that, O_3 is a relevant short-lived climate forcer. Most importantly, O_3 initiates many photochemical oxidation processes by direct reaction, photolysis and subsequent reactions. Therefore, it is a major oxidant in the troposphere. As the major tropospheric source of the hydroxyl radical (OH), it also determines other greenhouse gases such as methane (CH_4). The abundance near the surface is driven by photochemical production and loss involving radicals, nitrogen oxides (NO_x=NO+NO_2) and volatile organic compounds (VOCs) (Monks, 2005).

In addition, O_3 levels in the troposphere are influenced significantly by dry de-

position, where trace gases are transferred via turbulent movement to the surface depending on the stability of the lowest tropospheric layers. Then, they are removed by vegetation, deposited in the ground or the ocean. This process is important for cleansing the atmosphere and determining the atmospheric budgets of air pollutants in the planetary boundary layer. It accounts for about 20 % of the total O_3 in the troposphere and even drives the diurnal variation of surface levels in rural areas (Young et al., 2018). Also, for O_3 precursor gases such as hydrogen peroxides (HO_x=OH+HO_2) and NO_x (Wesely, 1989) as well as VOCs (Karl et al., 2010) dry deposition is an influential sink, ultimately affecting the oxidation capacity of the troposphere. The importance and the strength of the uptake vary among different surfaces and depends on the physical properties of the trace gas (Wesely, 1989). Efficient uptake of O_3 (Wesely and Hicks, 2000) and biogenic VOCs (e.g., Fares et al., 2012; Karl et al., 2010) happen, in particular, at terrestrial ecosystems where it either occurs through plant stomata or to the wax covering of the leaves (cuticle). For a long time, the research field has considered stomata as the main pathway for dry deposition. But as discussed by Clifton et al. (2020), more recently studies have demonstrated the cuticular and soil deposition as additional significant contributions to vegetation uptake (e.g., Fares et al., 2012; Rannik et al., 2012). As well as the stomatal pathway, the uptake at the ground and cuticle vary with local meteorology (Rannik et al., 2012). Cuticular uptake, in particular, is favoured by humidity (Altimir et al., 2006). But due to missing observations and process understanding, it is often predefined by constants in models (Wong et al., 2019). Model estimates of O_3 dry deposition reveal the biggest variation compared to different processes considered for the tropospheric budget. For O_3, the estimates range from 700 to 1200 Tg a^{-1} with a high uncertainty (Young et al., 2018; Griffiths et al., 2021). Wong et al. (2019) estimate differences of 2-8 nmol mol^{-1} (ppb) in surface O_3 due to discrepancies of dry deposition modelling. Thereby, most differences are attributed to the process representation link vegetation modelling . In particular, the non-stomatal pathway accounts for the variability among models (Hardacre et al., 2015). Also, Wong et al. (2019) have found that the local meteorology contributes significantly to the process uncertainty independent of the surface type-specific biases.

Atmospheric models represent the chemistry by a set of reactions that vary in complexity. The reaction kinetics are derived from theoretical calculations or chamber measurements at different temperature and pressure levels. An evaluation panel[1] collects and reports critically on the latest kinetic and photochemical data for the use by modellers in computer simulations of atmospheric chemistry. The derivation of accurate laboratory kinetic data is crucial, especially for the central atmospheric reactions, which are key in atmospheric transport models (Young et al., 2018). Radical reactions play a crucial role in tropospheric chemistry. They are involved in processes, such as the O_3 formation. Measurement studies show that radicals form complexes with water molecules. This complexation modulates the kinetics and the fate of the related reactions. Water vapour is the third most abundant gas in the troposphere, with the highest amounts near the surface (Buszek et al., 2011, and

[1] `https://jpldataeval.jpl.nasa.gov/`, last access: 3 February 2022

references therein). As warmer air absorbs more water vapour, the concentrations of lower-tropospheric water vapour are estimated to rise with global warming. Observations and models have shown an increase of the global-mean integrated water vapour by 7 % K^{-1} (Held and Soden, 2006; O'Gorman and Schneider, 2009). Since reactions of peroxy and hydroxyl radicals are an essential part of tropospheric chemistry, the formation of water-radical complexes can have significant effects modifying the trace gas budgets of OH and O_3 (Buszek et al., 2011; Butkovskaya et al., 2009). However, the relevant kinetics is not entirely known and is thus only included partially in a simplified way in models as well as EMAC.

An additionally important process, which affects the chemistry and fate of tropospheric O_3, is the biogenic emission of isoprene (C_5H_8). Isoprene is the main biogenic volatile organic compound (BVOC) emitted by plants (Guenther et al., 1995). Isoprene oxidation contributes to O_3 production in urban and suburban regions and impacts the atmospheric levels of the hydroxyl radical (OH), which drives the oxidation capacity of the troposphere (Monks, 2005; Pusede et al., 2015). Observations show that biogenic isoprene emissions mainly occur over tropical forests (e.g. Amazon basin, Indonesia) and to a lesser extent in the Southern US, South East Asia and Europe (Wells et al., 2020). The global distribution estimated with models is generally in agreement with these observations (Weng et al., 2020; Sindelarova et al., 2014) but model estimates span a wide range are highly uncertain. Uncertainties are associated with meteorological driving, land cover data and the used parametrisation (Guenther et al., 2012). According to a satellite-based constraint, models seem to overestimate global isoprene emissions (Bauwens et al., 2016). The here used Model of Emissions of Gases and Aerosols from Nature (MEGAN) is currently applied to estimate BVOCs (Cao et al., 2021). The framework estimates the emission based on measurements which include observed plant emissions varying in response to the past and current weather conditions (e.g. temperature), plant physiology, canopy environment, and leaf age and is capable of representing a large set of VOCs (Guenther et al., 2012). Due to the high uncertainty associated with the current formulation of the emission dependence on soil water status, this is not included in the standard model set-up of EMAC. However, the importance has been demonstrated by multiple measurement studies, such as Pegoraro et al. (2004) and Grote et al. (2009). According to these findings, significantly lower emissions occur during drought conditions. Especially in the light of global warming, where more frequent and intense droughts are predicted (Ridder et al., 2022), accounting for this dependence in global models is considered desirable.

The meteorological sensitivities described above are of significance for the tropospheric composition, especially in the surface layers, as the processes determine the chemistry, emission and deposition of different trace gases. The role of the weather dependencies grows due to the increased occurrence of meteorological extremes. The inclusion in EMAC aims at improved process representations, while the analysis allows assessing the respective role for predicting trace gas budgets such as tropospheric O_3 globally. Therefore, after employing multiple sensitivity simulations, the results for O_3 are compared to observation data of ground-based stations collected

in the frame of the Tropospheric Ozone Assessment Report (TOAR) as well as to satellite retrievals obtained from the Infrared Atmospheric Sounding Interferometer (IASI). Ultimately, an improved understanding of how the tropospheric composition is affected by local meteorology helps to target air pollution and climate issues.

In the following, the thesis divides into six chapters. The employed atmospheric model EMAC, the basics of the tropospheric O_3 chemistry and the observation data used in this study are introduced in Chapter 2. The subsequent Chapter 3 gives an overview of a study, published in the frame of meteorological sensitivities of processes important for tropospheric O_3. The study about the extension of the dry deposition of trace gases aims at a more comprehensive dry deposition scheme in EMAC. The various effects of this modification on the tropospheric composition are assessed in Chapter 4. Next (Chapte 5), the impact of water complexation in radical reactions is investigated. Chapter 6 provides an investigation of isoprene emissions responding to dry soil (drought). The results of the individual studies and analyses are summarised and discussed against the current model performance and general uncertainties in Chapter 7 which closes with an outlook for ongoing and new research projects.

2 Theoretical background

Within this thesis, we conduct global model simulations to investigate the impact of meteorological dependencies on the tropospheric composition. The employed atmospheric chemistry model ECHAM/MESSy (EMAC) is introduced in the following Sect. 2.1. Secondly (Sect. 2.2), the basic O_3 chemistry and budget terms are described. In particular, an overview of the related tropospheric chemistry is given. Finally (Sect. 2.3), the various kinds of the here used measurement data are presented.

2.1 The global atmospheric chemistry model ECHAM/MESSy (EMAC)

The simulations are performed with the ECHAM/MESSy Atmospheric Chemistry (EMAC) model where the Modular Earth Submodel System (Jöckel et al., 2010, MESSy) is coupled with the 5^{th} generation European Centre Hamburg general circulation model (Roeckner et al., 2003, ECHAM5) as the core atmospheric model. A general introduction to ECHAM5 and the MESSy infrastructure are provided in the following.

The core atmospheric model ECHAM5

ECHAM5 is based on the spectral weather prediction model of the European Centre for Medium-Range Weather Forecast (ECMWF, 'EC' $\rightarrow$ first part of the name) and has been developed by the Max-Planck Institute of Meteorology in Hamburg (MPIM, 'HAM' $\rightarrow$ second part of the name). A detailed description can be found in Roeckner et al. (2003). In the horizontal sphere, the basic prognostic variables temperature, divergence, vorticity and logarithmic pressure are described as a truncated series of spherical harmonics (Roeckner et al., 2003). The tracer transport is based on a semi-Lagrangian scheme (Lin and Rood, 1996). The soil is represented as a single bucket governed by rainfall, evaporation, snowmelt, surface runoff and drainage. The field capacity of the soil is prescribed as the maximum soil water content with two-dimensional input data varying in space, calculated for 1 January 1978. In a bucket scheme, the field capacity corresponds to water depths (Hagemann and Stacke, 2015).

Within this thesis, the model applies different resolutions of T42, T63 and T106, which correspond to a grid box size of 310 km (2.8°), 210 km (1.9°) and 125 km

(1.1°). In the vertical, hybrid pressure levels range up to 10 hPa (31 levels) and 0.01 hPa (47,90 levels), whereas the latter one reaches ≈80 km in the middle atmosphere (MA).

The MESSy infrastructure

The Modular Earth Submodel System[1] is a flexible, numerical system that allows linking multiple Earth system components to represent atmospheric chemistry and meteorological processes in a modular framework. The system is structured in four different layers. The first layer (BML) contains an atmospheric core, the atmospheric general circulation model ECHAM5 in this study. Second, the Base Model Interface Layer (BMIL) comprises the MESSy infrastructure connecting the three central functionalities. The Submodel Interface Layer (SMIL) provides the information and data transfer between the BMIL and the submodel' processes, which are included in the Submodel Core Layer (SMCL).

Atmospheric chemistry

Models represent atmospheric gas-phase chemistry by a set of chemical reactions, here described within the MESSy submodel MECCA ('Module Efficiently Calculating the Chemistry of the Atmosphere'). Multiple mechanisms with different complexity can be chosen, which allows matching individual scientific targets. A kinetic preprocessor (KP[4]) performs the numerical integration of a set of ordinary differential equations (ODE) (Sander et al., 2019).

In this study, we make use of two different chemical mechanisms according to the respective purpose of the investigation. First, the EMAC standard is applied. This mechanism used for the Chemistry-Climate Model Initiative (CCMI) contains the basic gas-phase chemistry of ozone, methane and odd nitrogen. This also includes alkanes and alkenes with up to four C atoms but neglects alkynes and aromatics (Jöckel et al., 2016). Second, the larger chemistry of the Mainz Organic Mechanism (MOM, Sander et al., 2019) is used for a couple of simulations aiming at an accurate representation of the tropospheric chemistry, including as many trace gases as feasible. MOM is the most complex chemical mechanism available in MESSy. Besides the basic chemistry of HO_x, NO_x, CH_4 this contains an extensive oxidation scheme for isoprene (Taraborrelli et al., 2009, 2012; Nölscher et al., 2014), monoterpenes (Hens et al., 2014), and aromatics (Taraborrelli et al., 2021; Cabrera-Perez et al., 2016) excluding iodine and mercury chemistry. Overall, MOM represents more than 600 species and 1600 reactions, including 43 primarily emitted VOCs. The reduction of the Master Chemical Mechanism (MCM), which is the source of MOM, however, introduces some uncertainty to the representation of atmospheric chemistry in global models (Whitehouse et al., 2004).

[1] `https://www.messy-interface.org/current/auto/messy_submodels.html`, (last accessed: 18 December 2021)

Table 2.1: List of dynamical MESSy submodels used in this thesis.

Submodel	Description
AEROPT	Aerosol optical properties (Jöckel et al., 2006)
CH4	Oxidation of CH_4 by OH, O(^{1}D), Cl. Feedback to the hydrological cycle[1]
CLOUD	ECHAM5 cloud scheme as MESSy submodel (Roeckner et al., 2006)
CLOUDOPT	Calculation of cloud optical properties (Dietmüller et al., 2016)
CONVECT	Convection parameterisations (Tost et al., 2006b)
E5VDIFF	Land-atmosphere exchange (except for tracers) and vertical diffusion - according to the ECHAM5 code[1]
GWAVE	Hines non-orographic gravity wave routines from ECHAM5[1]
JVAL	Photolysis rates (Jöckel et al., 2005)
ORBIT	Calculation of orbital parameters of the Earth orbit (Dietmüller et al., 2016)
OROGW	Parameterisation of subgrid scale orography (SSO) drag due to low level SSO blocking and orographic gravity wave forcing[1]
QBO	Newtonian relaxation of quasi-biennial oscillation (Jöckel et al., 2006)
RAD	Implementation of the ECHAM5 radiation code (Dietmüller et al., 2016)
SURFACE	The SURFACE submodel is the modularised version of the ECHAM5 subroutines SURF, LAKE, LICETEMP and SICETEMP. It calculates the surface temperatures over land, ice, ocean, lake, and within the soil, soil water content, snow depth, snow melt, glacier depth, runoff, drainage and soil heat flux.[1]
TROPOP	Tropopause and other diagnostics (Jöckel et al., 2006)
VERTEX	Land-atmosphere exchange (except for tracers) and vertical diffusion - alternative to E5VDIFF[1]

In addition, explicit aqueous-phase chemistry is calculated within the SCAVening (SCAV, Tost et al., 2006a) submodel, which is a unique feature of EMAC. In this study, a comprehensive mechanism is used (among the three available) which represents more than 150 reactions including in-cloud HO_x(aq) chemistry and the destruction of O_3(aq) (Jöckel et al., 2016) by a system of coupled ODEs. The uptake and release of gases from cloud and rain droplets follows Henry's law equilibrium and a correction for gas-phase diffusion limitation and the accommodation coefficients. Furthermore, the scheme explicitly represents dissociation and aqueous-phase redox reactions, in contrast to more simplified versions (Tost et al., 2006a). The representation of wet deposition is based on the in-cloud and in-precipitation chemical concentrations for both large-scale and convective clouds.

For obtaining reaction rates from multiple reactions and combining them into a single tracer, the submodels employ a sophisticated tagging system (Gromov et al., 2010). This system allows obtaining detailed tropospheric budgets of tracers. When

Table 2.2: List of additional MESSy submodels used in the chemical set-ups.

Submodel	Description
CCMI set-up:	
AIRSEA	Air-sea exchange of trace gases (Pozzer et al., 2006)
CVTRANS	Convective tracer transport (Tost, 2006)
DDEP	Dry deposition of trace gases and aerosols (see Sect. 2.1)
LNOX	Lightning NO_x production (Tost et al., 2007)
MECCA	Atmospheric chemistry (see Sect. 2.1)
MSBM	Multi-phase stratospheric box model (Jöckel et al., 2010)
OFFEMIS	Prescribed emissions of trace gases and aerosols (Kerkweg et al., 2006b)
ONEMIS	On-line calculated emissions of trace gases and aerosols (Kerkweg et al., 2006b)
PTRAC	Define additional prognostic tracers via namelist (Jöckel et al., 2008)
SEDI	Sedimentation of aerosol particles (Kerkweg et al., 2006a)
SORBIT	Sampling along sun-synchronous satellite orbits (Jöckel et al., 2010)
SCAV	Scavenging and wet deposition of trace gases and aerosol (Tost et al., 2006a)
SCOUT	High-frequency output of model data at the position of stationary observatories on-line (Jöckel et al., 2010)
TNUDGE	Newtonian relaxation of species as pseudo-emissions (Kerkweg et al., 2006b)
TREXP	Tracer release experiments from point sources Jöckel et al. (2010)
MOM set-up[a] :	
BIOBURN	Biomass burning fluxes (see Sect. 2.1)
MEGAN	Biogenic emissions of VOCs (see Sect. 2.1) - alternative to ONEMIS plant emission calculations

[a] additions/alternatives to the CCMI set-up

considering the global O_3 budget, odd oxygen (O_x) is analysed to account for rapid cycling between species of the O_x family, which is defined as:

$$\begin{aligned} O_x \equiv\ & O + O_3 + NO_2 + 2 \times NO_3 + 3 \times N_2O_5 + HNO_3 \\ & + HNO_4 + ClO + HOCl + ClNO_2 + 2 \times ClNO_3 \\ & + BrO + HOBr + BrNO_2 + 2 \times BrNO_3 + PANs \\ & + PNs + ANs + NPs \end{aligned} \tag{2.1}$$

where PANs are peroxyacyl nitrates, PNs are alkyl peroxynitrates, ANs are alkyl nitrates, and NPs are nitrophenols (Rosanka et al., 2021b). The O_x budget is calculated in the PBL and the troposphere taken the respective indices which are calculated within the MESSy submodel TROPOP (see Table 2.1). TROPOP diagnoses the tropopause with two different definitions. For latitudes equatorward of

30°, it is based on the temperature lapse rate according to the WMO definition. Poleward of 30° the tropopause is defined at the iso-surface of 3.5 potential vorticity units (PVU) (Jöckel et al., 2006).

Land-atmosphere exchange

Plants are key players in the water and energy cycle of land-atmosphere coupling, which drives the global climate. They regulate their water and CO_2 household via their stomates which accounts for a large fraction of the evapotranspiration over land. The latent heat flux is calculated based on the Monin-Obukhov similarity theory, which incorporates the stomatal resistance ($R_{stom}(PAR, LAI)$) at canopy level (Schulz et al., 2001). This depends on the photosynthetically active radiation (PAR in [W m^{-2}]) and Leaf Area Index (single-side total area of leaves/needles per area surface, LAI in [m^2 m^{-2}]), parameterised as follows (Ganzeveld and Lelieveld, 1995; Sellers, 1985):

$$R_{stom}(PAR, LAI) = \frac{kc}{\left[\frac{b}{dPAR} ln\left(\frac{d\exp(kLAI)+1}{d+1}\right) - ln\left(\frac{d+\exp(-kLAI)}{d+1}\right)\right]} \tag{2.2}$$

where k=0.9 is the extinction coefficient, c = 100 s m^{-1} is the minimum stomatal resistance and $a = 5000$ J m^{-3}, $b = 10$ W m^{-2} and $d = \frac{a+b\cdot c}{c\cdot PAR}$ are fitting parameters (Sellers, 1985). The parameters derived from site measurements introduce some uncertainty. A more detailed description of the transpiration scheme can be found in Giorgetta et al. (2013). Originally, the LAI in Eq. 2.2 is set to 1 to obtain a the stomatal resistance at leaf level (Ganzeveld and Lelieveld, 1995). The LAI data sets used for the sensitivity studies within this thesis are described in Sect. 2.1. This process (and vertical diffusion) is parameterised in the MESSy submodel VERTEX, which is the current alternative to the default E5VDIFF submodel in ECHAM5/MESSy. VERTEX was branched off by Huug Ouversloot in 2016, who also optimised the code and applied bug fixes. The stomatal resistance value from VERTEX is provided to the submodel DDEP (Sect. 2.1) for the dry deposition calculation.

Trace gas' dry deposition

To estimate dry deposition, the MESSy submodel Dry DEPosition (DDEP) (Kerkweg et al., 2006a) uses the resistance network by Wesely (1989) as commonly applied in Earth system models. This approach, shown in Fig. 2.1, represents the plant-atmosphere-soil system with various resistors, one compartment each, analogous to the transfer of electric power. In contrast to the original work by Ganzeveld and Lelieveld (1995), DDEP only distinguishes four different surface types (land, bare soil/snow, ice, water). The total flux in each model grid box is calculated as the sum of the dry deposition flux at the different surface types. The flux ($f_d(X)$) depends on the trace gas concentration ($C(X)$) and the dry deposition velocity ($v_d(X)$), which consists of the three main resistors describing the surface transfer conditions

(aerodynamic: R_a), the turbulence in the boundary layer (quasi-laminar boundary layer: R_{qbr}) and the uptake at the surface ($R_s(X)$, for each trace gas X).

$$f_d(X) = -v_d(X) \cdot C(X) \tag{2.3}$$

$$v_d(X) = (R_a + R_{qbr}(X) + R_s(X))^{-1} \tag{2.4}$$

$$\frac{1}{R_{s,veg}(X)} = \frac{1}{R_{can} + R_{s,soil}(X) + R_{qbr,veg}(X)} + \frac{LAI}{r_{cut}(X)} + \frac{LAI}{r_{stom,corr}(X) + r_{mes}(X)} \tag{2.5}$$

$$r_{stom,corr} = \frac{r_{stom}(PAR, LAI)}{fws} \cdot \frac{D_{\mathrm{H_2O}}}{D(X)}, \text{with } \frac{D_{\mathrm{H_2O}}}{D(X)} = \sqrt{\frac{M(X)}{M_{\mathrm{H_2O}}}} \tag{2.6}$$

The vegetation is considered as one (single-surface) big leaf (Wesely, 1989) whereas leaves are assumed to be oriented horizontally with uniformly vertically distributed leaf density. This assumption, however, neglects the detailed plant structures and characteristics (Sellers, 1985). The surface resistance at vegetation consists of in-canopy (*can*), soil (*soil*), cuticular (*cut*), stomatal (*stom*) and mesophyll (*mes*) contribution. In the original calculation, the stomatal, mesophyll and cuticular resistance are calculated at leaf level and then linearly scaled to the canopy by LAI while the different resistors are directly used at canopy level. The stomatal uptake is based on the exchange of water (Eq. 2.2). Incorporating the ratio of the molecular diffusivity (of the trace gas X) and water (H_2O) yields the gas-specific resistance. fws gives the soil moisture stress factor. The calculation of the surface resistances is based on the parametrisation for tropospheric O_3 and sulphur dioxide (SO_2) from which the dry deposition of other gases (except HNO_3, NO, NO_2) is obtained by scaling the respective resistance with the gas-specific properties of solubility ($H(X)$) and reactivity (s_{reac}) (Wesely, 1989).

$$R_{cut}(X) = \frac{R_{cut,d}(\mathrm{O_3})}{10^{-5} \cdot H(X) + s_{reac}(X)} \tag{2.7}$$

$$R_{ws}(X) = \left[\frac{1/3}{R_{cut,w}(SO_2)} + 10^{-7} \cdot H(X) + \frac{s_{reac}(X)}{R_{cut,w}(\mathrm{O_3})}\right]^{-1} \tag{2.8}$$

Often the resistances are pre-defined with constants such as the original cuticular ($R_{cut,\mathrm{O_3}}$ =10^5 s m^{-1}) and wet skin (($R_{ws,\mathrm{O_3}}$ =2000 s m^{-1}) resistance of O_3. Further details can be found in Kerkweg et al. (2006a) and Emmerichs et al. (2021).

Natural emissions

The biogenic emissions of NO_x (from the soil) and VOCs (from vegetation) are calculated online within the submodel ONEMIS depending on the actual model state. The soil NO_x emissions are based on the parametrisation by Yienger and Levy II (1995) described in Ganzeveld et al. (2002). The calculation varies mainly with soil wetness and soil temperature and depends on the prescribed fields of agriculture/cultivation and LAI. Applying this algorithm, models estimate global soil NO_x

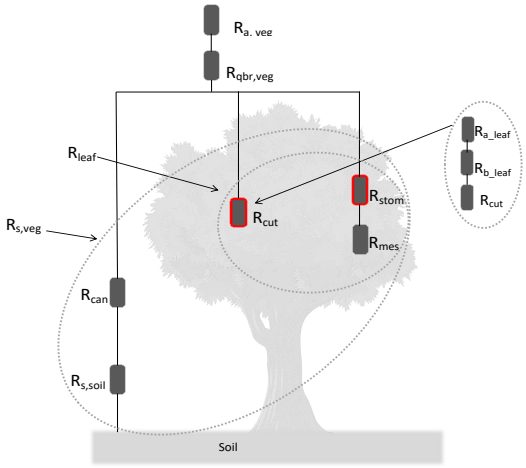

Figure 2.1: Dry deposition resistance analogy as used in Emmerichs et al. (2021); modified resistors are marked with red boxes.

emissions of 3.3-7.7 Tg a^{-1}. This is within the estimates of other models but at the lower end of satellite-based constraints (7.9-16.8 Tg per year, Weng et al., 2020).

The parametrisation of isoprene and monoterpene emissions from plants calculated in ONEMIS is based on the work by Guenther et al. (1995). This depends on the landscape average emission capacity, the model temperature, the radiative conditions within the canopy, the leafage and the prescribed foliar density. Guenther et al. (2006) developed a more comprehensive, semi-empirical modelling system for estimating the global net emission of gases (and aerosols), which is incorporated in the submodel MEGAN, an alternative to ONEMIS. This model calculates first an emission factor (ϵ) based on prescribed databases of plant function types (PFT: plant species e.g. trees, grasses), which uses satellite observations, vegetation inventories, ecosystem maps, and ecosystem model outputs. The factor ρ accounts for the production and loss within plant canopies. The emission changes due to deviations from standard conditions are calculated by the emission activity factor (γ):

$$Emission = \epsilon \cdot \gamma \cdot \rho \tag{2.9}$$

$$\gamma = \gamma_{CE} \cdot \gamma_{age} \cdot \gamma_{SM} \tag{2.10}$$

where γ_{CE} accounts for changes caused by variations in the canopy (LAI, light, temperature, humidity, wind conditions) and γ_{age} considers adjustments due to leaf age effects. Changes in soil moisture are described by γ_{SM} (Guenther et al., 2006) whose parametrisation is known to be uncertain (Huang et al., 2015). In the here used standard set-up of EMAC, it is set to 1 due to the high uncertainty (Jiang et al., 2018; Huang et al., 2015). A more mechanistic alternative is introduced in Chapter 6. In general, a high uncertainty of the MEGAN model is attributed to the estimation of the emission factors, which depends on the land cover data. The overall uncertainty is estimated to be about a factor of two to three (Guenther et al., 2012). Additionally, the modelling of regional BVOC and soil NO_x emission depends

on the resolution, i.e. the higher the resolution the better the representation. For BVOCs, the absolute impact is highest in the tropical forest, while the coastal and low emission regions reveal the largest relative change. Soil NO_x emissions are most resolution-dependent in the source regions such as North China and India (absolute) as well as at the coast (relative) (Weng et al., 2020).

An important source of NO_x in the free troposphere is lightning activity. Lightning accounts for 10-20 % of the global NO_x budget and the only natural transformation of N_2 in reactive nitrogen species. The process is described by a (semi-)empirical parametrisation within the MESSy submodel LNOX, which has been derived from correlations between other observable quantities. In general, estimates of the total amount of NO_x produced by lightning globally range from 2-8 Tg(N) a^{-1}. In this study, the current MESSy standard by Grewe et al. (2001) is used among the available schemes (see Tost et al. (2007)). This parametrisation links the updraft velocity as a measure for convective strength and associated cloud electrification with the flash frequency. The obtained flash frequency is scaled by 6.548. (Jöckel et al., 2016)). However, the lightning over land and ocean is not distinguished, although less intense cloud electrification, occurs over the ocean. In general, due to the process heterogeneity and the difficulty of measurements, the uncertainty is high, about 1.4 Tg(N) a^{-1} (Tost et al., 2007, and references therein).

Anthropogenic emissions and biomass burning

Trace gas emissions (e.g. NO, CO) from anthropogenic activities such as road traffic, ships and aircraft are prescribed and calculated within the MESSy submodel OFFEMIS. Applying the prescribed emission flux to the corresponding trace gas yields the respective change of the mixing ratio at one model time step. For halogens and terrestrial emissions of dimethyl sulfide (DMS), a lower boundary condition is calculated for the vertical diffusive flux (Kerkweg et al., 2006b). The data stems from the RCP8.5 scenario performed for the fifth assessment report (AR5) of the Intergovernmental Panel on Climate Change (IPCC) (Lamarque et al., 2010), vertically distributed following Pozzer et al. (2009). Anthropogenic NO_x emissions have an uncertainty of at least 20 % (Solazzo et al., 2021). Especially over the NH, where most of these emissions occur, this can largely contribute to the overall uncertainties because the anthropogenic sources account for roughly 65 % of the total NO_x emissions (Pozzer et al., 2012).

The representation of biomass burning events calculated in the MESSy submodel BIOBURN is based on the Global Fire Assimilation System (GFAS) inventory. The data stems originally from daily merged Fire Radiative Power (FRP) observations by the MODIS instruments on board the Terra and Aqua satellites. For the data gaps, which occur because only cloud-free scenes can be observed, additional information of earlier observations is assimilated. Via a universal conversion factor, the dry matter combustion rate is derived from this (Kaiser et al., 2012). Emission factors of 40 different gas and aerosol species have been compiled by Andreae (2019) and Akagi et al. (2011), respectively, which is based on 370 published field

measurements, ideally taken shortly after the fire eruption. The general uncertainty of the GFAS inventory is around 30 %, but increases for species like NO_x in the important fire regions Siberia, Central Africa and Indonesia where insufficient ground measurements lead to a lack of spatial information. Additionally, in the tropics, GFAS underestimates the fire radiative power because the average of daily observation in the data does not account for the high oscillation during the day. Further uncertainty is likely due to undetected small fires (Andela et al., 2013).

Performed model simulations

The multiple model simulations conducted within this thesis use different resolutions, submodels and set-ups serving different investigation purposes. First, the simulated Earth climate of the newly used vertical exchange submodel VERTEX is tuned and evaluated against the old one, E5VDIFF (Chapter 3). After that, two 30-year simulations are performed at a resolution of T42L90, where the high vertical resolution ensures the most accurate representation of climate-driving processes such as vertical diffusion. The simulations are free-running to allow the model to build up its climate. They are based on the dynamical set-up (Table 2.1), which has been prepared for MESSy investigations within the Chemistry-Climate Model Initiative (CCMI, Jöckel et al., 2016). For investigating the trace gas dry deposition atmospheric chemistry (MECCA, SCAV, Sect. 2.1) and related processes (e.g. on- and offline emissions) are included as prepared for CCMI. The additionally used submodels are listed in Table 2.2. To ensure consistency in the process representation of dry deposition, we use the same LAI data in the VERTEX, DDEP and SURFACE submodels. SURFACE calculates the surface type fractions used within the dry deposition calculation. As standard, this is the LAI look-up table derived by Ganzeveld et al. (2002). Also, ONEMIS uses the default LAI data set. The resolution dependency of dry deposition is explored by the means of three simulations covering the spatial resolution of T42, T63 and T106. In the vertical, the usage of 31 layers is sufficient to resolve the troposphere and related processes affecting dry deposition. For the assessment of the extended dry deposition scheme, including a comparison against site measurements as accurate as possible, the highest affordable spatial resolution (T106) is applied. Several simulations are performed to investigate the impact of the code developments on the representation of dry deposition and trace gas evolution.

The subsequent chapters 4-6 of this thesis aim at an accurate representation of tropospheric O_3 and the related processes at global scale. Therefore, the MOM chemistry involving more chemical species and reactions, in particular a larger set of VOCs and explicit isoprene chemistry, is used (Sect. 2.1). The biogenic emissions are calculated within the submodel MEGAN, which includes, in contrast to ONEMIS, the process representation for a large set of VOCs (Sect. 2.1). The global isoprene emission is targeted to an observational constraint of 594 Tg a^{-1} (Sindelarova et al., 2014). In addition, the submodel BIOBURN is used to enable trace gas emissions from fires which belong to the complement representation of tropospheric chemistry. The pre-

scribed field capacity input data for the soil bucket scheme is updated here with a new data set provided by Hagemann and Stacke (2015). This land surface parameter data set is based on the global distribution of major ecosystem types, which have been made available by the U.S. Geological Survey. The updated data set ensures a present-day representation of the soil wetness, and in particular a reduction of the model dryness in the Amazon. The LAI among the different submodels is represented with a 0.1° time-series based on satellite observations, covering 2005-2014. The data stems from the Moderate Resolution Imaging Spectroradiometer (MODIS), which is used commonly in climate models and has been aggregated by Klingmüller et al. (2017). Using an observation-based product overcomes uncertainties introduced by previously used look-up tables and ensures capturing the inter-annual variability of vegetation. For the global focus, the simulations are conducted at T42 but include 47 vertical layers to cover the stratosphere-troposphere exchange of O_3 and the related circulation. To ensure realistic meteorology, the model dynamics (temperature, divergence, vorticity, logarithmic pressure) of all chemical simulations are nudged through assimilation of ERAiniterim reanalysis data from the European Centre for Medium-Range Weather Forecasts (ECMWF) (Jöckel et al., 2010). In addition, the simulations are performed in the Quasi-Chemistry Transport Mode (Deckert et al., 2011, QCTM), which decouples the meteorology from the chemistry feedback. The QCTM mode ensures the usage of the same meteorology and allows investigations of the respective impact of the model developments/changes. An overview of all model simulations performed within this thesis is provided in Table 2.3.

2.2 Tropospheric ozone and its precursors

Tropospheric O_3 has multiple roles in the troposphere. Since elaborated exposure near the surface (PBL) directly harms humans' health, causing issues such as reduced lung function (Fleming et al., 2018) O_3 is a public concern. Also, vegetation is threatened by O_3 exposure which can lead to reduced carbon uptake and crop yields (Fowler et al., 2009). As a short-lived climate forcer, O_3 contributes 20 % to the total anthropogenic radiative forcing of the Earth's atmosphere since pre-industrial times (Myhre et al., 2014).

O_3 is a secondary produced pollutant, whose abundance in the troposphere is controlled by chemical reactions, deposition and stratospheric influx. The importance of the different terms vary with geographical location, emission sources and meteorological conditions driving the annual cycle of O_3. The lowest levels around 10 ppb occur over remote oceans where the only O_3 source is lightning NO_x. At continents or close-by additional sources of O_3 precursors facilitate higher O_3 production, in particular where large anthropogenic emissions exist. In continental areas, the levels increase with altitude reaching a maximum of 100 ppb at 300 hPa (Gaudel et al., 2018; Monks et al., 2015). According to this, the atmospheric lifetime of O_3 ranges from several hours in polluted urban areas with high precursor emissions to sev-

eral weeks in the free troposphere where intercontinental transport can be relevant (Monks et al., 2015).

Measurement studies estimate a present-day tropospheric O_3 burden of 340 Tg, which has increased from pre-industrial times and will rise even more in the future according to predictions (Griffiths et al., 2021). Around 500 Tg a^{-1} of tropospheric O_3 is introduced from the stratosphere (observation-based estimate). Model estimates range from 325-500 Tg a^{-1} often based on the assumption of budget closure over the year (Young et al., 2018; Griffiths et al., 2020). The most recent estimation by EMAC is in line with that (355 Tg per year, Rosanka et al., 2021b). The major part of tropospheric O_3 is produced by the chemistry involving the major precursors: VOCs NO_x. Models estimate the global annual chemical O_3 production to be about 4500-5200 Tg a^{-1} (Young et al., 2018; Griffiths et al., 2020). Employing the EMAC model, Rosanka et al. (2021b) recently estimated an annual O_3 production of 5896 Tg a^{-1} . During day, the photolysis of NO_2 (Reaction 2.11) is the most important O_3 source amplified by sunlight and temperature (Monks et al., 2015; Pusede et al., 2015). The O_3 formed in Reaction 2.12 can be directly destroyed again which regenerates NO_2 (Reaction 2.13).

$$NO_2 + h\nu \rightarrow NO + O(^3P) \tag{2.11}$$

$$O_2 + O(^3P) + M \rightarrow O_3 + M \tag{2.12}$$

$$NO + O_3 \rightarrow NO_2 + O_2 \tag{2.13}$$

Further, rapid inter-conversion of NO and NO_2 occurs by Reaction 2.14 and 2.15 involving hydroxyl (HO_2) and peroxyl (RO_2) radicals. These are also key for the HO_x and NO_x fate representing the main production terms ($+CH_3O_2$: $P(O_x)$) of the odd oxygen family (Monks et al., 2015). The reaction kinetics are known to be affected by water vapour (Buszek et al., 2011) which is described further in Sect. 5.1.

$$HO_2 + NO \rightarrow OH + NO_2 \tag{2.14}$$

$$RO_2 + NO \rightarrow RO + NO_2 \tag{2.15}$$

Due to this rapid recycling, the lifetime of NO_x is short (several hours to a few days), and the highest amounts typically occur in the PBL near the emission source (Monks et al., 2015). In industrial areas such as Southeast Asia, anthropogenic emissions are a large source. However, also biogenic soil emissions and biomass burning contribute significantly to tropospheric NO_x. The latter occurs dominantly in South America and Africa. On the contrary, in remote areas lightning activity represents the main source, whose importance rises with altitude (Vinken et al., 2014). These emission patterns change with time depending on human activities and meteorological conditions.

The regeneration of HO_2 and RO_2 allowing further NO_2 formation (Reaction 2.14) occurs via reactions of VOCs of biogenic or anthropogenic origin such as carbon monoxide (CO) which then complement the net O_3 production. CO is mainly emit-

ted by anthropogenic sources and open vegetation fires (Wiedinmyer et al., 2011).

$$\mathrm{VOC} + \mathrm{OH}(+\mathrm{O_2}) \rightarrow \mathrm{H_2O} + \mathrm{RO_2} \tag{2.16}$$

$$\mathrm{CO} + \mathrm{OH}(+\mathrm{O_2}) \rightarrow \mathrm{CO_2} + \mathrm{HO_2} \tag{2.17}$$

However, whether the VOC-OH reaction occurs predominantly depends on the local VOCs:NO_x ratio. At low NO_x conditions and sufficient high VOC levels (NO_x-limited), the O_3 production increases with rising NO_x concentrations enhancing the Reactions 2.14 and 2.15 (Seinfeld and Pandis, 2016). As the NO_x levels rise further the O_3 formation becomes suppressed (VOC-limited) due to the fast NO_x consumption in Reaction 2.18 limiting the O_3 formation (Monks et al., 2015) such as in urban areas. The produced HNO_3 has a long lifetime, but it is also removed efficiently by e.g. wet deposition, and thus represents a relevant NO_x sink ($L(O_x)$). VOC-limited chemistry is also found in vegetated areas where high amounts of BVOCs such as isoprene are emitted during day increasing with temperature (up to 40 °C).

$$L(\mathrm{NO_x})\text{: } \mathrm{OH} + \mathrm{NO_2} + M \rightarrow \mathrm{HNO_3} + M \tag{2.18}$$

The major loss of tropospheric O_3 during day occurs via its own photolysis (Reaction 2.19) where effective destruction can only take place in the presence of water via Reaction 2.20. This accounts for 43 % of the daytime OH source (Seinfeld and Pandis, 2016).

$$\mathrm{O_3} + \mathrm{h}\nu \rightarrow \mathrm{O}(^1\mathrm{D}) + \mathrm{O_2} \tag{2.19}$$

$$\mathrm{O}(^1\mathrm{D}) + \mathrm{H_2O} \rightarrow \mathrm{OH} + \mathrm{OH} \tag{2.20}$$

Furthermore, O_3 is lost by the reaction with HO_x radicals which is a major sink for HO_x. Reaction 2.20, 2.21 and 2.22 are the three main contributor to the chemical loss of O_x (Monks, 2005; Griffiths et al., 2020):

$$\mathrm{O_3} + \mathrm{OH} \rightarrow \mathrm{HO_2} + \mathrm{O_2} \tag{2.21}$$

$$\mathrm{O_3} + \mathrm{HO_2} \rightarrow \mathrm{OH} + 2\,\mathrm{O_2} \tag{2.22}$$

In VOC-rich environment, the VOC ozonolysis is an additional relevant O_3 sink. Exemplary, the reaction with C_5H_8 forming different VOCs like methacrolein (MACR), methyl vinyl ketone (MVK) and formaldehyde (HCHO) as major products:

$$\mathrm{C_5H_8} + \mathrm{O_3} \rightarrow \mathrm{MACR} + \mathrm{MVK} + \mathrm{HCHO} \tag{2.23}$$

In total, the chemical destruction of tropospheric O_3 is estimated to 4000-4800 Tg a^{-1} (model estimates). Additionally, 850-1150 Tg a^{-1} are lost by dry deposition (Young et al., 2018). The most recent EMAC estimates are 5255 Tg a^{-1} and 846 Tg a^{-1} chemical O_3 destruction and dry deposition, respectively (Rosanka et al., 2021b).

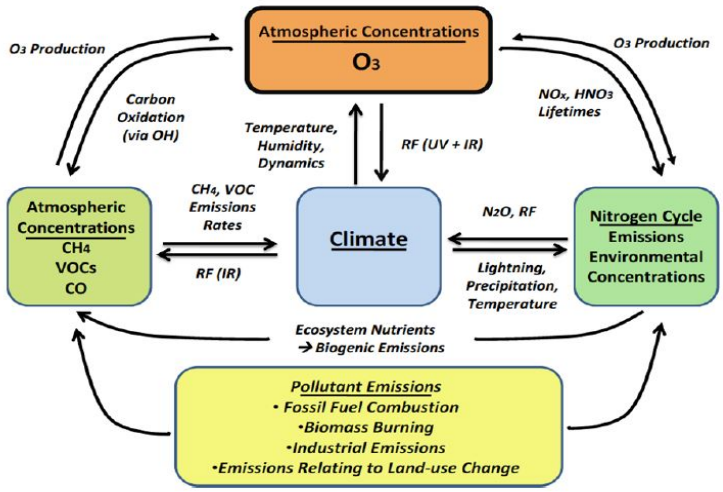

Figure 2.2: Ozone interactions (Monks et al., 2015)

The multiple bi-directional interactions of O_3 in the troposphere, modulated by meteorological parameters, are summarised by Fig. 2.2.

As the O_3 production, driven by photo-chemistry, increases with temperature and sunlight (Pusede et al., 2015) O_3 extremes are typically observed in summer amplified by stagnant conditions where the precursors accumulate in the PBL (Andersson and Engardt, 2010, e.g.).

A measure for the O_3 formation during the oxidation cycles is the Ozone Production Efficiency (OPE). It reveals the number of O_3 molecules formed per removal of NO_x from the oxidation cycle. According to Wang et al. (2018), this includes the major O_x production terms ($P(O_x)$, Reaction 2.14, 2.15 and of CH_3O_2) and the main NO_x loss term (Reaction 2.18), defined above. It also involves the HNO_3 production by VOCs reacting with nitrates (NO_3) (Reaction 2.25) and the heterogeneous loss of dinitrogen pentaoxide (N_2O_5) at aerosol or cloud water (Reaction 2.26). The latter reaction has been found to account even for 30 % of the HNO_3 production in the atmosphere (Liao and Seinfeld, 2005) :

$$OPE = \frac{P(\mathrm{O_x})}{L(\mathrm{NO_x}) + P(\mathrm{HNO_3}) + P_{het}(\mathrm{N_2O_5})} \tag{2.24}$$

$$P(\mathrm{HNO_3}) = \sum_{VOC} (\mathrm{VOC} + \mathrm{NO_3} \rightarrow \mathrm{VOC2} + \mathrm{CO} + \mathrm{HNO_3}) \tag{2.25}$$

$$L_{het}(\mathrm{N_2O_5}) = \mathrm{N_2O_5} + \mathrm{H_2O(het)} \rightarrow 2\mathrm{HNO_3} \tag{2.26}$$

Studies comparing multiple models (e.g. CMIP6[2]) report a general overestimation of tropospheric O_3 in the NH (20 %) and an underestimation in the Southern Hemisphere (SH) (Griffiths et al., 2021; Young et al., 2018, 2013). This has been shown for EMAC as well (Jöckel et al., 2016). The models reproduce the spatial and seasonal

[2]Coupled Model Intercomparison Phase 6 (`https://esgf-node.llnl.gov/projects/cmip6/`, last access at 22 November 2021)

variability and capture previous trends well (Griffiths et al., 2021). But Griffiths et al. (2021) identifies the different troposphere definition as a key uncertainty. A further uncertainty source might be the VOC emissions which are spatially correlated with the model spread (Griffiths et al., 2021; Young et al., 2013). Among the different O_3 budget terms, dry deposition shows the comparably largest model spread indicating a high uncertainty which possibly arises from different parametrisations, a lack of observational constraints and different land representation (Young et al., 2018). Recently, Rosanka et al. (2021b) suggests that the simplification of the aqueous-phase O_3 chemistry may account for 20 % of the overall uncertainty.

Volatile organic compounds

Organic compounds are a key for atmospheric photochemistry since they drive the oxidative processes. Those compounds with 15 or fewer carbon atoms and high volatility in the atmosphere (vapour pressure> 10 Pa at 25°C, boiling point of up to 260°C at atmospheric pressure) belong to the large group of VOCs (tens of thousand) which exist at mixing ratios of 10^{-9} (ppb) down to 10^{-12} (ppt). In total (non-methane hydrocarbons), 186 TgC a^{-1} is emitted from various anthropogenic activities such as exploitation of fossil fuels, road transport and biomass burning, among others. Biogenic emissions, however, are estimated to be ten times larger, ranging from 370 to 1150 TgC a^{-1}. Thereby, VOCs are mainly released through the assimilation of carbon dioxide during plant photosynthesis. The ocean and soils are small contributors (Koppmann, 2008, and references therein). The main VOCs emitted by plants are isoprene and monoterpenes. The amount and the species emitted vary among the plant type, age, health and ambient meteorological conditions (Guenther et al., 1995). All compounds are mainly removed by oxidation with OH (see Reaction 2.16) and to a lesser extent by reactions with O_3, NO_3 and halogen radicals. Also, during sunlight, some compounds photolyse, which yield smaller fragments. Further important sinks are dry deposition to surfaces such as vegetation and wet deposition.

Due to their high reactivity, oxygenated VOCs (OVOCs) play a specially important role in the O_3 formation. Large amounts of OVOCs stem from the oxidation of hydrocarbons such as CH_4 among being emitted from various anthropogenic and biological sources. Their photolysis, being the main sink for some OVOCs, forms significant amounts of radicals and drives the atmospheric HO_x production. As an example, the reaction is shown here for HCHO (Koppmann, 2008, and references therein).

$$\mathrm{HCHO} + h\nu \rightarrow H + HCO \tag{2.27}$$

$$\rightarrow \mathrm{HO_2} + CO \tag{2.28}$$

2.3 Observation data

Within this study, three different kinds of observational data sets are used, serving different purposes. For assessing the influence of the revised dry deposition scheme (Chapter 3), we use O_3 flux measurements at four sides: Hyytiälä (Finland), Borden research station (Canada), Lindcove research station (USA) and the Amazon Tall Tower (South America). Gas fluxes are derived mostly from fluctuations of the vertical wind velocity and the gas concentration (eddy-covariance technique). For the wind measurements, for example (ultra-)sonic anemometers are used (Rannik et al., 2012; Fares et al., 2012). O_3 measurements are based on chemiluminescence where a solid or organic liquid dye emits light until it reacts with O_3. On the other hand, the O_3 concentration can be obtained by measuring the absorption (see description below) (Fares et al., 2012; Clifton et al., 2020). A high instrument resolution is required to resolve the small scale eddies accurately. Small eddies are associated with vertical transport and the small gas concentration variations in the range of 10-60 Hz. The measuring systems can differ individually since no standard exists, thus the applied corrections cover a wide range (Clifton et al., 2020). In separate cases, O_3 dry deposition is estimated by the eddy diffusivity and the concentration gradient within the canopy based on the K-theory (Wu et al., 2016). The O_3 diffusivity is often assumed to be identical to the diffusivity of sensible heat, which, however, does not hold when the gradient is perturbed by the local chemistry. For sensible heat, it is calculated based on the Monin-Obukhov similarity theory. It limits the possible observation height to the roughness sublayer where, however, most observations are located (Clifton et al., 2020). Both methods have a general uncertainty of 10-20 % (Rannik et al., 2016; Wu et al., 2016).

Second, to evaluate the impact of introduced meteorological dependencies (Chapter 4-6) on O_3 levels, ground-based O_3 measurements from the TOAR (Tropospheric Ozone Assessment report) database are used in monthly resolution. The TOAR database (Schultz et al., 2017) includes measurements at almost 10,000 sides around the world, which have been sampled from multiple monitoring networks (e.g. Clean Air Status and Trends Network (CASTNET)) and data providers (e.g. Umweltbundesamt) (Schultz et al., 2017). The various applied measurement techniques use the chemical and radiative properties (UV absorption, IR absorption and emission) of tropospheric O_3. Since 1970, UV absorption photometers are the common standard for in-situ O_3 measurements. The instruments, which measure the UV light absorption at the wavelength, where O_3 absorbs the strongest (Hartley band: 220-310 nm), have a sensitivity of 1 ppb. The instruments need little maintenance and show the required signal-to-noise ratio, detection limit, stability of sensitivity and negligible interference during clean-air measurements. The measurement uncertainty is below 2 ppb (Tarasick et al., 2019, and references therein). The collected data has run through extensive data control. Thereby, for example, time-series with frequent interruption or significant change of the measurement technique are excluded from the data (Schultz et al., 2017). For this study, the data is filtered for low-elevation and rural sites, since the model resolution of 250 km only captures those. The remaining data in the SH is sparse, therefore only the NH is considered in the comparison.

The lower tropospheric O_3 (up to 300 hPa) simulated by EMAC is compared with a satellite product based on the observations by the Infrared Atmospheric Sounding Interferometer (IASI) instrument. This thermal infrared (TIR) Fourier transform spectrometer onboard the MetOP-A and B satellites measures the backwards radiation of the Earth's surface and the lower atmosphere while the satellites surround the Earth on a polar, sun-synchronous orbit crossing the Equator at around 9:30 a.m. and p.m. local time. IASI has a higher sensitivity than UV-visible instruments (Clerbaux et al., 2009). The applied nadir view is most efficient to observe the global O_3 distribution in the atmosphere since it allows covering the globe twice a day with more than ≈ 1.3 million spectra per day (Boynard et al., 2016, and references therein). With the fast radiative transfer and retrieval software FORLI (Fast Optimal Retrievals on Layers for IASI) version 20151001 near-real-time global O_3 concentrations are retrieved from IASI. The application-specific flags exclude poor spectral fits, data with poor vertical sensitivity and cloudy scenes. This procedure ensures overall good data quality. Also, restricting the data to 300 hPa limits the influence of stratospheric O_3 while the tropospheric layers of maximum IASI sensitivity are still covered (Wespes et al., 2017). Multiple studies (Hurtmans et al., 2012; Boynard et al., 2018) have estimated the statistical bias of the measurement to about 5-20 %. A comparison with ozone sondes shows an underestimation of the FORLI O_3 in the mid-latitudes and the tropics (11-13 % and 16-19 %, respectively). For the comparison with EMAC, vertical O_3 profiles (in volume mixing ratio, VMR) are sampled at the time and location of the IASI instrument by the MESSy submodel SORBIT (Jöckel et al., 2010). Then, after the interpolation to FORLI-O_3 pressure grids, the data are converted to column profiles. This procedure is repeated for each of the several IASI measurements falling into one model (here: 2.8° x 2.8°) grid box for one day. The application of the FORLI-O_3 averaging kernels to the simulated O_3 data according to Rodgers (2000) then additionally accounts for the vertical sensitivity of IASI in the resulting simulation data, as would be seen by IASI.

Table 2.3: Overview of the EMAC simulations

Simulation[a]	Resolution	Set-up
published (Chapter 3):		
E5VDIFF climatological simulation (clim-E5)	T42L90MA	Dynamical submodels including E5VDIFF
VERTEX climatological simulation (clim-VER)	T42L90MA	Dynamical submodels including VERTEX, modified cloud parameter
Dry deposition evaluation - default (DEF)	T106L31ECMWF	Standard CCMI set-up (including CCMI chemistry)
Dry deposition evaluation - soil moisture stress (REV-fws)	T106L31ECMWF	CCMI set-up (including CCMI chemistry), modified soil moisture stress parametrisation
Dry deposition evaluation - temperature and VPD stress (REV-fTfD)	T106L31ECMWF	CCMI set-up (including CCMI chemistry), new temperature and drought stress factors
Dry deposition evaluation - revised (REV)	T106L31ECMWF	CCMI set-up (including CCMI chemistry), cuticular parametrisation, modified stomatal stress factors
Dry deposition evaluation - non-nudged (REV-NNTR)	T106L31ECMWF	as REV, free-running
Resolution dependency (REST42)	T42L31ECMWF	CCMI set-up (including CCMI chemistry).
Resolution dependency (REST63)	T63L31ECMWF	CCMI set-up (including CCMI chemistry).
Chapter 4-6:		
Reference simulation (EMACref)	T42L47MA	MOM chemistry, biomass burning and biogenic emissions of VOCs (MEGAN)
Impact of the revised dry deposition scheme (EMACddep)	T42L47MA	Reference set-up, dry deposition scheme by Emmerichs et al. (2021)
Impact of the water-dependent radical chemistry (EMACh2o)	T42L47MA	Reference set-up, water-dependent radical chemistry
Impact of the drought-dependent isoprene emissions (EMACisop)	T42L47MA	Reference set-up, BVOC drought stress factor

[a]Simulation label in brackets

3 A revised dry deposition scheme for land-atmosphere exchange of trace gases in ECHAM/MESSy v2.54

A detailed version (Appendix) of this section was published as:

Emmerichs, T., Kerkweg, A., Ouwersloot, H., Fares, S., Mammarella, I., and Taraborrelli, D.: A revised dry deposition scheme for land–atmosphere exchange of trace gases in ECHAM/MESSy v2.54, Geosci. Model Dev., 14, 495–519, https://doi.org/10.5194/gmd-14-495-2021, 2021.

The authors' contribution is listed here:

- T. Emmerichs: code development together with A. Kerkweg, model simulations, data analysis, manuscript writing, proof-reading
- A. Kerkweg: code development
- H. Ouwersloot: original writing of the MESSy VERTEX vertical diffusion submodel
- S. Fares: realisation of the measurement data from Lindcove and further related theoretical calculations for the analysis
- I. Mammarella: realisation of dry deposition measurements at Hyytiälä and related support during the analysis
- D. Taraborrelli: concept, supervision and discussions

3.1 Introduction

A realistic model representation of dry deposition is critical to simulate the trace gases levels in the troposphere as good as possible, especially for tropospheric ozone. Advancements in this field ultimately affect model predictions of air pollution, which

[1] `https://creativecommons.org/licenses/by/4.0/` (last access: 1 February 2022)

is of high public concern (Young et al., 2018). Tropospheric O_3 is not only controlled by chemical production and loss. About 20 % of the total tropospheric O_3 loss is attributed to dry deposition. While the stomatal contribution to O_3 dry deposition ranges from 30-90 % (45 % on average) depending on meteorological and environmental conditions and the species properties also the non-stomatal pathway is desirable (Hardacre et al., 2015; Clifton et al., 2020, and references therein). However, global chemistry-climate models differ largely in estimating the O_3 dry deposition term, which represents a major uncertainty in the estimates of the global O_3 budget (Young et al., 2018). Studies attribute the main fraction of this uncertainty to the different process representation across models (Hardacre et al., 2015, and references therein). In particular, the representation of non-stomatal uptake suffers from knowledge gaps and crude parametrisations. A relevant uncertainty source is associated with the local meteorology, which strongly modulates the variation of dry deposition (Wong et al., 2019). As future projections yield an increase in weather extremes due to climate warming (Ridder et al., 2022) the investigation of these effects becomes highly desirable.

This study presents an extension of the current dry deposition scheme in EMAC with crucial features and meteorological dependencies applied to all trace gases deposited in the model. Thereby, the parametrisations are selected to serve the model focus, which is on complex atmospheric chemistry rather than on a sophisticated land surface representation. Tropospheric O_3 is central here since it is the basis of the dry deposition scheme, and additionally, most dry deposition measurements are available. The analysis of the model simulations characterises the effects of each added model feature and assesses the global impact on O_3. The modelled dry deposition velocity is compared with measurements at four ground stations, which represent different land cover types and climates. This analysis allows us to evaluate the scheme and identify weaknesses and additional knowledge gaps. Also, the dependence of dry deposition on the model resolution is explored here, which points to potential uncertainties in the process representation. The vertical exchange model of EMAC (VERTEX), which contains the modified parametrisation of the stomatal resistance, is documented first in this study. Then, it is evaluated against results obtained with the legacy submodel E5VDIFF.

3.2 Methodology

In this study, different methods are employed in terms of the preparation of simulations, the development of the dry deposition scheme and the assessment of their global and local impact when compared to site measurements. The first part aims at the evaluation of the vertical diffusion and exchange submodel VERTEX (see Sect. 2.1) against the former MESSy standard E5VDIFF to give a general recommendation for future use of VERTEX. However, first, the simulated climate has to be best matched to the current state of the Earth's climate, in this case, the state simulated by E5VDIFF. For this purpose, the model radiation balance at the top of

the atmosphere (TOA) should agree. Thus, the model is re-tuned during multiple simulations modifying four cloud parameters: the convective mass-flux above the level of non-buoyancy, entrainment rate for shallow convection, entrainment rate for deep convection and convective cloud conversion from cloud water to rain (Mauritsen et al., 2012). Including this new set of parameters, the long-term VERTEX simulation (clim-VER, Table 2.3) can be performed while representing (almost) the same climate state as E5VDIFF.

To improve the representation of trace gas uptake at vegetation, the parametrisation of the surface resistance in EMAC is modified. The stomatal resistance which originally only relies on solar dependence (Eq. 2.2) is extended with further meteorological sensitivities to temperature and atmospheric water demand (vapour pressure deficit: VPD[2]) following the commonly used multiplicative approach by Jarvis (1976):

$$f(T) = b_3(T - T_l)(T_h - T)^{b_4} \tag{3.1}$$

$$f(VPD) = VPD^{-\frac{1}{2}} \tag{3.2}$$

The stomatal temperature stress parametrised with an empirical formulation by Jarvis (1976) varies between a lower and upper-temperature threshold around an optimal value of 25 °C. We note that the parameters $T_h = 318.15$ K, $T_l = 268.15$ K, $b_3 = 8\ 10^{-3}$ and $b_4 = 0.5$, however, have been derived from one side only (Jarvis, 1976) and introduce some uncertainty. The VPD stress factor is based on the theory of minimising water loss at maximum CO_2 uptake during plant photosynthesis (Katul et al., 2009). Also, the parametrisation of plant water stress to stomata based on soil moisture is critically re-assessed. As it leads to an unrealistic shutdown of the stomatal deposition, e.g. during the dry season in the Amazon basin, the lower threshold (wilting point) is removed according to the original parametrisation by Delworth and Manabe (1988). Furthermore, since the cuticle contributes significantly to dry deposition to vegetation (Hogg et al., 2007; Clifton et al., 2020; Rannik et al., 2012) an explicit parametrisation of the cuticular uptake empirically derived by Zhang et al. (2002) is implemented in DDEP (Sect. 2.1).

$$R_{cut,d}(\mathrm{O_3/SO_2}) = \frac{R_{cut,d0}(\mathrm{O_3/SO_2})}{\exp(0.03 \cdot RH) \cdot LAI^{0.25} \cdot u_*} \tag{3.3}$$

$$R_{cut,w}(\mathrm{O_3/SO_2}) = \frac{R_{cut,w0}(\mathrm{O_3/SO_2})}{LAI^{0.5} \cdot u_*} \tag{3.4}$$

where the cuticular resistance of O_3 and SO_2 is distinguished for dry canopies ($R_{cut,d}$) and wet canopies ($R_{cut,w}$), respectively, depending on relative humidity (RH in [%]), LAI and friction velocity (u_* in [m s^{-1}]). The input parameters are $R_{cut,d0}(O_3)$=5000 s $^{-1}$, $R_{cut,w0}(O_3)$=300 s $^{-1}$ and $R_{cut,d0}(SO_2)$=2000 s $^{-1}$ (Zhang et al., 2002). For rain and dew conditions, values of 50 s m^{-1} and 100 s m^{-1} are prescribed for $R_{cut,w0}(SO_2)$. The default scheme only uses the originally proposed

[2] $VPD = p_{H_2O,sat}(T) - p_{H_2O} = \left(1 - \frac{RH}{100}\right) p_{H_2O,sat}(T)$,
RH: relative humidity, $p_{H_2O,sat}(T)$, p_{H_2O}: saturated and actual water vapour pressure in [kPa]

high constants by Wesely (1989) which leads to a minor contribution of cuticular uptake in the model. The user can apply these code modifications via switches in the respective submodel namelist of VERTEX and DDEP. Thereby, the consistency among the dry deposition calculation in VERTEX and DDEP has to be ensured, i.e. the resistances are either calculated at leaf or canopy level.

3.3 Summary of the results

The study reports firstly on the usage of the vertical exchange and diffusion submodel VERTEX, which represents a replacement for E5VDIFF since it contains important bug fixes and optimised code. To construct a similar climate with VERTEX like with E5VDIFF, the model radiation balance with VERTEX is tuned before the long-term simulation is conducted. After many sensitivity simulations were performed, the application of a slightly higher conversion rate to rain in the VERTEX simulation yields a final radiation imbalance at TOA of -1.55 W m^{-2}. The difference to the TOA estimate with E5VDIFF is within the uncertainty range of $\pm$ 0.4 W m^{-2}. The submodels dynamics are evaluated against each other on a climatological timescale (1979-2008). The global (weighted) annual mean values of EMAC using E5VDIFF and VERTEX show different comparisons. The time-series of cloud liquid water and planetary boundary height reveal small deviations within the respective uncertainty range of the values. The surface temperature and relative humidity predicted by E5VDIFF and VERTEX differ to a higher extent during some periods whereas, however, the long-term annual means are not significantly different. However, the dynamical tuning of VERTEX has to be repeated as a bug (in the radiation scheme), which was found in the meantime, has to be considered.

Regarding the investigation of dry deposition, the revised scheme is evaluated against dry deposition velocity measurements at four sites representing the main landcover types at different time scales. The comparison of measured and modelled monthly means at a mixed forest with a temperate climate in Southeast Canada (Borden forest) reveals an improved agreement of the modified scheme with the measurements. Portioning the dry deposition in stomatal and non-stomatal uptake shows this is mostly due to the increased cuticular uptake. However, a discrepancy remains in late (boreal) summer. This mismatch is attributed to the underestimated relative humidity (compared to the micro-meteorological measurement) and thus too low cuticular uptake in the model. In the cold-temperate boreal forest in Hyytiälä, however, the comparison reveals a general mismatch of the modelled and measured annual cycle. Both dry deposition schemes simulate too high values in summer. The overestimation in the old parametrisation arises from the constant LAI of 1 in the stomatal resistance. Including the cuticular pathway enables a significant contribution to dry deposition, which agrees with previously reported findings during autumn. But the stomatal uptake is still overestimated. This overestimation arises from a too high summer LAI in the model and the negation of the wilting point in the soil moisture stress function.

The measured daily cycle of dry deposition velocity at the irrigated Orchard in California (Mediterranean, Lindcove research station) is represented well by the revised model parametrisation in spring 2010. The inclusion of the cuticular uptake improves the representation at night. During the day, the stomatal temperature and VPD stress factors additionally reduce the overestimation, which confirms the findings by Fares et al. (2012). However, applying a stomatal soil moisture stress function does not reproduce the realistic conditions of the irrigated site in spring and summer, which significantly affects the dry deposition modelling. The stomata in the model suffer from too high temperature stress, which leads to an under-predicted dry deposition. This high temperature occurs because the model does not capture the sustained cooling by evapotranspiration, resulting in a higher model temperature (compared to the measured values). Also, the soil moisture is not captured correctly in the model due to the irrigation. Furthermore, the accurate representation of soil deposition may be a potential contributor to an improved modelling (Fares et al., 2012).

At the densely vegetated tropical rainforest, O_3 dry deposition is under-predicted by EMAC. However, similar low values are reported by other models as well (Hardacre et al., 2015). The underestimation in EMAC compared with measurements at the Amazonian Tall Tower Observatory (ATTO) is attributed to the dry bias in the Amazon forest, which arises from the missing soil moisture storage in the bucket scheme of EMAC (Hagemann and Stacke, 2015). Consequently, the simulated relative humidity is too low, as shown in comparison with ERA5 data. The model dryness also limits the cuticular uptake, which is especially important at night. In the dry season, the mismatch of relative humidity is even higher. By that, the soil moisture stress formulation of the standard model leads to a shut-down of the dry deposition, while the modified formulation allows for some uptake. Also, too high-temperature stress acts on the stomata. Omitting meteorological nudging, which can have a detrimental effect on precipitation and evaporation (Jeuken et al., 1996), leads to an increase of humidity (air and surface wetness). This yields more realistic stomatal stress factors compared to the factors calculated from observation data. Also, the cuticular uptake is increased, which brings the simulated dry deposition velocity closer to the measurements.

Globally, the revised dry deposition scheme allows higher dry deposition velocity of up to 0.5 cm s^{-1} in (boreal) summer. The increase is mainly due to the explicit representation of cuticular uptake, which has the largest effect in the northern continental regions covered by dense vegetation. The much lower soil moisture stress in regions with dry soil ($<$ the lower threshold/wilting point) also boosts the stomatal deposition. The addition of the temperature and VPD stress factor has a spatially varying impact. While in humid and cold temperate climates the stomatal deposition rises, a decrease occurs in drought/temperature stressed regions. The annual global dry deposition of the sensitivity study increased by 6 % due to the modifications. The resulting estimate is in line with other models (Young et al., 2018). The subsequent reduction of ground-level O_3 by up to 12 ppb (24 %) in some regions might potentially contribute to the reduction of the positive O_3 bias when compared

to measurements. In fact, for EMAC, e.g. Righi et al. (2015) reports an overestimation of 20 ppb. Also, other trace gases are affected by the revised dry deposition scheme, depending on the gas-specific properties.

The spatial model resolution impacts the simulation of meteorology, surface processes and dilution of O_3 and its precursors, which drive dry deposition. The analysis of the global annual dry deposition flux modelled at three different resolutions shows a difference of up to 40 Tg yr^{-1}. The T106 resolution simulates the highest flux. In the NH, the difference is driven by ground-level O_3, which also dominates the global correlation. Only in the SH extra-Tropics, a significant correlation to temperature is found. The discrepancies are attributed to a different representation of atmospheric humidity.

The revised dry deposition scheme published here represents a relevant contribution to the study by Franco et al. (2021) aiming at an improved simulation of formic acid (HCOOH). The study contribution includes the re-formulation of the stomatal soil moisture stress, which assumes more realistic stress values and buffers the dry model bias in the Amazon basin. The inclusion of the additional meteorological dependencies on temperature and atmospheric water demand increases the sensitivity of dry deposition to extreme events. Furthermore, implementing an explicit non-stomatal deposition at dry and wet cuticles accounts for a non-negligible additional loss of HCHO. This loss term counter-balances the HCOOH increase by the chemical source implemented here, leading to a better agreement of the model values with observations.

4 Impact of the revised dry deposition scheme

This chapter investigates the impact of the revised dry deposition scheme (i.e., meteorological stress factors, cuticular resistance parametrisation) described in Emmerichs et al. (2021) on the tropospheric composition and assesses its potential to reduce the tropospheric model bias. For this purpose, we conduct an additional sensitivity simulation (EMACddep) which considers, in contrast to Emmerichs et al. (2021), the complex chemical mechanism MOM (Sect. 2.1) and the representation of oxygenated VOCs.

4.1 Changed dry deposition of ozone and OVOCs

For the sake of this comprehensive analysis, the impact of the modified scheme O_x dry deposition is here firstly summarised. As shown in Emmerichs et al. (2021), applying the extended dry deposition scheme, in general, enables an additional cuticular (non-stomatal) uptake of trace gases that are relatively soluble or reactive. The importance of this pathway is proportional to LAI and humidity (Altimir et al., 2006; Zhang et al., 2002). The stomatal stress factors associated with temperature and vapour pressure deficit (VPD) have a spatially differing impact. For instance, the VPD stress factor counteracts the temperature stress under very humid conditions. The importance of this mechanism depends on the competition between the stomatal and non-stomatal pathways for the compound's dry deposition, which varies with molar mass, the water solubility and the reactivity of trace gases (see Eq. 2.6-2.8).

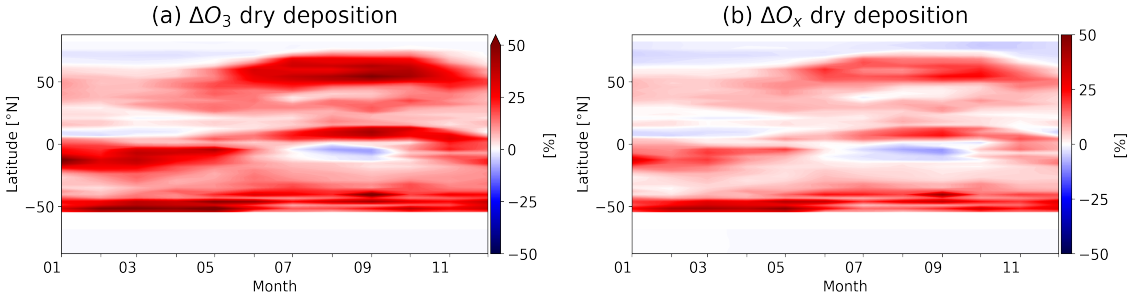

Figure 4.1: Zonal mean relative difference of the dry deposition flux over land (a) of O_3 and (b) O_x in 2009.

The annual cycle of the zonal mean change reveals that the extended scheme increases the O_3 dry deposition flux by up to 50 % mainly due to the enhanced cuticular uptake (Fig. 4.1a). The uptake increases towards boreal summer (JJA: June-August) in the NH by more than 20 %. The changing pattern follows mainly the seasonal variation of the vegetation foliage on the NH (extra-tropics), which is the main driver of stomatal and cuticular uptake. The only decrease in dry deposition flux occurs during August/September in the tropics, where the overestimation of the stomatal deposition by the standard scheme is highest among the globe due to the high vegetation density (see Emmerichs et al. (2021)). The (global, annual) maximum dry deposition velocity of O_3 is increased by 36 %. Globally, the O_3 dry deposition flux estimated by EMACref to 780.2 Tg a^{-1} is increased slightly by 3.5 % (Tabl 4.1). A comprehensive view of the impact on tropospheric O_3 and the related chemistry is revealed by the dry deposition of total O_x (for dry deposition: NO_2, NO_3, N_2O_5, HNO_3, HNO_4, HOBr, $BrNO_3$). Globally, the dry deposition of all O_x compounds is estimated to be 825.2 Tg a^{-1} (EMACref). Table 4.1 lists the O_x compounds dry deposition properties and the changes due to the extended scheme. Although relative to O_3 the dry deposition fluxes are much lower, the relative change of the vegetation uptake for the other O_x species is significant. All compounds are considered as reactive as O_3 (f=1, Eq. 2.7, 2.8) while they are more soluble ($H(X)$ >0.01) and less diffusive in air ($\frac{D_{H_2O}}{(D(X)}$ >1.6). The diffusivity in the air determines the transport of trace gases through the boundary layer and the uptake at stomata. The lower the molecular weight (larger diffusivity), the more the trace gas is favoured for dry deposition at the surface. An empirical relationship of observed daytime deposition scale of highly depositing compounds and the inverse of the molecular mass has been found by Nguyen et al. (2015, their Fig. 5). Accordingly, the highest uptake velocities during the year are predicted for $BrNO_3$, HNO_3, HNO_4 and N_2O_5 because they are very reactive in the aqueous phase. Among those, the actual global dry deposition flux per year is highest for HNO_3 due to its high dry deposition velocity and its abundance. In the standard scheme, it is treated as most favourable for dry deposition with low resistance ($R(HNO_3)$=1 s m^{-1}) at all surfaces since it is observed to be removed within one day (Wesely and Hicks, 2000). Therefore, the maximum dry deposition velocity is not significantly increased by the modified dry deposition applied here. The largest change is seen for NO_2, which is commonly considered to be deposited similarly as O_3 (Wesely and Hicks, 2000), with a doubling of the maximum uptake velocity throughout the year. Globally, the revised scheme yields a 27 % higher NO_2 loss by dry deposition. The dry deposition of HNO_4 is also increased notably. This increase contributes to the change of O_x dry deposition (flux) in some regions like the northern hemispheric boreal forest and Central Africa. The annual dry deposition flux of N_2O_5, a relevant night-time oxidant, is reduced, which likely arises from the increased dry deposition of its precursors, NO_2 and NO_3. The N_2O_5 dry deposition velocity remains unchanged. This result demonstrates that the modifications of dry deposition also have implications for the night-time chemistry. The annual cycle of zonal mean O_x dry deposition shows a similar pattern as seen for O_3 but with lower increase over the course of the year (Fig. 4.1b). Despite the various effects described above, the revision of the

deposition scheme yields a similar increase of the annual global dry deposition flux as for O_3.

Table 4.1: Global annual dry deposition of O_x compounds, their diffusivity in air ($\frac{D_{H_2O}}{(D(X)}$), the effective solubility (H(X) in [M atm^{-1}]), the estimated maximum dry deposition velocity ($v_{d,max}$ in [cm s^{-1}]), the global annual dry deposition flux (in [Tg a^{-1}]) and the respective change of the estimates by EMACddep.

Compound	$\frac{D_{H_2O}}{(D(X)}$	H(X)	$v_{d,max}$	$\Delta v_{d,max}$	Flux	ΔFlux (%Δ)	Normalised Δflux[a]
O_3	1.6	0.01	0.7	+36 %	780.2	+26.6 (3.4)	+6.1 %
NO_2	1.6	0.01	0.5	+52 %	7.3	+2.2 (30)	+29 %
NO_3	1.9	1.8	0.63	+36 %	0.04	0 (+3.4)	+1.4 %
N_2O_5	2.4	$1.\times10^{40}$	3.4	0	1.0	-0.11 (11)	-1.0 %
HNO_3	1.9	$1.\times10^{40}$	3.5	+3.1 %	36.2	-0.4 (1.0)	-78 %
HNO_4	2.1	1.3×10^{6}	2.3	+13 %	0.4	+0.03 (7.7)	+2.4 %
$BrNO_3$	2.8	$1.\times10^{30}$	4.58	0	0	0	-0.1 %
HOBr	2.3	91	0.54	+43 %	0.05	0 (+3.4)	+1.2 %
$\sum(O_x)$					825.4	+28.4 (3.4)	

[a] ΔEMACddep normalised by surface gas mixing ratio [mol mol^{-1}]

In the following, the different responses of dry deposition to the changes are explored separately during day and night, as the cuticular uptake has been observed to be favoured during night (Rannik et al., 2012). Thereby, we define the daytime period according to O_3 photolysis. Only boreal summer is considered, as dry deposition is most important (i.e., highest) during that time of the year. When day- and night-time dry deposition are distinguished, substantial different changes become apparent. During summer day-time, the O_3 uptake is reduced under very dry conditions where the stomatal temperature stress dominates, such as in the Southern U.S. (Fig. 4.2a). The decrease in the tropical evergreen forests (the highest LAI globally) arises from the overestimation of the default stomatal dry deposition and the local dryness in the model (Emmerichs et al., 2021). An increase occurs in sufficiently moderate to humid climates and over vegetated areas during the day, whereas the night-time changes are significantly higher (Fig. 4.2b). The stomatal uptake is small during the night due to its light dependence and thus contributes only slightly to the night-time dry deposition. Overall, the night-time dry deposition increases by 6.9 % due to the modified parametrisation, whereas the increase during the day is only minor (1.5 %) throughout the year. This highlights the important contribution of the cuticular parametrisation enabling vegetation uptake during the night.

Studies by e.g. Nguyen et al. (2015) and Karl et al. (2010) show that also significant amounts of OVOCs are removed efficiently by dry deposition during the day, which is attributed mainly to the non-stomatal pathway. In particular, compounds with high solubility, and thus high potential to interact with water layers at the surface, are favoured to undergo non-stomatal uptake. Also, sufficient reactivity enables some

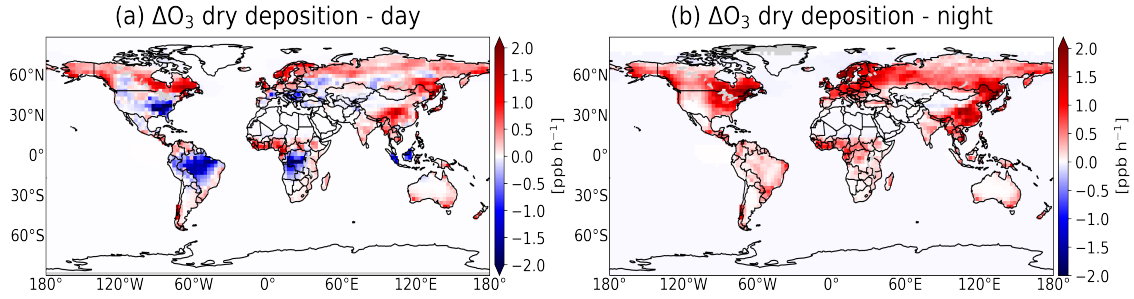

Figure 4.2: Absolute difference of O_3 dry deposition flux during (a) day and (b) night in JJA.

interaction of the trace gas with the surface as it is considered in the Wesely (1989) dry deposition scheme (see Eq. 2.7, 2.8). Table 4.2 lists the here considered OVOCs, their dry deposition properties and the respective changes of the global annual dry deposition due to the extended scheme. Insoluble (semi-reactive) compounds are predicted to be removed with deposition velocities in the range of 0-0.4 cm s^{-1} where the maximum values occur in the high vegetated regions of tropical forests (Fig. 4.3a). This result indicates that the main deposition happens to vegetation, as it can be expected from its low propensity to interact with surfaces. The modified dry deposition scheme leads to a 30-50 % decrease (Fig. 4.3b) at the whole globe due to stomatal stress. Compounds with high solubility (see the lower part of Tabl 4.2) show substantially higher deposition on the whole globe (Fig. 4.4a), as also indicated by measurement studies (Karl et al., 2010; Nguyen et al., 2015). The global distribution reflects not only deposition to vegetation. Due to their interaction with surfaces, the compounds likely deposit also to soil and snow. The explicit parametrisation of the cuticular scheme doubles the dry deposition velocity in all vegetated areas (Fig. 4.4b) while the stomatal stress likely leads to minor contributing counter-balancing effects. As the importance of the cuticular pathway increases with vegetation (see Eq. 3.3) and relative humidity, the change is highest in boreal forests. The wet season (high humidity) additionally features the favoured conditions. The global annual dry deposition of the soluble OVOCs increases by 10-25 % due to the modified parametrisation.

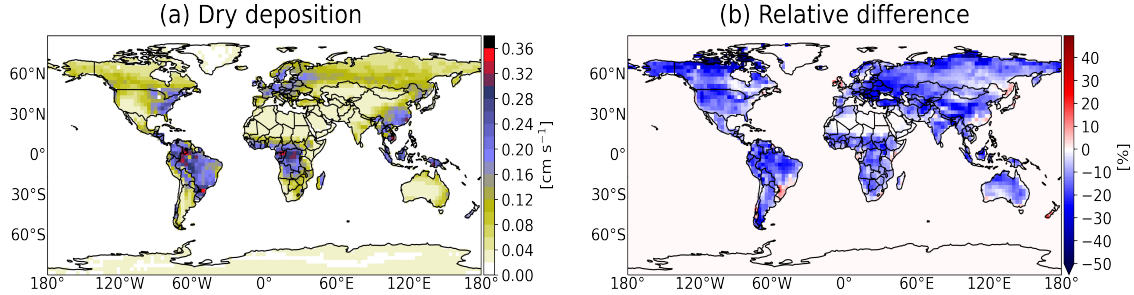

Figure 4.3: Annual mean (a) dry deposition velocity (EMACref) and the (b) relative difference (EMACddep-EMACref) of a set of insoluble (semi-reactive) OVOCs (average).

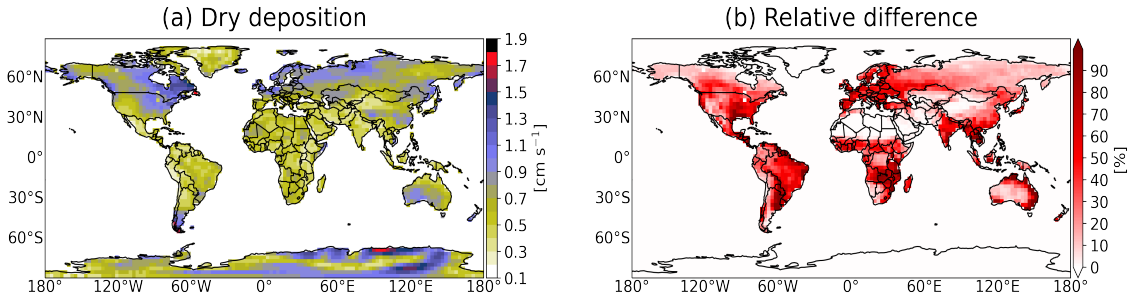

Figure 4.4: Annual mean (a) dry deposition velocity (EMACref) and the (b) relative difference (EMACddep-EMACref) of a set of soluble (semi-reactive) OVOCs (average).

Table 4.2: List of OVOCs, the diffusivity in air ($\frac{D(X)}{D(H_2O)}$), the effective solubility (H(X) in [M atm^{-1}]), the global annual dry deposition (in [Tg(C) a^{-1}]) and the change by EMACddep. All compounds are considered as semi-reactive (f= 0.1), the upper part as insoluble, the lower part as soluble compounds.

Compound	$\frac{D(X)}{D(H_2O)}$	H(X)	EMACref	ΔEMACddep (Δ%)
Acetaldehyde	1.6	13	2.1	-0.2 (11)
Peroxyacetyl nitrate (PAN)	2.6	2.8	1.2	-0.07 (14)
Acetone	1.8	30	0.1	-0.03 (21)
Methylvinylketone (MVK)	2.0	23	3.8	-0.02 (7.0)
Methyhlethylketone (MEK)	2.0	20	0.3	-0.6 (15)
Methylbutenol (MBO)	2.1	1×10^6	0.1	+0.03 (27)
Hydroxymethyl hydroperoxide (HMHP)	1.9	1.7×10^6	0.3	+0.07 (25)
Formic acid	1.6	6.7×10^6	2.0	+0.5 (24)
Glyoxylic acid	2.0	6.6×10^7	0.1	+0.03 (21)

4.2 Impact on the tropospheric composition

The enhancement of dry deposition is much higher for soluble than for insoluble VOCs. The two major atmospheric sinks of VOCs, the oxidation by OH and the photolysis, are subsequently reduced for most of the globe. To link the changed dry deposition flux of soluble OVOCs (ΔsOVOC ddep) to the chemical composition, the (Pearson) correlation in the PBL is derived throughout the year. Thereby, a p-value of 0.05 indicates the significance level. The increased OVOC dry deposition flux appears to be negatively correlated to the change of radical propagation (RO_2, HO_2, CH_3O_2 +NO) (Fig. 4.5a). This indicates that the enhanced dry deposition causes a decrease in the radical reaction rate, mainly in the NH. No significant correlation (or correlation=0, white coloured) is found where small dry deposition changes due to balancing effects occur, such as in the Amazon forest. When considering the whole troposphere, the significance of the correlation is less widespread than in the PBL.

The weaker radical propagation rate limits the NO−to−NO_2 conversion yield. This also affects the back-conversion, as Fig. 4.5b shows the sole change in NO_2 photolysis under identical meteorology in EMACref and EMACddep. The NO_2 photolysis rate is reduced in all vegetated areas except the inner tropics. Both lower NO_2 production and the direct increase of NO_2 dry deposition concur to this reduction, which shifts the NO:NO_2 ratio towards NO. The decrease of more than -100 ppb d^{-1} is highest in Europe.

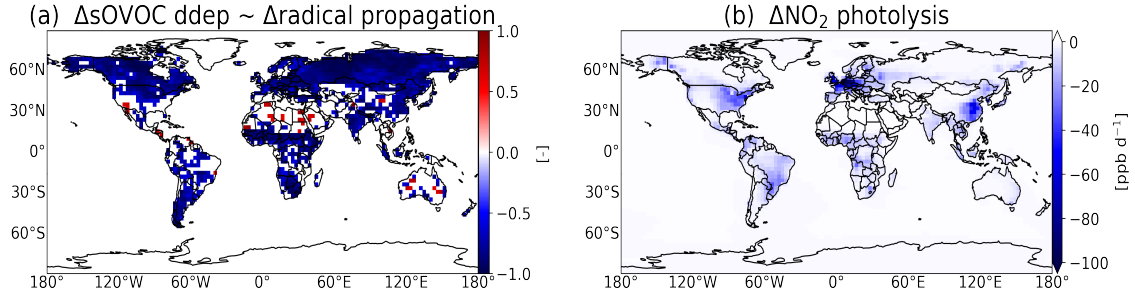

Figure 4.5: Annual mean (a) correlation of the changed dry deposition of soluble VOCs towards the change of radical propagation and (b) the change of the NO_2 photolysis rate in the PBL.

Higher VOC deposition fluxes generally result in weaker HO_x production (reduced photolysis), which is most pronounced in the tropics. In low NO_x tropical regions, this is ruled out by the reduced HO_2 loss reaction with O_3 while in industrial area (e.g. Europe) the loss by NO predominantly counteracts. These effects are reflected by the change of net O_x loss ($L(O_x)$: HO_2, OH $+O_3$, Fig. 4.6b). However, the about one order higher decrease of the radical propagation initiating the O_3 production dominates as the net-O_x production ($P(O_x)$: RO_2, HO_2, CH_3O_2 +NO) shows (Fig. 4.6a). Up to 3 ppb d^{-1} less O_x is produced between 0° and 30°S where the change of the radical production (not shown) is most pronounced across the globe. Another major reduction occurs in East Asia where photochemical activity is comparably lower than in the tropics/subtropics.

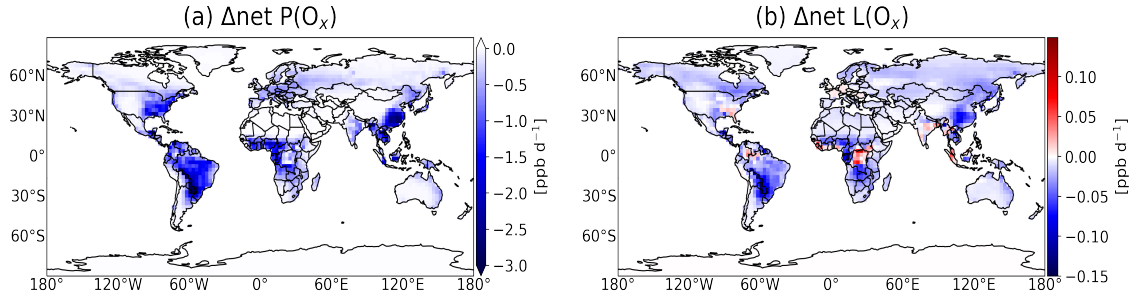

Figure 4.6: Annual mean absolute change (a) of the net $P(O_x)$ ($\frac{dO_x}{dt}$) and (b) of the net $L(O_x)$ at the surface.

Whether the O_3 production by the radical propagation ($P(O_x)$: HO_2,RO_2,CH_3O_2 + NO) dominates over the NO_x loss (HNO_3 production, heterogeneous formation

of N_2O_5) becomes apparent in Fig. 4.7 which represents the ratio of the respective reaction rates. This is one definition of the O_3 production efficiency (OPE, Eq. 2.24) which, however, is limited in complexity against other definitions (Wang et al., 2018). Under low-NO_x conditions (NO_x-limited), the radical propagation dominates leading to high ratios around 40, also reported in literature (Wang et al., 2018). The minima close to 0 occur in industrial areas influenced by strong anthropogenic NO_x sources (e.g. East Asia, Europe) where OH radicals react increasingly with NO_2 instead of oxidising VOCs (see Seinfeld and Pandis (2016)). Applying the extended dry deposition scheme affects the above-mentioned reaction rates differently depending on the regional conditions. Over tropical forests, the reduction of $P(O_x)$ dominates the decrease of the loss, and thus the OPE is increased by up to 30 % (Fi. 4.7b). In the NH, these terms are (almost) balanced due to the higher reduction of NO_x (also by higher deposition). Thereby, the decrease of N_2O_5 contributes in Europe, East U.S. and East Asia. In general, the change is largest at the surface, slightly decreasing if higher altitudes are considered (up to the tropopause).

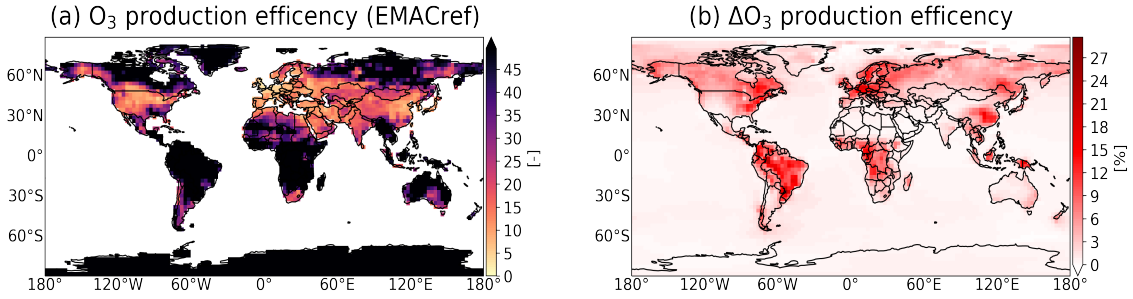

Figure 4.7: Annual mean (a) O_3 production efficiency (EMACref) and (b) the absolute change by EMACddep (EMACddep-EMACref).

The OPE measures the number of O_3 molecules which are formed per NO_x removal from the system (deposition and scavenging of HNO_3). The change of the annual mean NO_x surface mixing ratio is shown in Fig. 4.8a. Corresponding to the dominance of the OH+NO_2 reaction (low OPE) the surface mixing ratio is reduced (20 %) in the tropics. The increase of OPE with decreasing NO_x in unpolluted conditions has been reported by multiply studies (Wang et al., 2018, and references therein). The NO_x changes in Europe and further NH regions by down to 200 ppt can be attributed to enhanced dry deposition of NO and NO_2. The change in O_3 mixing ratio (Fig. 4.8b), overall, can be inferred from the decreases of the O_x budget terms considering also the enhanced OPE. Although the decrease of radical reactions initiating the O_3 production is highest in the tropics, the production efficiency per removal of NO_x is increased. These counteracting effects explain the relative low decrease of O_3 mixing ratio in the SH tropics. In the NH, the O_3 decrease follows mainly the enhanced dry deposition of O_3 and NO_x. The O_3 changes are in the range of 5-10 %.

The comparison of the model results with TOAR measurement data and the changes by EMACddep in JJA, when dry deposition has the highest impact on O_3, is shown in Fig. 4.9. The initial O_3 bias of EMACref is about 5 ppb higher during night than

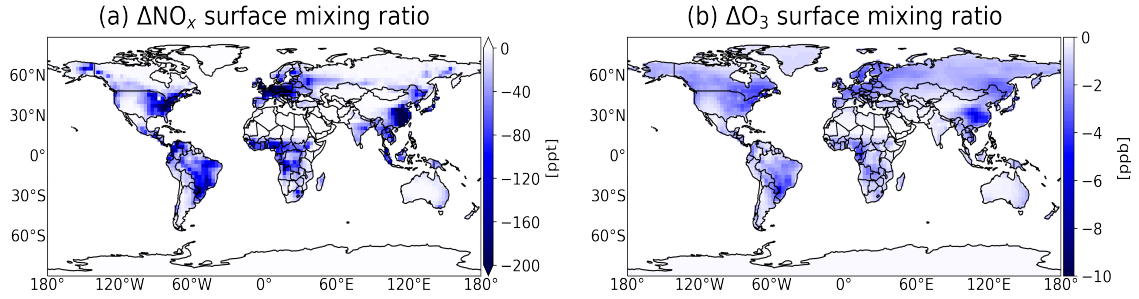

Figure 4.8: Annual mean absolute change (a) of the NO_x (b) and O_3 surface mixing ratio.

at day-time for almost all observation sites (Figs. 4.9a, c). Applying the extended dry deposition scheme decreases the overestimation of EMAC to the TOAR observations by about 10-20 % towards a remaining discrepancy of ± 5-10 ppb (Figs. 4.9b, d). The relative change is more important during the night as it has been shown for O_3 uptake, which points to dry deposition as a missing process in the standard configuration of EMAC (here: EMACref). The mean discrepancy between all TOAR O_3 measurements and the model results of 11 ppb is reduced by 13 % for 2009. The reduction differs between Europe and the USA, where the main part of the TOAR data is located. In Europe, the annual bias is lowered by almost a factor of 2. The remaining discrepancy of 2.8 ppb is considered as being within the measurement uncertainty. In the warmer and dryer climate of the USA when stomata are more stressed and the cuticular uptake is less favoured, the change is only -20 %.

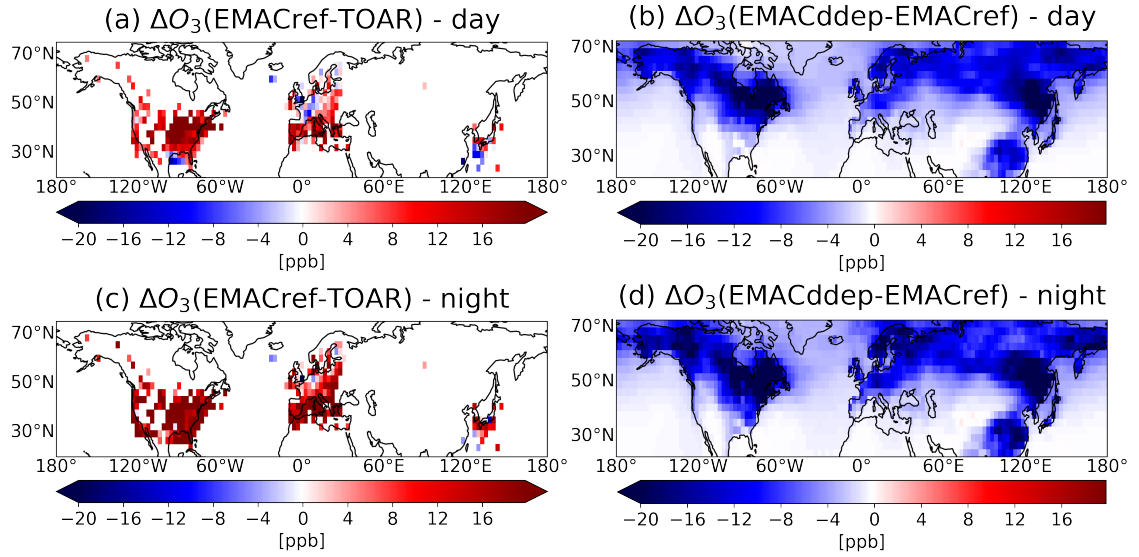

Figure 4.9: Boreal 2009 summer mean absolute difference of the surface O_3 mixing ratio comparing EMACref to TOAR (a, b) and the relative change to EMACddep (c, d) during day and night, respectively.

The impact of dry deposition trace gas mixing ratios generally decreases towards the free troposphere. Dry deposition accounts for one-third of the O_x removal in the PBL

while only 16 % for the whole troposphere. Here, the zonal mean relative difference of tropospheric O_3 due to the modified dry deposition is shown in Fig. 4.10. For O_3, the maximum reduction of -10 % occurs in the NH surface layers, decreasing up to the tropopause. The change diminishes towards the equator, where the impact of the stomatal temperature stress counter-balances the enhanced cuticular uptake. The changes south of the equator mainly reflect the secondary role of dry deposition to the land surface, as the SH is mainly covered by ocean. Accordingly, the comparison of the simulated O_3 with the lower tropospheric column (up to 300 hPa) retrieved by IASI is not impacted significantly on monthly average (ΔO_3 bias < 5 %).

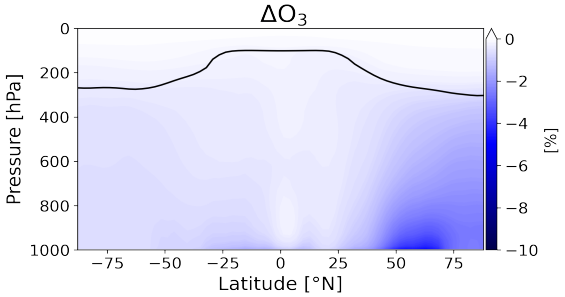

Figure 4.10: Zonal mean relative difference of tropospheric O_3. The annual mean tropopause is depicted by a black line.

4.3 Discussion

The prognostic model used here for the stomatal dry deposition is applied commonly in global Earth system models (Simpson et al., 2012; Myriokefalitakis et al., 2020) due to its simplicity and adaptability. The multiplicative approach by Jarvis (1976), however, has some drawbacks. For instance, it assumes independent environmental responses and relies on empirically derived parametrisations. Photosynthetic models which get more popular, in contrast, use a more mechanistic approach. They couple the stomatal behaviour with the net assimilation of CO_2 during plant's photosynthesis (Ran et al., 2017; Clifton et al., 2020). In contrast to the prognostic model, such a approach relies on many plant physiological details, which are not always available from the model in use. Also, the higher amount of parameters account for additional uncertainty sources. Both model frameworks show improvements and uncertainties at different locations (Lu, 2018). For the cuticular pathway, most models use predefined constants, as it is also the standard in EMAC. However, by this, the variability of the process is neglected. The inclusion of an explicit representation depending on meteorological and environmental variables bridges this gap. In particular, strong evidence for cuticular O_3 uptake dependent on relative humidity is considered. Since it is independent of daylight, the parametrisation represents an important contribution to dry deposition during the night. However, the empirical approach relies on parameters fitted for a few measurement sites and is generalised to the global scale (Zhang et al., 2002). Dry deposition fluxes of NO_2 predicted by

EMACddep might be overestimated according to observations which only reveal dry deposition velocities comparable to O_3 when low soil emissions of NO occur. In fact, the rapid photochemical reaction of O_3 with the emitted NO forming NO_2 might diminish the total dry deposition of NO_2. Moreover, it is unclear if a compensation point for the NO_2 concentration in trees, varying among different compounds, exists and should be included in the dry deposition model (Wesely and Hicks, 2000, and references therein). Dry deposition estimates by Archer-Nicholls et al. (2021) agree more with the results of EMACref. The significant increase of (soluble) OVOC deposition due to the modified dry deposition scheme shown here improves the model performance against flux measurements. In general, high OVOC deposition velocity at mid-latitude forests (and tropical) have been observed. Dry deposition of insoluble compounds seems to be underestimated in comparison to measurements where e.g. MVK has been observed to deposit at similar velocities as for O_3 (1-2 cm s^{-1}) (Karl et al., 2010; Nguyen et al., 2015). An explanation for the efficient deposition has been proposed by Karl et al. (2010) who found that plants metabolism responds to environmental changes, such as acute chemical exposure. As protection, they increase the activity of OVOC removal, which is one responsible process for plant detoxification. Increasing the surface reactivity parameter in models to the maximum as for O_3 (f=1, Eq. 2.7, 2.8) could account for this fast metabolic conversion (Karl et al., 2010). Although this mechanistic behaviour of plants is reported also by other studies, more field measurements of OVOC deposition are needed to confirm this proposal. Anyway, accounting for enhanced surface reactivity of OVOCs will further reduce the predicted production and levels of tropospheric O_3 in EMAC.

Model estimates of the global O_3 dry deposition are in a wide range from 710-1470 Tg a^{-1}. However, dry deposition has the largest uncertainty among the O_3 budget terms due to the uncertainties of model approaches, observational constraints, land cover data and knowledge gaps (Young et al., 2018; Hardacre et al., 2015). Also, the model representation of meteorology, which drives the local variation of dry deposition, might be a non-negligible uncertainty source as indicated by e.g. Emmerichs et al. (2021). The here calculated global dry deposition flux of O_3 lies within the range of current model estimates, but the modification yields no significant improvement (only 3 %) towards the most recent multi-model estimate of 1000 Tg a^{-1}. One reason for this small change is certainly that the modelled deposition flux is directly proportional to the trace gas mixing ratio, which decreases for O_3 with the revised parameterisation. Hence, this calculation may not represent the appropriate measure to assess the changes by dry deposition. The representation of O_3 dry deposition could be further improved by explicitly representing O_3 deposition to soil, which several measurement studies report as an important pathway (e.g., Fares et al., 2012; Stella et al., 2011). Moreover, it is known that due to a dry bias (too dry soil and too high temperature) in the Amazon basin for the base model of EMAC (Hagemann and Stacke, 2015), the dry deposition is underestimated substantially in this area. As tropical forests are very relevant for the global magnitude of dry deposition, this is a critical aspect for the dry deposition modelling (Emmerichs et al., 2021).

5 Global modelling of water-radical complexes

Here, the global impact of the water vapour on radical reactions important for O_3 chemistry is investigated. Kinetics and product distribution for three different radical reactions (HO_2+NO, RO_2+NO and OH+NO_2), have been modified to be affected by humidity as suggested by previous studies. These effects by water vapour on gas kinetics are usually not considered in global models and their overall impact is assessed with the simulation labelled EMACh2o.

5.1 Modified kinetics

In the chemical mechanism of MECCA by Sander et al. (2019) the reaction of HO_2+NO yields solely NO_2 and OH (see Reaction 2.14) with a rate constant that is only temperature-dependent (T in [K]). Following the NASA/JPL kinetic data evaluation no. 18 (Burkholder et al., 2015), which bases this recommendation on eight studies at room temperature and below, the rate constant is:

$$k_{HO_2+NO} = 3.3 \times 10^{-12} \cdot \exp\left(\frac{270}{T}\right). \tag{5.1}$$

However, Butkovskaya et al. (2005) first reported about experimental kinetic data supporting a second channel for Reactio 2.14 yielding nitric acid (HNO_3) under dry conditions:

$$HO_2 + NO \rightarrow HNO_3 \tag{5.2}$$

This channel is enhanced by water vapour which is known to form the $HO_2{\cdot}H_2O$ complex:

$$HO_2 \cdot H_2O + NO \rightarrow HNO_3 + H_2O \tag{5.3}$$

First, Reaction 5.2 is added with the branching ratio after Butkovskaya et al. (2007). Following indications by Butkovskaya et al. (2009) and Gottschaldt et al. (2013), this is replaced by a different rate constant (k_{1w,HO_2+NO}) allowing for the formation of the hydrogen bonded $HO_2{\cdot}H_2O$ complex. A new rate constant is defined as:

$$k_{1w,HO_2+NO} = k_{0,HO_2+NO} - k_{2w,HO_2+NO} \tag{5.4}$$

where k_{0,HO_2+NO}, recommended by Sander et al. (2003), is very similar to k_{HO_2+NO}. k_{2w,HO_2+NO} describes the second channel of the HO_2+NO reaction forming HNO_3,

which is significant in humid conditions. Neglecting the water impact, the HNO_3 yield is only a small fraction of the total reaction (Butkovskaya et al., 2009). The rate constant for the HNO_3-formation channel, firstly added to EMAC by Gottschaldt et al. (2013), is described as:

$$k_{2w,HO_2+NO} = \frac{\beta \cdot k_{0,HO_2+NO} \cdot (1 + 42 \cdot \alpha)}{(1+\alpha) \cdot (1+\beta)} \cdot \frac{1}{2} \tag{5.5}$$

As reported by JPL (Burkholder et al., 2020), β describes a pressure (p in [Pa]) and temperature dependence valid for dry conditions in the pressure range 93–800 hPa and the temperature range 223–298 K, which have been determined by an empirical fit of laboratory data (Butkovskaya et al., 2007). The water complex is considered by including α, which additionally depends on the atmospheric concentration of water vapour (H_2O) and the equilibrium coefficient of the HO_2-water complex (K_{eq} in [cm^3]) (Gottschaldt et al., 2013; Butkovskaya et al., 2009).

$$\beta(p,T) = 0.01 \cdot \left(\frac{530}{T} + p \cdot 4.8 \times 10^{-6} - 1.73\right) \tag{5.6}$$

$$\alpha = [H_2O] \cdot K_{eq}, \text{with } K_{eq} = 6.6 \times 10^{27} \cdot T \cdot \exp(\frac{3700}{T}) \tag{5.7}$$

In contrast to e.g Gottschaldt et al. (2013), a 2-fold lower rate constant k_{2w,HO_2+NO} is used here according to a study characterising a Chemical Amplifier instrument for measuring peroxy radicals (Duncianu et al., 2020). By applying a 2-fold lower reaction rate to a box model Duncianu et al. (2020) have achieved a better agreement with the measured data, which was significantly underestimated before. This study represents the first, but indirect confirmation of the water dependence reported by Butkovskaya et al. (2009) although with a water effect half as strong.

The potential formation of water complexes in reactions of organic peroxy radicals has been suggested in a few studies (Kumbhani et al., 2015; Clark et al., 2010). It has been indicated that during the oxidation of methacrolein (MACR) substituted RO_2-water complexes might yield a unity alkyl nitrate when reacting with NO. This would be consistent with a relatively high equilibrium constant for the complexation of water with the first alkyl peroxy radical from MACRO2. Based on the data determination for MACRO2 by Xing et al. (2018), the water-dependence effect is implemented here for all substituted RO_2 assuming the same behaviour as MACRO2. The branching ratio for the RO_2+NO reaction forming alkyl nitrates is calculated as follows:

$$\alpha_{AN}(T, cair) \times f_{\mathrm{RO_2}} + (1 - f_{\mathrm{RO_2}}) \tag{5.8}$$

The dry alkyl nitrate yield (α_{AN}) depends on temperature, pressure and the concentration of air molecules ($cair$) (Sander et al., 2019), and is about 0.03 for MACRO2. In order to account for the water dependence, Equation 5.8 is extended by the portioning of RO_2-water (1-$f_{\mathrm{RO_2}}$) complexes and non-complexed RO_2 here. According to Xing et al. (2018), $f_{\mathrm{RO_2}}$ is defined as:

$$f_{\mathrm{RO_2}} = \frac{1}{(K_{eq,\mathrm{RO_2}} * [H_2O] + 1)}, \text{with } K_{eq,\mathrm{RO_2}} = 1.89 \times 10^{-18} \tag{5.9}$$

Recently, experimental evidence for the water enhancement of the OH+NO_2 reaction rate (Reactio 2.18) has been published. This reaction yields HNO_3 and peroxynitrous acid (HOONO). Amedro et al. (2020) have demonstrated that water molecules are six times more efficient than N_2 at quenching the HO-NO_2 complex. To account for this effect, the original rate coefficient Amedro et al. (2019, Eq. 5)) is extended according to Amedro et al. (2020, Eq. 15). The rate coefficient also includes the collision efficiency (β_i of the respective gas i) for energy transfer from the initially formed HO+NO_2 association complex to H_2O.

$$k_1(p,T) = \frac{\beta k_0 \left(\frac{T}{300}\right)^{-m} M k_\infty \left(\frac{T}{300}\right)^{-n}}{\sum \beta k_0 \left(\frac{T}{300}^{-m}\right) M + k_\infty \left(\frac{T}{300}\right)^{-n}} \cdot F, \text{with } \beta = \sum \beta_i x_i \tag{5.10}$$

where k_0 and k_∞ are the low-pressure [cm^6 $molecule^{-2}$ s^{-1}] and the high-pressure [cm^3 $molecule^{-1}$ s^{-1}] limit rate coefficient. M is the density [molecule m^{-3}], F the broadening factor and m and n are dimensionless temperature exponents.

5.2 Simulation results

To assess the global impact of the water-radical complexes the modified kinetics of the OH+NO_2 and the NO+RO_2/HO_2 reactions are applied in the sensitivity simulation EMACh2o. The impact on the tropospheric composition is analysed by the means of passive tracers and the calculated global O_x budget (Tabl 5.1).

The modification of the radical kinetics allows for the complexation of radicals with water molecules and firstly includes the water enhancement for the formation of HNO_3 from the HO_2+NO reaction. This modification has significant impacts on the O_x chemistry in the PBL and the whole troposphere. Figure 5.1 shows the seasonal mean relative difference of the HO_2+NO reaction rate (major channel) between EMACh2o and EMACref in austral summer (DJF: December-February) and boreal summer (JJA: June-August). The rate of the original HO_2+NO channel producing OH and NO_2 at the surface decreases in most areas since it competes with the newly introduced HNO_3-forming channel. The HNO_3 production is generally favoured at cold temperature and high humidity (see also Gottschaldt et al. (2013)). Thus, the highest decrease of the HO_2+NO reaction rate occurs in the tropics, relatively similar in both seasons. In the SH, also NO_2 photolysis is reduced as consequence of the weakened HO_2+NO reaction rate which strengthens the reaction decrease. An increase in the HO_2+NO reaction rate occurs at polar circles, where mainly night-time chemistry takes place during the respective winter (dark) seasons. Less NO is converted to NO_2 due to the overall decreasing O_3 levels (described later), which feeds back to the HO_2+NO reaction. During the entire year, the modified reaction kinetics account overall for a 25 % reduction of the HO_2+NO reaction rate in the global troposphere (see Tabl 5.1). The HNO_3 yield at the surface is shown to increase in most regions. Consequently, the increase on the NH is relative small in boreal summer compared to winter (Fig. 5.1c). This demonstrates that the added HNO_3

Table 5.1: $O_x$budget gross terms of the reference simulation (EMACref in [Tg a^{-1}]), calculated for the troposphere and the PBL, and relative changes induced by the sensitivity simulation EMACh2o (in [%]).

	Troposphere		**PBL**	
	EMACref	ΔEMACh2o	EMACref	ΔEMACh2o
Sources [Tg a^{-1}]				
Chemical production	5550.6	-20.0	1596.3	-19.8
HO_2+NO	3823.0	-24.9	950.5	-20.2
CH_3O_2+NO	1060.3	-23.0	313.4	-22.1
RO_2+NO	643.9	-12.8	326.7	-25.2
HONO+OH	0.94	-34.0	0.35	-31.4
STE[a]	508.9	+18.5		
Sinks [Tg a^{-1}]				
Chemical loss	4990.8	-16.6	1246.3	-20.8
$O(^1D)$+H_2O	2268.4	-16.1	669.1	-15.8
HO_2+O_3	1575.7	-16.3	322.8	-19.1
OH+O_3	673.1	-31.2	115.7	-29.7
Dry deposition	825.2	-14.2	825.2	-14.2
O_3	780.2	-15.0	780.5	-15.0
NO_2	7.3	-2.7	7.3	-2.7
Scavenging	243.5	-6.9	45.3	-3.5
O_3 burden [Tg]	394.0	-12.0	28.8	-14.6
O_3 lifetime [days]	23.7	+5.5	5.0	0

[a]Difference of source and sink terms, definition not valid for PBL

channel is of minor importance when the reaction is not affected by water vapour as reported by e.g. Butkovskaya et al. (2009). Higher humidity amplifies the effect enhancing the HNO_3 surface mixing ratio by up to 40 % (Fig. 5.1d). However, the increased HNO_3 yield only dominates where the NO_x recycling is sufficiently higher than its removal (see Fig. 4.7). Then, the enhancement of the HNO_3 formation by the HO_2+NO reaction exceeds the reduction of the additional production via OH+NO_2 and the heterogeneous N_2O_5 loss (to HNO_3, $L_{het}(N_2O_5)$). As the weakened HO_2+NO reaction rate decreases NO_2 and thus also N_2O_5 which cause the reduction of the OH+NO_2 reaction and the heterogeneous N_2O_5 loss (to HNO_3, $L_{het}(N_2O_5)$). The relative increase of the HNO_3 yield is most dominant in the tropics due to the high abundance of water vapour and strong photochemical activity. The decrease of the HNO_3 oxidation is highest in the Central Amazon due to the lowered OH yield from the HO_2+NO reaction, which additionally explains the local maximum. A further reason might be that the local dry deposition, which is the main sink of HNO_3, is relatively small compared to other regions due to the dry model bias in the Amazon (Hagemann and Stacke, 2015).

The weakening of the NO_2-production (and the enhancement of the HNO_3-formation) from the HO_2+NO reaction has regionally different effects for the NO_x levels at the

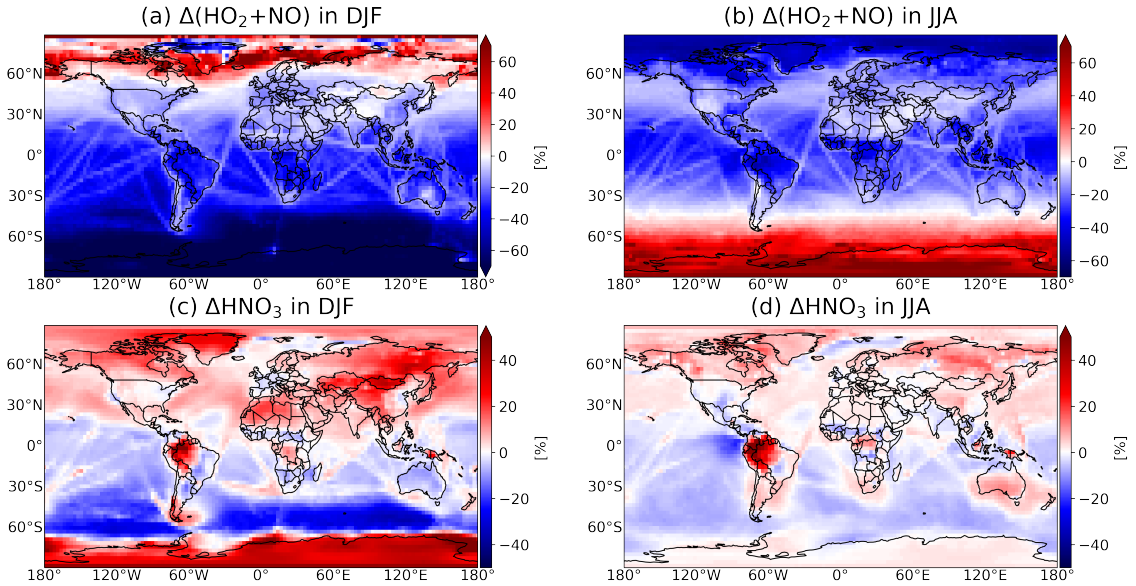

Figure 5.1: Seasonal mean relative difference of the HO_2+NO reaction rate and the HNO_3 mixing ratio (a, c) in DJF and (b, d) JJA, respectively.

surface. In general, HNO_3 represents a net sink for NO_x because its deposition is much faster than the one of NO and NO_2. Thus, an increased HNO_3 yield corresponds to lowered NO_x levels when comparing EMACh2o and EMACref (Figs. 5.2a, b). The strength varies due to the temperature and humidity dependence of the reaction rates across the seasons. This impact is, however, counter-balanced by the decrease in HO_x. Due to its long lifetime of up to 10 days, HNO_3 can also undergo long-range transport. Indeed, the additionally produced HNO_3 in EMACh2o is transported from the South America to the tropical Oceans, yielding 10-30 % decrease of NO_x there. In addition, the heterogeneous loss of continental N_2O_5 transported over the ocean is more efficient than over the continents and thus likely contributes to the NO_x decrease over the tropical Oceans (Fig. 5.2c, d). An increase of NO_x, in contrast, occurs over highly polluted regions such as Europe, the U.S. and East Asia. There, the decrease of the OH+NO_2 reaction caused by the weakened NO_2 recycling dominates also the impact on NO_x. In fact, this reaction removes less NO_x from the atmosphere (Figs. 5.2a, b). The increase is more pronounced in DJF than in JJA because the rapid NO_x loss through N_2O_5 ($L_{het}(N_2O_5)$) decreases (in the NH) less in DJF than in JJA due to its humidity dependence (Figs. 5.2c, d).

The overall OH decrease and the reduced oxidation capacity of the atmosphere, which agrees with the findings by Gottschaldt et al. (2013), also contributes to the changes in the computed O_x budget. In fact, the oxidation rate of CH_4 decreases, which explains the lower (annual) O_3 production via the CH_3O_2+NO reaction globally (Tabl 5.1). The highest relative change among the O_x production terms is estimated for the reaction of OH+HONO decreasing the NO_2 formation which, however, contributes only minor to the overall chemical production.

The contribution of the RO_2+NO reaction to the O_x production is also reduced by

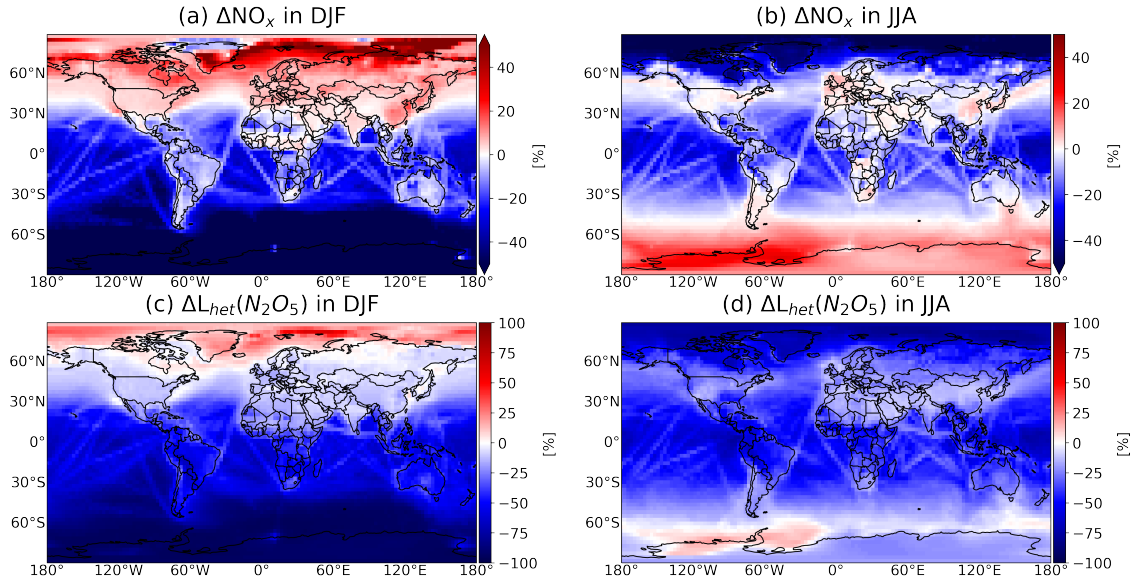

Figure 5.2: Seasonal mean relative difference of the NO_x mixing ratio and the heterogeneous N_2O_5 loss reaction (a, c) in DJF and (b, d) JJA, respectively.

25 % in the PBL (20 % for the whole troposphere). In the PBL, the reduction even exceeds the change of the major O_x production reaction, HO_2+NO. As the RO_2+NO reaction produces either one alkyl nitrate (minor branch) or leads to the formation of two O_3 molecules (major branch) the average yield of alkyl nitrates ($\sum$ AN[1]) can be correlated to O_3 in the field data (Day et al., 2003). Enabling the formation of water-radical complexes in the RO_2+NO reactions is known to increase the alkyl nitrate production while the major branch (and thus the O_3 production) is inhibited (see Sect. 5.1). The change of the alkyl nitrate production is assessed here by considering dry deposition as direct sink. As the high water solubility of the hydroxyalkyl nitrates, an important alkyl nitrate group, allows for rapid dry deposition (Day et al., 2003, and references therein). Applying the modified kinetics increases the $\sum$AN dry deposition significantly from 0.35 to 0.96 Tg(N) a^{-1} (2.7 and 7.9 Tg a^{-1}). The enhanced abundance is here calculated exemplary for two ANs. For i$-C_3H_7NO_3$ and n$-C_3H_7NO_3$, the global burden is increased by 77 % to 65.7 and 43.8 Gg, respectively. The increase in the alkyl nitrate yield is an enhancement of radical termination that consequently decreases O_3 production. The changed HO_x and NO_x levels as a consequence of the modified HO_2+NO reaction kinetics additionally influence the change of the RO_2+NO reaction, regionally different. The increase of the NO_x levels in the polluted regions raises all NO_x reactions, in general, while the reduced NO_x levels on the SH strengthen the decrease of the RO_2+NO reaction. The inclusion of the water enhancement in the OH+NO_2 reaction is likely contributing to the O_3 changes in the tropical PBL (Amedro et al., 2020). In fact,

[1] $\sum AN$ =BZBIPERNO3, PROPOLNO3, LBUT1ENNO3, BZEMUCNO3, IBUTOLBNO3, ISOPBNO3,ISOPDNO3, LAPINABNO3, BPINANO3, IC3H7NO3, NC3H7NO3, C514NO3, LMBOABNO3, C614NO3, C6H5CH2NO3, TLBIPERNO3, TLEMUCNO3 (as defined in MOM)

Amedro et al. (2020) shows that the OH+NO_2 rate coefficient is underestimated in the warm tropics by 8 % when the water impact is not considered.

Taking all these effects into account, the annual mean surface O_3 is reduced on the whole globe due to the changes of NO_x and HO_x levels. In the highly polluted NH regions, the opposite changes of NO_x and HO_x contrast with a O_3 decrease of up to -15 % at the surface. The reduction is significantly higher in the entire SH, where the weakening of the original HO_2+NO is favoured. About a two-fold decrease of surface O_3 is computed over the Central Amazon (Fig. 5.3a). Consequently, the comparison of modelled surface O_3 to the TOAR data improves towards a small discrepancy of ± 4 ppb (Fig. 5.3b) among all considered stations which is close to the measurement uncertainty (≈2 ppb). The decrease is higher in Europe than in the U.S. as the impact of the water-radical formation increases with humidity. Thereby, the surface O_3 mixing ratios predicted by EMACh2o match almost the observed values during the year. In the U.S., the simulated annual cycle is represented well in the first half of the year, while the monthly mean values of July to November are overestimated. Considering the spatial dependence of the bias, the highest mismatch remains in suburban coastal grid boxes where an accurate representation of abundance is notoriously challenging since the steep concentration gradients from land to ocean (stronger during daytime) are not resolved in models (Fiore et al., 2002). According to the lower O_3 and HO_x abundances also the chemical loss terms of O_x decrease, however, less compared to the production resulting in a net decrease of O_x globally.

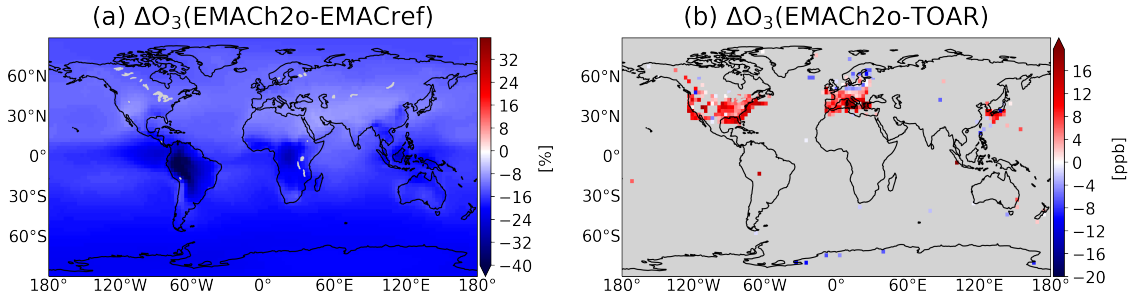

Figure 5.3: Annual mean surface O_3 (a) relative difference (EMACh2o- EMACref) and (b) the remaining bias of EMACh2o towards TOAR.

While the impact of the introduced water effects is most important at ground level, the inclusion of the dry HNO_3-formation channel affects the higher troposphere. Indeed, the highest branching ratio of the HNO_3-formation channel occurs in the cold tropical upper troposphere/lower stratosphere (UTLS) (Gottschaldt et al., 2013). This explains the local maximum of the zonal mean relative difference when comparing EMACref and EMACh2o in Fig. 5.4a, as it has also been reported by Gottschaldt et al. (2013). In the lower layers up to 400 hPa the spatially varying responses counter-balance to an overall small change. The high increase of surface HNO_3 in the central Amazon disappears in the zonal mean. Within the overall troposphere, only the low temperature in the southern and northernmost regions, favouring the

HNO_3 production, occur to be of importance. Due to the temperature dependence, the changes are more pronounced in the respective cold seasons. In contrast, the decrease of the OH levels by up to 30 % throughout the whole troposphere corresponds to the described effects at the surface (Fig. 5.4b). The highest changes occur in the tropics and the SH. The peak in the tropical UTLS corresponds to the maximum of HNO_3 as also shown by Gottschaldt et al. (2013). But the OH change is generally not height-dependent and occur relatively similar at all altitudes up to the tropopause, which might reflect the speed-up of the $OH+NO_2$ reaction. In fact, the reaction with NO_2 depicts a sink term for OH molecules, which becomes more important in the higher troposphere (Amedro et al., 2020). Similar to OH, the zonal mean relative difference of O_3 shows a decrease of up to 30 %, relatively uniformly at all layers (Fig. 5.4c). Above the tropopause, the impact of the water-radical complexation diminishes. On the SH, the reduction is generally larger than on the NH due to the higher water vapour abundance and the greater role of the radical propagation reactions for the O_3 chemistry.

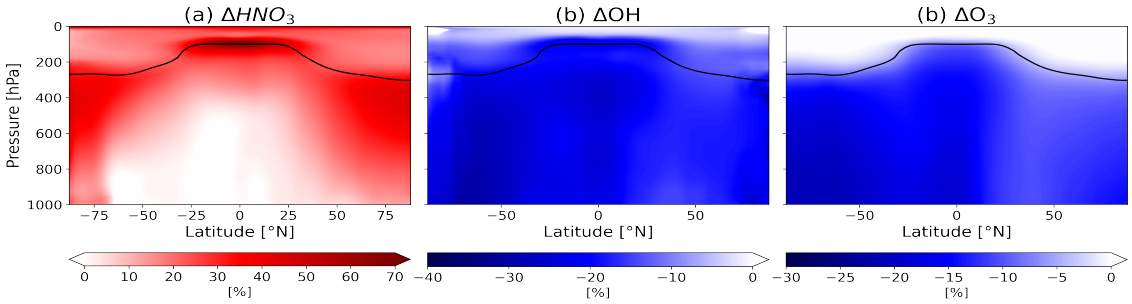

Figure 5.4: Zonal mean relative difference (EMACh2o vs. EMACref) for mixing ratios of HNO_3 (a), OH (b) and O_3 (c) in the atmosphere. The annual mean tropopause is depicted by a black line.

To also evaluate the effects on tropospheric O_3, we compare the simulated values with observations by IASI in the lower tropospheric column (up to 300 hPa). Initially, the model overestimates the lower tropospheric O_3 column from IASI by 4-12 DU (40°N–40°S) as shown in Fig. 5.5a. This is at the lower end of the most recent estimates from EMAC evaluation studies (Jöckel et al., 2016; Rosanka et al., 2021b). Allowing for the water enhancement of the NO_x reactions mentioned above the annual mean tropospheric column O_3 in this region is reduced by 10-15 % (Fig. 5.5b) with the highest changes in the tropics as also seen at the surface. Globally, the reduction of the average bias amounts 30 %. The remaining discrepancy between EMACh2o and IASI (Fig. 5.5c) exceeds the measurement uncertainty only in a few regions, such as over the tropical Pacific.

5.3 Discussion

The modification of the radical reactions driving the O_3 production includes the important dependence on water, based on the most recent findings. The impact of

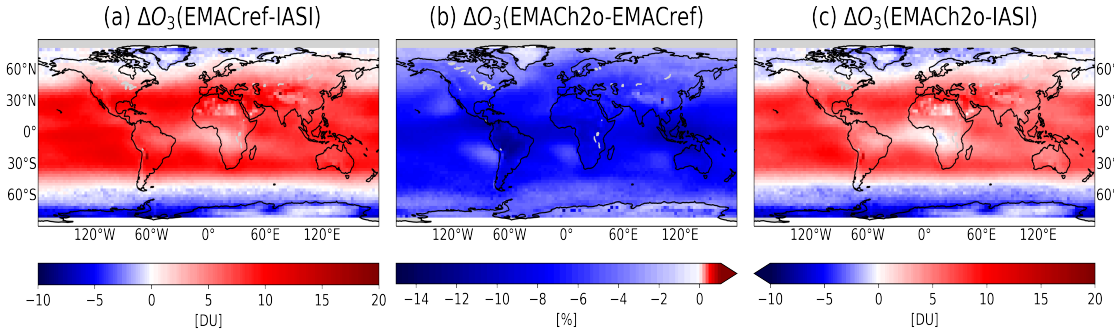

Figure 5.5: Annual mean lower tropospheric (up to 300 hPa) O_3 column (a) bias of EMACref towards IASI, (b) the change due to EMACh2o and the remaining discrepancy between IASI and EMACh2o.

the modified reactions was investigated in one sensitivity simulation. The inclusion of a water-dependent HNO_3-channel of the HO_2+NO reaction is identified as the dominant effect. In particular, humid conditions significantly enhance the yield. These findings are in line with Butkovskaya et al. (2009) who reported that the HNO_3-channel at 50 % humidity is as important as the HNO_3 production from the OH+NO_2 reaction. However, here, the HNO_3 yield might be overestimated in the Amazon due to the local deposition predicted by EMAC. HNO_3 is deposited efficiently to surfaces which is favoured by wetness (Nguyen et al., 2015). But for EMAC a dry bias occurs in the Amazon, resulting in too dry soil (Hagemann and Stacke, 2015) and under-represented dry deposition. The simulated weakening of the OH and NO_2 sink due to the newly added channel, which decreases tropospheric O_3, is consistent with other studies (Butkovskaya et al., 2009; Gottschaldt et al., 2013; Cariolle et al., 2008). A significant reduction of the O_3 bias due to this mechanism has been also reported by e.g. Righi et al. (2015).

The inclusion of the water dependence in the RO_2+NO reactions leads to an increased alkyl nitrate yield. Exemplary for two compounds, we calculated an enhancement by 77 %. The resulting values exceed, however, the estimates by Khan et al. (2015, Table 5) which likely reflects the speed-up of the RO_2+NO reactions by water here. Furthermore, the dry deposition fluxes in EMAC also increase significantly but they are at the lower end of model estimates (e.g., Archer-Nicholls et al., 2021, their Table 8). The general increase of alkyl nitrates agrees with the general findings of Xing et al. (2018) who also reports an enhanced yield as a consequence of RO_2-water complexation, however only for MACRO2. The supporting evidence for this effect in other RO_2+NO reactions has not yet been published.

The rate coefficient used here to enable the formation of water-radical complexes in the OH+NO_2 reaction lies in between the recommendations of the two expert panels, IUPAC and JPL. Their recommended kinetic data significantly deviates from both recommendations under dry conditions in some parts of the atmosphere. This deviation leads to predictions of different partitioning of reactive nitrogen between NO_x and NO_y. In particular, in the cold UTLS, the discrepancy of the reported

rated coefficients is 50 % (Amedro et al., 2020). Nevertheless, significant impacts of the water-effect in the OH+NO_2 reaction on O_3 production are expected only for very polluted and humid air masses. The major uncertainty on this reaction concerns the formation and fate of HOONO. A better assessment of the atmospheric importance for NO_x and HO_x would need detailed experimental studies (Amedro et al., 2020). Overall, enabling the formation of water-radical complexes lowers the chemical O_x production by 20 % to 4451 Tg a^{-1}. This change dominates the 17 % decrease of the chemical loss terms to 4118 Tg a^{-1} (mainly due to O_3 decrease, see Table 5.1). The reduction of the chemical budget terms brings the model in better agreement with the recent estimates by the Tropospheric Ozone Assessment Report (TOAR), reporting 4500-5200 Tg a^{-1} chemical O_3 production and 4000-4800 Tg a^{-1} loss (Young et al., 2018). Considering also the changes of the additional O_x sources and sinks yields a net reduction of O_x. The remaining tropospheric O_3 burden of 347 Tg (-12 %, Table 5.1), simulated by EMACh2o, also agrees much better with the recent multi-model mean estimate of 340 Tg a^{-1}.

6 Global modelling of drought-stressed biogenic isoprene emissions

This chapter describes the inclusion of drought stress in the model for biogenic isoprene emissions. To assess the global impact of the drought stress on the isoprene emission flux we conduct the sensitivity simulation EMACisop, which applies the pre-calculated drought stress factor (Jiang et al., 2018) via namelist. The change of the global isoprene emission is compared to model and site measurements. The subsequent impacts on the isoprene abundance and the tropospheric composition are shown and discussed with the help of passive tracers for diagnostic of the computed global O_x budgets. Finally, the comparison with measurement data assesses the potential of this modification to improve the current tropospheric O_3 model bias.

6.1 Model implementation

Measurement studies found diverging responses of BVOC emissions to drought depending on the duration of the drought period. At the initial stage, plants reduce the water loss by decreasing the stomatal conductance, which leads to an increase in leaf temperature. Plant emissions are correlated positively to leaf temperature. Thus, the emissions increase if sufficient carbon resources are available despite the reduced uptake. After longer exposure to drought, emissions ultimately decrease in response to a soil moisture deficit (Pegoraro et al., 2004; Grote et al., 2009). However, the commonly used soil moisture (drought) stress factor, available in MEGAN2.1, cannot capture such severe drought events (e.g., Sindelarova et al., 2014). The algorithm describes a factor in the [0,1] range varying with actual soil moisture and the local wilting point (relative to an empirical constant parameter). However, the derived stress factor depends strongly on the choice of the wilting point. Thus, Huang et al. (2015) have shown a wide range in emission reductions going from minimal to -70 %, depending on the wilting point input data. These findings demonstrate that soil moisture represents a relevant uncertainty in the modelling of plant emissions (Huang et al., 2015; Jiang et al., 2018). Using the soil moisture factor results in an underestimation of isoprene emission at the start and the peak of the drought period compared to measurement data (Jiang et al., 2018). Due to these reasons, the standard configuration of EMAC neglects the MEGAN2.1 soil moisture factor.

In contrast, by applying a mechanistic drought stress activity factor Jiang et al.

(2018) achieved a good agreement between modelled and measured isoprene emissions under short- and long-term droughts. The stress factor acts on the photosynthetic enzyme activity ($V_{c,max}$), which decreases in response to dryness as stomata close. Drought stress is defined by the function β, which depends on soil water potential, the root distribution of PFTs and the wilting point. If β falls below 0.6, a threshold derived from field measurements, plants are considered to suffer from drought stress. When drought stress increases, the factor approaches 0. According to this, the soil moisture (drought) stress factor (γ_{SM} in Eq. 2.10, standard EMAC: =1) is calculated with the following algorithm (Jiang et al., 2018):

$$\gamma_{SM} = 1, \qquad (\beta > 0.6) \tag{6.1}$$

$$\gamma_{SM} = V_{c,max}/\alpha, \qquad (\beta < 0.6, \alpha = 37) \tag{6.2}$$

$$\gamma_{SM} = 0, \qquad (\beta < 0.6) \tag{6.3}$$

The empirical parameter α, however, relies only on measurements at one side and would need more evaluation (Jiang et al., 2018). The soil and plant scheme required for this approach is not available in such detail in EMAC. Therefore, we use the pre-calculated data set by Jiang et al. (2018) in CLM/MEGAN as monthly time-series covering 2005 to 2014[1]. Figure 6.1 reveals the global distribution of the pre-calculated factor for the year 2009. Several regions with high emissions, such as South East Asia and the Southern U.S., experience significant drought stress. The inner tropics are not affected during most of the year, which is likely due to the deep water reservoirs (Hagemann and Stacke, 2015, and references therein).

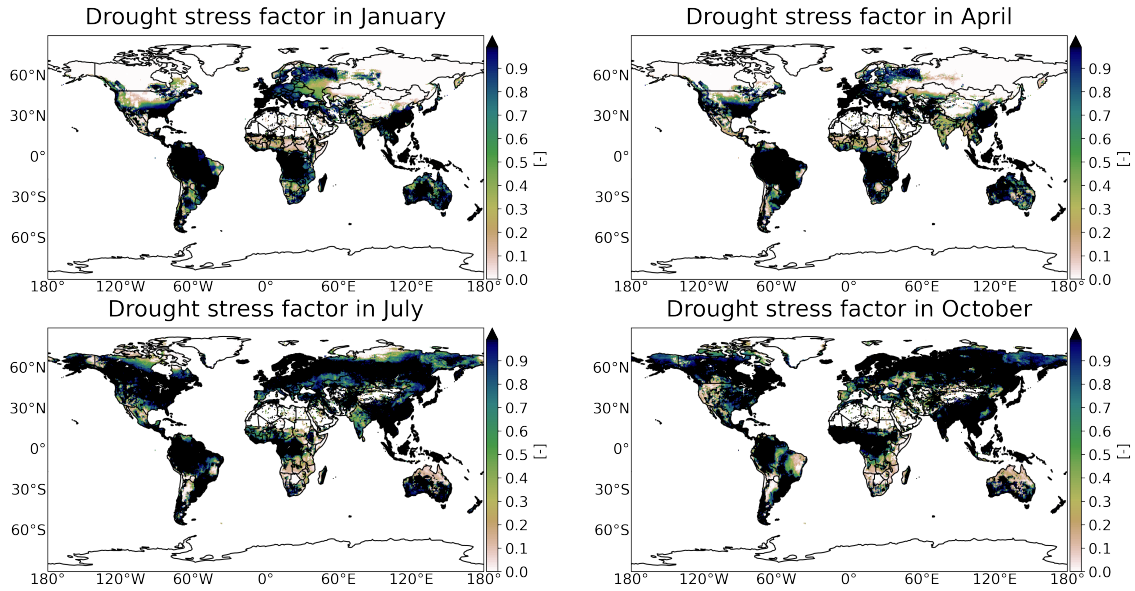

Figure 6.1: Applied drought stress (a) in January, (b) in April, (c) in July and (d) in October 2009.

[1]freely available at `https://drive.google.com/file/d/0B53BwxgQlv_3NWktNTF5MENBMk0/view?resourcekey=0-ejUxanIwTDo_RI3e3O-SUg`, last access: November 2021

6.2 Simulation results

Figure 6.2 shows the global distribution of the annual mean isoprene emission flux and the absolute difference comparing the reference and the sensitivity simulation. The isoprene emissions range from >100 mg $m^{-2}d^{-1}$ in the Eastern US, Central Africa and the Amazon to small values (≈1 mg $m^{-2}d^{-1}$) in the cold temperate forests (not visible here). These findings are generally in line with other studies employing MEGAN. In fact, estimated emission activity varies among different PFTs (Guenther et al., 2006, and references therein). The highest activity is estimated over evergreen broad-leaf tropical trees (Guenther et al., 2012) as shown here (Fig. 6.2a) over the Amazon and Central Africa. Among the main emission regions (US, East Asia, Amazon and Central/Southern Africa), the regional mean emission is highest in the Amazon (Fig. 6.3a) over the year, with a maximum in October. The seasonal variation on isoprene emissions depends on the local weather conditions, as also considered by MEGAN. The peaked emissions in the Amazon are associated with the local maximum in temperature and solar radiation.

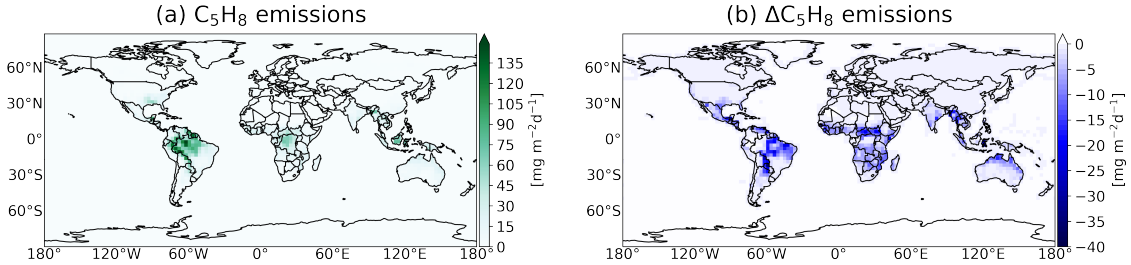

Figure 6.2: Annual mean (a) isoprene emission flux (EMACref) and (b) the absolute difference (EMACisop-EMACref) in 2009.

Observations by Wells et al. (2020), however, additionally show a maximum in April and a minimum in June/July associated with the leaf flushing between the wet and dry season. EMAC predicts much lower emissions over South Africa, which significantly underestimate the measurements due to the missing representation of biogenic emissions in the woodlands of Angola (Guenther et al., 2012). During the year, the modelled emissions vary only slightly. According to observations, emissions show a maximum in January and a minimum in July (Wells et al., 2020, and references therein). In the NH, the emissions (Southern US and East Asia) are generally lower than on the SH. Thereby, the maximum emissions occur in the U.S. due to the greening of the deciduous oak trees, which are associated with a high releases of VOCs (Guenther et al., 2012), also shown by measurements (Wells et al., 2020, and references therein).

[2]defined according to the IPCC climate reference regions (Iturbide et al., 2020). The following are used (region names with acronym and index in brackets): E Asia: (EAS/35); SE US: E.North-America (ENA/5), Amazon: N.W.South-America (NWS/9), N.South-America (NSA/10), N.E.South-America (NES/11), South-American-Monsoon (SAM / 12); S. Africa: S.Eastern-Africa (SEAF/24), W.Southern-Africa (WSAF/25), E.Southern-Africa (ESAF/26)

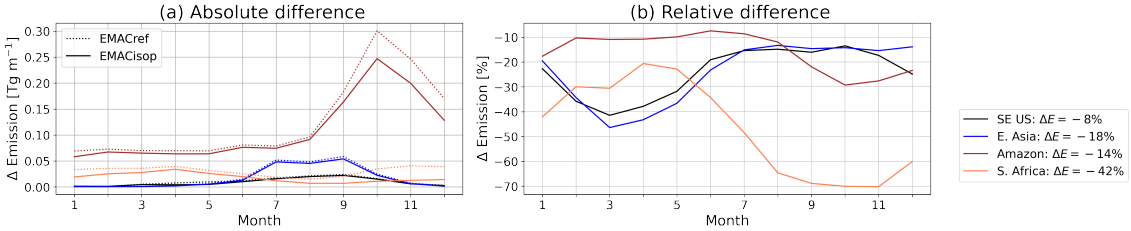

Figure 6.3: Annual cycle of the regional mean (a) isoprene emission flux (EMACref) and (b) the relative difference (EMACisop-EMACref) for different regions[2].

Applying the drought stress factor to EMAC leads to decreased annual mean isoprene emissions in the southern part of the U.S., Asia, Central Africa and South America. Among the regional means, all emissions decrease during the year (Fig. 6.2b). The absolute change is highest in the Amazon, where the emissions drop significantly at the onset of the dry season in October (Fig. 6.3a). This change accounts for a 20 % reduction (corresponding to $\Delta\gamma_{SM}$ =-0.2) relative to the prevailing drought stress during the year. The same seasonality of drought stress applies to the South African (regional mean) emissions. This region covers dryer areas such as savannas, and thus the drought stress is stronger during the year than in the Amazon (Fig. 6.3b). This yields 42 % emission reduction per year, the highest change among the emission regions. Also, the northern emission regions experience drought stress between 20 and 45 % during the year. The maximum reduction occurs in March due to the low fraction of wet-covered surfaces. Globally, the drought stress decreases the isoprene emissions by 22 %, which is close to the emission change reported by Jiang et al. (2018).

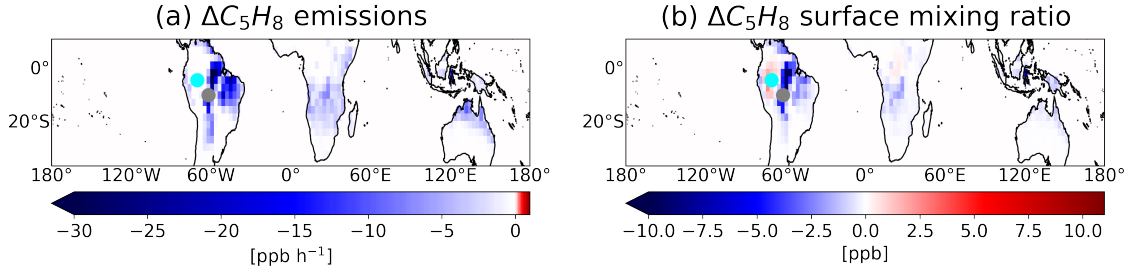

Figure 6.4: Mean absolute difference (EMACisop-EMACref) of (a) the isoprene emission flux and (b) the surface mixing ratio of isoprene during October, 1-5.

The impact of the emission reduction on the tropospheric chemistry is explored exemplary at two locations in South America (see dots in Fig. 6.4) for October 2009. At the location in South Brazil (gray dot), the ratio of isoprene background levels (≈10 ppb) and NO_x mixing ratios is a lot smaller than in other South American regions (Fig. 6.5). The net O_x ($\frac{dO_x}{dt}$) change is not correlated significantly to NO, which indicates that also VOCs have an influence on the O_x chemistry. In response to the inclusion of the drought dependence the isoprene emission flux decreases

at all days by 10-80 ppb h^{-1} which yield a reduction of the surface mixing ratio by more than a factor of 2 (-4- -8 ppb). Consequently, less VOC photolysis and oxidation occurs. The reduced photolysis leads to a noticeable reduction of the HO_2 production (≈ -0.04 ppb h^{-1}, 20 %) but is lower than the changed loss of HO_2 by reaction with O_3 (net $L(O_x)$, Fig. 6.6). Also, the reduced oxidation leading to fewer radicals and thus up to 2.8 pph h^{-1} less net O_x production (see Sect. 2.2) is minor (≈ 4 %) relative to the absolute reaction rate of 5-80 ppb h^{-1}.

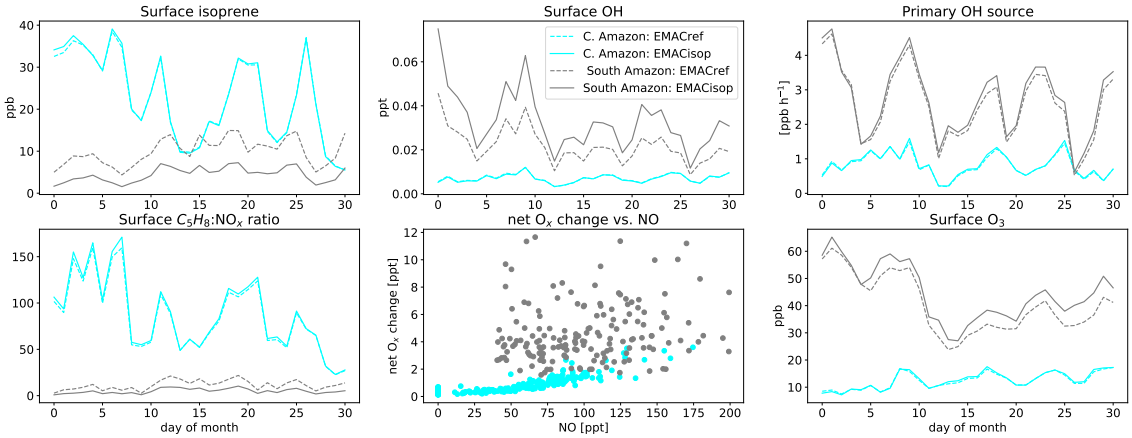

Figure 6.5: Chemical trace gas levels at the two sites in South America: central Amazon (grey colour) and south Amazon (cyan colour).

The VOC ozonolysis occurs to be a relevant O_3 sink at this site, with higher reaction rates than the O_3 destruction by OH and HO_2 during the entire month (Fig. 6.6a). According to the reduced isoprene abundance, the reaction rate is almost halved (-0.2- -5.5 pph h^{-1}), which dominates the change of the O_x production and other loss terms easily. Thus, the O_3 increase by up to 8 ppb (5 %) is associated with this change, as also reported by Jiang et al. (2018, and references therein). In response to the O_3 enhancement, the primary OH production increases (up to 20 %). As OH accounts for its main oxidation, this leads to a further isoprene decrease.

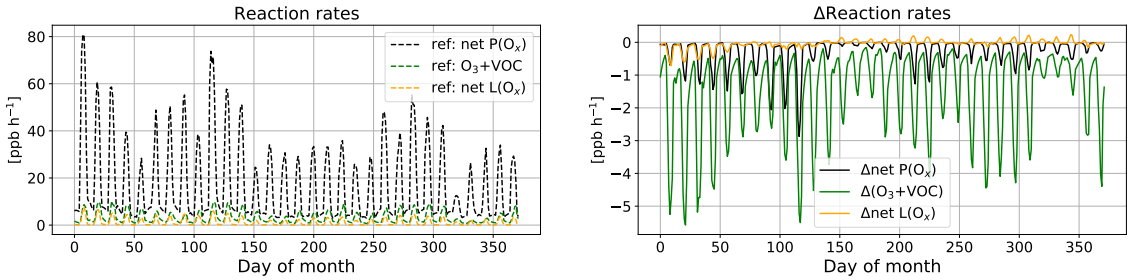

Figure 6.6: Monthly 2-hourly time-series of the (a) O_x production and loss terms and the VOC ozonolysis reaction rate (EMACref) and (b) the respective absolute difference (EMACisop-EMACref) at the southern Amazon site (gray dot in Fig. 6.4) in October 2009.

Contrarily, the central tropical rainforests show a slight increase in isoprene. Al-

though the local emissions are not significantly stressed, the trace gas levels change, likely affected by the altered composition in the near surroundings. So, the central Amazon (cyan coloured dot) experiences a transition in prevailing wind direction at the onset of the dry season, where the monthly mean wind shifts from North-West to South-East (Fig. 6.7). This regional phenomenon is related to a change of atmospheric heating driven by the evapotranspiration from the forest (Li and Fu, 2004).

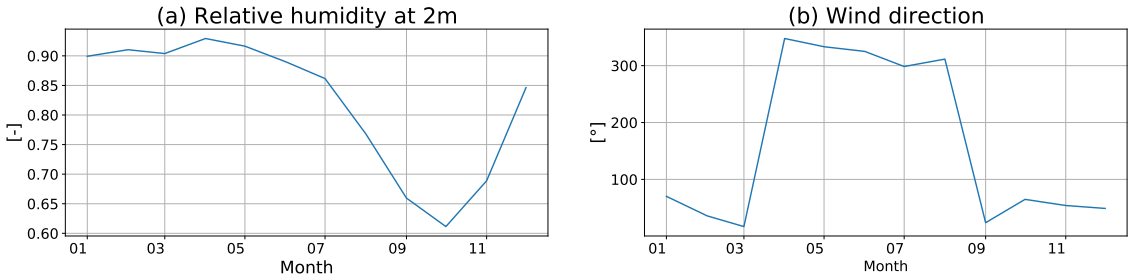

Figure 6.7: Annual cycle of monthly mean (a) relative humidity and (b) wind direction at 4.2 °S, 71.3°W (cyan dot).

Thus, the local ground-level air composition in the Central Amazon is likely affected by south-easterly transport ($\approx 65°$ in October) from the site at which the isoprene emissions decrease (e.g. location marked by the gray dot). Here, due to the high isoprene emissions, the ratio to NO_x levels (100-150 ppt) is two orders of magnitude higher than at the southern location. Thus, net O_x rises with increasing NO levels (NO_x-limited, see Sect. 2.2). The transport of fewer OVOCs, which are formed during isoprene oxidation, leads to a lower local radical production. This decreases the main O_x producing reactions, which occurs to be far higher than the decrease in net $L(O_x)$ ($L(O_x)$: OH/HO_2+O_3, Fig. 6.8b). This way up to 10 % less net O_x occurs. The reduced HO_2+NO reaction lowers the local OH production, which dominates the OH yield of $O(^1D)$. The initial OH decrease lowers the O_3 depletion (by reaction with OH and HO_2) which results in a rise of the O_3 mixing ratio. These reactions rates are, however, more than one order of magnitude slower than the OH production rate. The enhanced O_3 levels (and thus the photolysis product: $O(^1D)$) provide an enhanced OH source by +10 %, which starts to exceed the OH formation by Reaction 2.14. Lower OH levels lead to less isoprene oxidation (Reaction 2.16), which explains the increase of the surface isoprene mixing ratio at the beginning of October. Throughout the month, isoprene and OH levels counter-balance each other. Although the VOC ozonolysis has high reaction rates at this VOC-rich site (compared to the southern side), it is only slightly changed.

Figure 6.9b reveals the annual change of OH, which depends on the isoprene emission change and the local chemical regime. Since isoprene mainly reacts with OH (Taraborrelli et al., 2009), the isoprene decrease results in enhanced OH surface mixing ratios. Small changes in the NH occur consistent with small reductions in isoprene emissions. The high descent of the isoprene levels over the SH continents leads to an increase of the OH surface mixing ratio by more than 40 %. Also, the

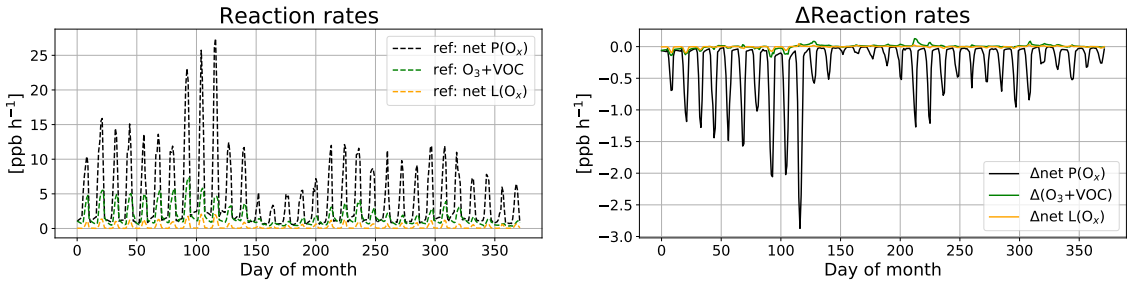

Figure 6.8: Monthly 2-hourly time-series of the (a) O_x production and loss terms and the VOC ozonolysis reaction rate (b) and the respective absolute difference at the northern side (cyan dot in Fig. 6.4) in October 2009.

decrease of isoprene due to the stressed emissions strengthens the OH reaction with NO_2 (against the VOC oxidation), and by this an important OH sink under high NO_x conditions (Lelieveld et al., 2016). The increase is pronounced in the SH, which dominates the enhancement of the HO_2+NO reaction rate. Thus, the stronger radical termination rate (NO_x removal) and consequently weaker net O_3 production (see Sect. 2.2) causes lower O_3 surface levels by up to -10 % compared to the reference simulation (Fig. 6.9c). The O_3 increase in South America reflects the decrease of the VOC ozonolysis resulting in enhanced O_3. In Europe and North America, the low isoprene changes do not affect the O_3 driving reactions (OH+NO_2, HO_2+NO) much, resulting only in a small decrease of O_3 at the surface. The corresponding reduction of 3-5 ppb is in agreement with Jiang et al. (2018). When the chemical regime is O_3-depleting, such as in the Amazon and Congo basin, the O_3 decrease follows from the increase of OH, which is a relevant O_3 sink and vice versa.

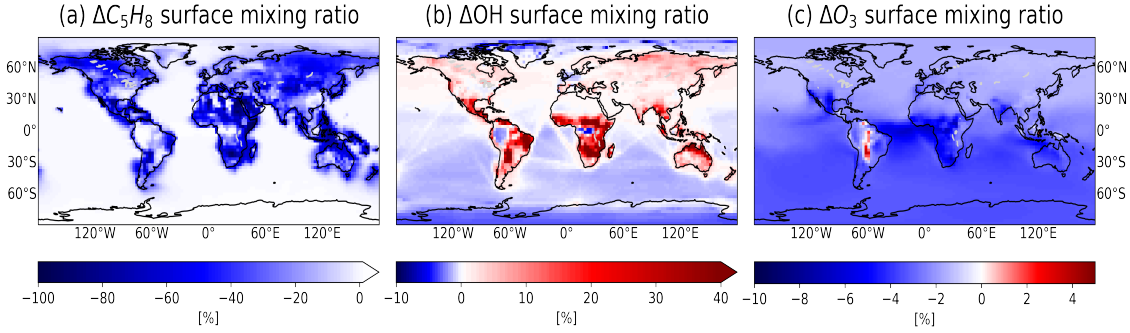

Figure 6.9: Annual mean relative difference (EMACisop-EMACref) of (a) the isoprene, (b) OH and (c) O_3 mixing ratio at the surface.

Globally, the decrease of the radical sources dominates the influence on O_x production. In fact, the rate of the RO_2+NO reactions is reduced by 16 % in the PBL. This drives the lower O_x and O_3 production, which exceeds the decrease of loss by O_3 reacting with HO_2 (-6 %) globally. Overall, this results in a decrease of net O_x levels. However, the decrease is small relative to the model-measurement bias. The discrepancy towards the ground-based observations from the TOAR database is not significantly changed (<2 ppb) for most regions on the NH. Nevertheless, the mean

O_3 bias declines by 9 %.

The reduction of O_3 in the troposphere is within 3-5 % (Fig. 6.10b) of a similar magnitude as at the surface. The changes dominate in the SH, where the modification of the isoprene emission reveals the highest reduction. The reduced isoprene levels correspond to a slight decrease (1-2 DU) of the seasonal mean EMAC-IASI mismatch. The global bias is not affected significantly. The lowered oxidation of isoprene and products (HCHO, MVK etc.) reduces the atmospheric sinks of OH. Subsequently, the OH mixing ratio in the major parts of the troposphere increases compared to EMACref. The increase of up to 6 % is strongest in the lowest layers of the SH (0- -50°) and decreases towards the troposphere (Fig. 6.10a). The slight OH decrease south of 40° reflects mainly the response to the O_3 reduction over the ocean.

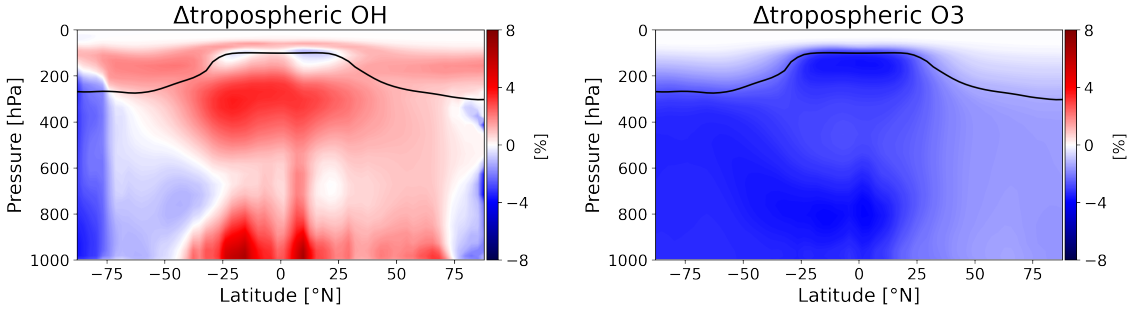

Figure 6.10: Zonal mean relative difference of tropospheric (a) OH and (b) O_3. The annual mean tropopause is depicted by a black line.

6.3 Discussion

Applying the drought stress factor by Jiang et al. (2018) accounts for the isoprene reduction in moderate and severe drought well in comparison with site measurements. The formulation avoids the uncertainty associated with the wilting point input data required for the current MEGAN v2.1 soil moisture dependency. However, observations report rising isoprene emissions during the initial drought state (e.g., Ferracci et al., 2020). The drought stress factor used in this study depends on the plant water status and the carbon fixation during photosynthesis and may, thus, not account for this emission increase. Including the response to the soil water status in models is generally important for the accurate representation of BVOC emissions (Paton-Walsh et al., 2022, and references therein). However, the drought stress factor applied here stems from a pre-calculated data set because EMAC still lacks a fully coupled dynamic vegetation model and thus, does not account for the soil and plant information required for the algorithm. The Land component of the Community Earth System Model (CLM4.5/CESM1.2), which was used to generate the data set (Jiang et al., 2018), however, differ from EMAC regarding meteorological model nature.

In general, the global distribution of isoprene emissions estimated by models is in line with space-observations (Weng et al., 2020; Sindelarova et al., 2014). Model estimates are, however, highly uncertain and differ significantly depending on the driving meteorology, land cover data and the algorithm (Cao et al., 2021; Weng et al., 2020). Present-day estimates ranges from 330 to 415 Tg(C) a^{-1} for similar model resolutions. Table 6.1 provides an overview. Most models apply the MEGAN algorithm to estimate biogenic emissions. The usage of interactive land cover schemes may reduce the uncertainty associated with prescribed land cover and vegetation data. Considering the soil moisture/drought dependency yields in general lower estimates (Sindelarova et al., 2014; Weng et al., 2020) which are in line with the global isoprene emissions predicted in this study. However, not all current models include the soil moisture/drought response of isoprene emissions due to the high uncertainty of currently available formulations such as the MEGAN v2.1 soil moisture stress factor and incomplete knowledge of the underlying physiological functioning (e.g., Emmons et al., 2010). In comparison with an OMI-based constraint, all model estimates seem to be over-predicting the global isoprene emissions (Bauwens et al., 2016). In fact, Bauwens et al. (2016) have estimated a global isoprene emission of 272 Tg(C) a^{-1} from OMI HCHO retrievals for 2005-2013. A recent study based on six CMIP6 models reports a low agreement between the models and measurements where models overestimate emissions over the evergreen-broadleaf forest and underestimate the emissions over grassland, deciduous-broadleaf forest and evergreen-need leaf forest by 40-50 %, respectively. A possible reason might be that bottom-up approaches like MEGAN miss the emission peak in Southern Africa (Wells et al., 2020). Also, Wells et al. (2020) found an overestimation of the observed isoprene column over the Amazon, which they attribute to under-predicted NO_x emissions leading to biased OH levels.

Table 6.1: Overview of present-day (2000-2017) isoprene emission estimates.

Data source	Drought/SM stress	Resolution [°]	Estimate [Tg(C) a^{-1}]
MEGAN v2 (Emmons et al., 2010)	no	2.8x2.8	414
LPJ-GUESS (Young et al., 2009)	no	2.5x3.75	401
CMIP6 models (Cao et al., 2021)	50 % SM	0.9-2.8	400
MEGAN v2.1, JSBACH (Henrot et al., 2017)	SM	1.8x1.8	351
This study, MEGAN v2.1	**Drought**	**2.8x2.8**	**347**
MEGANv2.1 (Weng et al., 2020)	SM	2.0x2.5	333
satellite-based (Bauwens et al., 2016)		0.5x0.5	272

7 Summary, discussion and outlook

Conclusion

Representing the chemical composition of the troposphere in models is a crucial task in climate research just as for air quality assessment. This research requires not only knowledge of the chemical processes, trace gas sources and sinks. Considering the interaction of tropospheric composition with meteorology is important. This aspect becomes more and more relevant as along with the general warming of the climate the frequencies of meteorological extremes are expected to increase.

This study aims to add the necessary meteorological dependencies to diverse process representations in EMAC to increase the realism of modelled weather-pollution interactions. This investigation also provides potential recommendations for other Earth system models. The impact of additional meteorological features for the trace gas dry deposition, radical chemistry and biogenic VOC emissions is investigated in this study at the local and global scale. Although some uncertainties remain, the analysis reveals significant improvement potential for global Earth system modelling.

First, the model representation of trace gas dry deposition to terrestrial vegetation is extended with dependencies on meteorology (Chapter 3) which have been shown to drive its site-specific variation significantly. Since the process plays a key role for tropospheric O_3 this trace gas is in the focus of the first study. The default dry deposition parametrisation of stomatal uptake only relies on solar radiation. To consider its response to meteorology properly, the scheme is extended by multiplicative sensitivity factors for temperature and atmospheric water deficit. Although the formulation is empirically derived from site measurements, it depends only on a few parameters. This approach ensures simplicity and adaptability, which is of concern, especially for global models. The extension yields a spatially different response depending on the local climate. Namely, in moderate and humid climates O_3 uptake is increased, while during dryness and elevated temperature the plants increasingly respond by closing their stomata. In addition, the extended scheme firstly contains an explicit representation of cuticular dry deposition depending on vegetation foliage density, relative humidity and surface roughness. This pathway has been proposed as a relevant contributor to e.g. O_3 uptake. Compared to the old scheme, which only relies on a high constant resistance, the explicit formulation of the cuticular pathway leads to a widespread increase of dry deposition. The increase is favoured in humid and densely vegetated areas. The evaluation against measurements of dry deposition velocity at four ground stations underlines the importance of both developments. The increase of the dry deposition yields an improved agreement

throughout the year. The analysis also demonstrates the considerable contribution of the cuticle over night, when stomatal uptake is small. Also, the implementation of the stomatal stress factors leads to a notable improvement of O_3 dry deposition towards measurements on a daily timescale. The assessment of the model performance in the Amazon forest has crucial importance since a high fraction of the global dry deposition is attributed to this densely vegetated region. Also, in this region, the revised scheme yields an increase in modelled dry deposition. However, the amplitude is significantly under-predicted by EMAC, like also by other models. The original parametrisation by which the stomata respond to soil moisture leads to stomatal closure. The water storage in the soil of the tropical forests does not hold enough water in the model. The modified soil moisture stress function, however, allows stomatal deposition with only reductions instead of shutting down (no wilting point). But the 'artificial' dryness in this model region cause a too high temperature and VPD stress and leads to an underestimation of cuticular deposition. This phenomenon explains the under-predicted dry deposition velocity compared to the measured value. Overall, the comparison with measurements demonstrates the crucial role of representing the meteorology accurately and the related uncertainty for dry deposition modelling. Globally, the extended dry deposition scheme leads to an increased annual dry deposition flux by 6 %. In separate regions, the impact is significantly higher, causing a reduction of surface O_3 by up to 25%.

The impact of this extended dry deposition scheme is assessed further with a global simulation capable of accurately representing the tropospheric O_3 chemistry and related processes. The model set-up additionally includes the representation of more VOCs emitted from plants and more complex chemistry (Chapter 4). A better representation of OVOCs allows for investigating the changed dry deposition, which is an important sink, especially for soluble compounds. In-soluble OVOCs, which generally have a lower uptake velocity (compared to soluble OVOCs), are affected more by the changes of stomatal dry deposition. Soluble compounds are shown to be deposited more efficient in the revised scheme, whereas the impact is higher than for O_3. That's because soluble compounds interact efficiently with wet interfaces. Globally, the dry deposition of soluble OVOCs is increased by 10-25 %. The reduced OVOC levels decrease the source of HO_2 radicals from photo-induced reaction cascades, which lower the O_x production. Thus, surface O_3 mixing ratios are reduced with the largest changes occurring in the NH during the vegetation seasons. The comparison of surface O_3 simulated by EMAC with TOAR measurements, considering day and night separately, demonstrates the improvement potential of including the cuticular pathway. The extended scheme increases O_3 dry deposition fluxes during the night to a higher degree than during the day. The total annual model bias of surface O_3 is reduced by 13 %.

Next, the role of water vapour in reactions of HO_x and RO_x radicals with NO_x is considered because it has been found to significantly affect the trace gas budget of HO_x and O_3 (Chapte 5). For this, modified kinetics based on the most recent findings are used. While the modifications of the HO_x+NO_x reactions are well evidenced, the inclusion of the water effect for the RO_2+NO reaction is speculative.

In addition, the well known HNO_3-channel from the HO_2+NO reaction is included according to the most recent kinetic data, which also considers the important dependence on water. This modification reveals to be dominant among the modifications of the radical kinetics. Due to the competition with the original solely channel, this weakens the chemical O_x production through the HO_2+NO reaction and thus decreases the NO_2 surface levels in the respective regions. The results confirm that the humidity amplifies the HNO_3 formation, leading to 40 % enhanced HNO_3 mixing ratio at the surface. Although the reaction is fastest in cold regions as the Canadian boreal forest, the maximal relative increase occurs in the Amazon due to the high water vapour levels. The globally mainly reduced NO_2 and OH levels also affect the further O_x production terms decreasing it overall by 20-30 %. The water inclusion in the RO_2+NO reaction leads to an enhanced tropospheric burden and dry deposition of alkyl nitrates and decreases the O_x formation. The expected speed-up of the OH+NO_2 is likely only contributing to the trace gas budget changes in the tropics, where it is a significant net OH sink. Overall, enabling the formation of water-radical complexes decreases the chemical O_x terms, leading to a better agreement with recent estimates (models and measurements). The modification lowers the global tropospheric O_3 burden by 12 %, which improves the comparison with O_3 measurements at the surface and in the lower troposphere. The remaining discrepancy towards TOAR data is with ± 4 ppb minor. Also, the lower tropospheric O_3 column is significantly reduced by 30 % down towards a global bias of 4.2 DU.

Apart from radicals also VOCs, whose highest amounts are emitted from the biosphere, importantly determine the tropospheric composition, in particular O_3 chemistry. The inclusion of the sensitivity to drought/soil moisture is considered desirable in this study. The applied offline approach, however, is based on pre-calculated data, which relies on other model dynamics. The modification reduces the annual global emission of isoprene by 22 %, most pronounced in the Amazon (Chapter 6), which brings the EMAC emission estimate in better agreement with other models and measurements. The emission decrease weakens the OH oxidation and gives rise to the O_3 termination reaction, reducing the O_3 abundance by up to 20 % in regions with low VOC levels compared to NO_x. In the Central Amazon, where no drought stress happens, and thus the local emissions remain unchanged, the trace gas budgets are affected by the changes in the surroundings. Namely, fewer OVOCs are advected, weakening the local radical propagation. This change initiates several effects, which decrease the monthly mean OH levels. In the prevailing NO_x-limited chemistry, OH is a net sink for O_3, thus the O_3 levels are enhanced. The reduced VOC abundance weakens the OH recycling, corresponding to higher OH levels in the entire troposphere. Globally, the O_3 discrepancy towards TOAR data is decreased by 9 % per year due to the modification. On the SH, the changes also influence the seasonal mean tropospheric column. Overall, the reduction of the isoprene emissions reduces the annual EMAC bias towards IASI by 1-2 DU.

Discussion

The model prediction of the tropospheric O_3 levels, which is a key for the entire chemical composition of the troposphere, also relies on the release of NO_x from natural and human activities. The soil NO_x emissions which account for 25 % of global NO_x are generally underestimated in EMAC through the current usage of the Yienger&Levy scheme (Steinkamp et al., 2009). The pulsing parametrisation, which describes a large NO_x release if very dry soil becomes wet and the rapid decay afterwards, reasons the underestimation at all land-cover types (except in the tundra and rainforest). This effect could explain the remaining mismatch of surface O_3 when comparing model and measurements in Europe and USA, most important in boreal summer and autumn. A relevant contribution of the destruction by surface-emitted NO to the O_3 loss during the day has been shown by e.g. Fares et al. (2012). In the NH, the positive O_3 bias is additionally attributed to the coarse model resolution, which cannot resolve hot spots with enhanced NO_z (NO_y - NO_x) production in polluted regions. The nesting of higher-resolved models for the European, North American and Asian domain decreases the model bias of surface O_3 by 3-5 ppb. The annual mean model-measurement discrepancy of the whole troposphere is reduced thus by about 10 % globally (Yan et al., 2016). The discrepancy for O_3 between models and measurements over South Africa is explained likely by undetected small fires (>100 hectare) by satellite products based on the MODIS instrument (Ramo et al., 2021), which is also one source of data for the GFAS inventory (Andela et al., 2013). Furthermore, NO_2 is likely underestimated in this region because peat fires emit low amounts of NO_x. Bottom-up approaches, such as GFAS hardly capture a high abundance of VOCs (Krol et al., 2013). The positive model bias over the tropical Pacific is attributed to the lightning NO_x scheme used here since the standard parametrisation in EMAC does not distinguish between land and ocean when estimating the flash frequency. Thus, this scheme overpredicts the lightning activity over oceans (Tost et al., 2007). The distinction is represented by the Price&Rind scheme commonly applied in e.g. the CMIP6 simulations (Griffiths et al., 2021). Also, the under-represented O_3 loss by halogens (Sherwen et al., 2016) contributes to the overestimation of tropospheric O_3 over the ocean. The inclusion of tropospheric iodine, which catalytically destroys O_3, leads to about 20 % reduction of surface and 10 % of tropospheric O_3. In general, the model evaluation requires measurement data to evaluate the model performance, as demonstrated in this thesis. Especially, ground-based observations are also needed for the evaluation of satellite products. However, observation sites in the SH are generally sparse and often only located in urban areas (Paton-Walsh et al., 2022).

Outlook

In this work, the proposed model developments enabling a higher model sensitivity to meteorology were analysed and finally evaluated against O_3 measurements in the scope of a general improvement. However, extreme meteorological events, such as

heat waves, will increase in frequency and intensity (Ridder et al., 2022). Heat waves are mostly attributed to synoptic-scale high-pressure systems, often so-called blocking situations when the pressure system persists at almost one location over a long period. Thereby, soil dryness typically amplifies the high air temperatures. Meteorological extremes are known to be linked to the occurrence of elevated air pollution events. For example, Hou and Wu (2016) found that severe O_3 pollution are seven times more probable during summer when heat waves occur. Air stagnation resulting from a high-pressure blocking system leads to an accumulation of the precursors in the PBL, which amplifies the local O_3 formation. Also, a considerable fraction of high O_3 levels in heat wave conditions is attributed to a decrease of dry deposition in response to soil dryness, high temperature, and atmospheric water deficits (e.g., Andersson and Engardt, 2010). Since these relations leading to high O_3 exposure which can cause severe health issues are of public concern, the creation of an openly available web interface of this is an ongoing project. The interface visualises the occurrence of high O_3 concentration dependent on metrics for meteorological extremes (heat waves and air stagnation) and reveals where the O_3 levels exceed the healthy limit.

Also, an investigation of these interactions during the summer heat wave 2010 in Eastern Europe is ongoing. During this mega heat wave, 50 % of the measured values in Europe exceeded the 500-year temperature record (Barriopedro et al., 2011). Additionally to the stomatal parametrisation with meteorological responses, EMAC was recently equipped with a photosynthesis scheme (A-g_s model) used in the IFS model and developed at ECMWF (2015). In the A-g_s model, the stomatal behaviour is coupled to the CO_2 assimilation in plants, affecting also the transpiration and thus moisture cycling. Applying these two stomatal schemes, the simulated O_3 extremes in the 2010 summer heat-wave will be assessed against ground-based measurements of maximum O_3. The plant photosynthesis, calculated by the A-g_s model, provides additionally the possibility to implement the online calculation of the BVOC emission reduction by soil moisture stress (according to Jiang et al. (2018)). However, also O_3 and plants interact in the opposite direction since high O_3 exposure damage the plant physiology, which impacts the crop yield, the carbon and the water cycle. This impact will be considered in EMAC by incorporating a recent parametrisation by Sadiq et al. (2017). To examine the drivers, chemical and physical, of air pollution extremes during heat waves and drought in the light of climate warming descriptive storylines of past extreme events will be developed (Shepherd et al., 2018). Separating the dynamical (large scale circulation patterns, high uncertainty) from the thermodynamic effects via spectral nudging only wind and vorticity allows reproducing the dynamical conditions of the extreme event while thermodynamic aspects can be studied. This approach aims to make climate change and its impact more tangible.

For the accurate representation of tropospheric O_3 in models reducing the current model discrepancy towards measurements, additional processes are potentially relevant. Accounting for the explicit representation of in-cloud organic chemistry could reduce this model bias, as it has been shown by using the Jülich Aqueous-phase

Mechanism of Organic Chemistry (JAMOC; Rosanka et al., 2021a). This is also important for estimating the impact of intense peat fires on tropospheric O_3 (Rosanka et al., 2020).

Furthermore, the soil emissions of nitrous acid (HONO) by bacterial nitrification, which is similar to NO emitted by soils, have been found to account for the current underestimations of the tropospheric levels in models. HONO is a relevant daytime source of OH. Adding this process to the model representation affects the HO_x and O_3 budget in the troposphere importantly (Su et al., 2011; Yang et al., 2020). The first global model assessment of this process based on model estimates of NO soil emissions and measurements at multiple field samples is in preparation. The upcoming implementation of a more mechanistic NO soil emission scheme will also ensure an improved dependence on soil moisture, pulsing and temperature in this process (Hudman et al., 2012).

Geosci. Model Dev., 14, 495–519, 2021
https://doi.org/10.5194/gmd-14-495-2021

Geoscientific Model Development
Open Access
EGU

A revised dry deposition scheme for land–atmosphere exchange of trace gases in ECHAM/MESSy v2.54

Tamara Emmerichs[1], Astrid Kerkweg[1], Huug Ouwersloot[2], Silvano Fares[3], Ivan Mammarella[4], and Domenico Taraborrelli[1]

[1]Institute of Energy and Climate Research 8, Troposphere, Forschungszentrum Jülich, Jülich, Germany
[2]Max Planck Institute for Chemistry, Mainz, Germany
[3]National Research Council, Institute of Bioeconomy, Rome, Italy
[4]Institute for Atmospheric and Earth System Research/Physics, Faculty of Science, University of Helsinki, Helsinki, Finland

Correspondence: Domenico Taraborrelli (d.taraborrelli@fz-juelich.de)

Received: 14 May 2020 – Discussion started: 17 June 2020
Revised: 20 November 2020 – Accepted: 6 December 2020 – Published: 26 January 2021

Abstract. Dry deposition to vegetation is a major sink of ground-level ozone and is responsible for about 20 % of the total tropospheric ozone loss. Its parameterization in atmospheric chemistry models represents a significant source of uncertainty for the global tropospheric ozone budget and might account for the mismatch with observations. The model used in this study, the Modular Earth Submodel System version 2 (MESSy2) linked to the fifth-generation European Centre Hamburg general circulation model (ECHAM5) as an atmospheric circulation model (EMAC), is no exception. Like many global models, EMAC employs a "resistance in series" scheme with the major surface deposition via plant stomata which is hardly sensitive to meteorology, depending only on solar radiation. Unlike many global models, however, EMAC uses a simplified high resistance for non-stomatal deposition which makes this pathway negligible in the model. However, several studies have shown this process to be comparable in magnitude to the stomatal uptake, especially during the night over moist surfaces. Hence, we present here a revised dry deposition in EMAC including meteorological adjustment factors for stomatal closure and an explicit cuticular pathway. These modifications for the three stomatal stress functions have been included in the newly developed MESSy VERTEX submodel, i.e. a process model describing the vertical exchange in the atmospheric boundary layer, which will be evaluated for the first time here. The scheme is limited by a small number of different surface types and generalized parameters. The MESSy submodel describing the dry deposition of trace gases and aerosols (DDEP) has been revised accordingly. The comparison of the simulation results with measurement data at four sites shows that the new scheme enables a more realistic representation of dry deposition. However, the representation is strongly limited by the local meteorology. In total, the changes increase the dry deposition velocity of ozone up to a factor of 2 globally, whereby the highest impact arises from the inclusion of cuticular uptake, especially over moist surfaces. This corresponds to a 6 % increase of global annual dry deposition loss of ozone resulting globally in a slight decrease of ground-level ozone but a regional decrease of up to 25 %. The change of ozone dry deposition is also reasoned by the altered loss of ozone precursors. Thus, the revision of the process parameterization as documented here has, among others, the potential to significantly reduce the overestimation of tropospheric ozone in global models.

1 Introduction

Ground-level ozone is a secondary air pollutant which is harmful for humans and ecosystems. Besides chemical destruction, a large fraction of it is removed by dry deposition which accounts for about 20 % of the total O_3 loss (Young et al., 2018). The process description of dry deposition considers boundary-layer meteorology (e.g. turbulence), chemical properties of the trace gases and surface types. In most global models, dry deposition of trace gases is parameterized using the "resistance in series" analogy by We-

sely (1989). The largest deposition rates of ozone occur over dense vegetation (Hardacre et al., 2015) where it mainly follows two pathways: through leaf openings (stomata) and to leaf waxes (cuticle) (Fares et al., 2012). Thereby, stomatal uptake is commonly parameterized following the empirical multiplicative approach by Jarvis (1976) which uses a predefined minimum resistance and multiple environmental response factors like in Zhang et al. (2003), Simpson et al. (2012) and Emberson et al. (2000). More advanced formulations often used by land surface models (Ran et al., 2017; Val Martin et al., 2014) are based on the CO_2 assimilation by plants during photosynthesis (Ball et al., 1987; Collatz et al., 1992). Both approaches rely on the choice and constraints of ecosystem-dependent parameters and have different advantages (Lu, 2018). A further role in coupling stomata to ecosystems is played by stomatal optimization models, whereas optimal stomatal activity with a maximum amount of carbon gain and a minimum loss of water is calculated based on ecophysiological processes (e.g. Cowan and Farquhar, 1977). Of particular interest are stomatal optimization models which, based on ecophysiological processes, maximize carbon gain while minimizing water loss. According to Wang et al. (2020), these models are promising in representing stomatal behaviour and improving carbon cycle modelling. Non-stomatal deposition has been less investigated by now; therefore, most models use predefined constant resistances or scale it with leaf area index (e.g. Val Martin et al., 2014; Simpson et al., 2012), while some apply an explicit parameterization based on the observational findings of enhance cuticular uptake under leaf surface wetness (Altimir et al., 2006).

The different parameterizations of the (surface) resistances cause main model uncertainties in computing dry deposition fluxes of trace gases, which depend on the response to hydroclimate and land-type-specific properties (Hardacre et al., 2015; Wu et al., 2018; Wesely and Hicks, 2000). Thereby, it has been shown that the original Wesely-based parameterization generally captures well the seasonal and diurnal cycles of dry deposition velocity, whereas model–observation discrepancy at seasonal scales arises from biased land type and leaf area index input data (Silva and Heald, 2018). Wong et al. (2019) stated that discrepancies of up to 8 ppb in ground-level ozone arise from different parameterizations.

The current dry deposition scheme of EMAC uses six surface types, where the parameterized processes represent the forest canopy as a whole (big-leaf approach). Thereby, the uptake over vegetation relies on stomatal deposition as the only pathway determined by the photosynthetically active radiation (Kerkweg et al., 2006). According to Fares et al. (2012) and Rannik et al. (2012), the stomatal uptake in parameterizations often lacks the dependence on meteorological and environmental variables (leaf area index, temperature, vapour pressure deficit). Moreover, several studies (e.g. Hogg et al., 2007; Fares et al., 2012; Clifton et al., 2017) found the contribution of an additional process to dry deposition at the leaf covering of plants. Zhang et al. (2002) firstly derived a parameterization from field studies which establishes the important link of this process to meteorology. In general, findings by Solberg et al. (2008), Andersson and Engardt (2010) and Wong et al. (2019) highlight the importance of considering the dry deposition–meteorology dependence in global models. Such an extension would realistically enhance the sensitivity of dry deposition to climate variability and would result in a more accurate prediction of ground-level ozone.

Given the importance of ozone as a major tropospheric oxidant, air pollutant and greenhouse gas, an accurate representation of dry deposition is desirable (Jacob and Winner, 2009). Additionally, the significance of a realistic representation of land–atmosphere feedbacks rises in light of the changing Earth's climate with the projected increase of extreme events' frequency and intensity (Coumou and Rahmstorf, 2012).

Here, we present a revision of the existing Wesely-based dry deposition scheme in the Modular Earth Submodel System (MESSy), which has a very simplified representation of vegetation and soil. The modifications are done by well-established findings about the controls of stomatal and cuticular uptake of trace gases. The calculation of stomatal deposition fluxes is extended by including the vegetation density, two meteorological adjustment factors and an improved soil moisture availability function for plant stomata following the multiplicative algorithm by Jarvis (1976). For the first time in MESSy, a parameterization for cuticular dry deposition dependent on important meteorological and environmental variables is implemented explicitly (Zhang et al., 2003). In Sect. 2, a description of the model setup and the simulations is provided, whereas especially the transition to the new vertical exchange scheme is described in detail. Subsequently, the new VERTEX scheme is evaluated. In Sect. 4, the impact of the changes on ozone dry deposition is evaluated on daily and seasonal scales by comparison with measurements at four different sites. Here, advantages, uncertainties and missing processes in the revised scheme are identified. Next, the global impact on ground-level ozone is assessed by separating the effect of the different implemented parameterizations. Then, Sect. 6 provides a description of the uncertainties in modelling stomatal conductance and Sect. 7 comprises an investigation of the sensitivity to model resolution. Section 8 summarizes the main findings and the remaining process and model uncertainties which form the basis for the provided recommendations. Section 9 describes planned future developments.

2 Model description

This study uses the ECHAM/MESSy atmospheric chemistry model. MESSy v2.54 (Jöckel et al., 2010) provides a flexible infrastructure for coupling processes to build comprehensive

Earth system models (ESMs) and is utilized here with the fifth-generation European Centre Hamburg general circulation model (ECHAM5; Roeckner et al., 2003) as an atmospheric general circulation model. The dry deposition process of gases is calculated within the submodel DDEP (Kerkweg et al., 2006). This is described in Sect. 2.2. It relies on the VERTEX vertical exchange submodel (Sect. 2.1), former E5VDIFF, which contains the calculation of stomatal uptake (Eq. 5) and soil moisture stress (Eq. 12). The stomatal uptake parameterization is the base for the evapotranspiration scheme in VERTEX (Appendix B) which also incorporates the soil moisture stress.

2.1 The new VERTEX vertical exchange submodel

The VERTEX submodel represents land–atmosphere exchange and vertical diffusion as an alternative to the default E5VDIFF submodel in ECHAM5/MESSy. In 2016, Huug Ouwersloot branched VERTEX off from E5VDIFF. He optimized the code and applied bug fixes. This includes changes in calculation of the transfer coefficients for vertical diffusion, the latent heat vaporization, the convective transfer coefficient, the storage of the friction velocity, the roughness length over sea, the kinematic heat and moisture fluxes and the 2 and 10 m friction velocity. A detailed description can be found in the Supplement.

2.2 Dry deposition over vegetation

Dry deposition of trace gases to vegetation is calculated according to the multiple resistance scheme by Wesely (1989) shown in Fig. 1. The scheme, originally designed for a regional model with 11 land types and five seasonal categories, is used here with six generalized land types (Kerkweg et al., 2006). This was adapted by Ganzeveld and Lelieveld (1995) to the surface scheme of the ECHAM climate model (Klimarechenzentrum et al., 1992). The vegetation canopy is represented as one system; i.e. the detailed structure and plant characteristics are neglected (one big-leaf approach). Only one assumption about the canopy structure is made: the leaves are horizontally oriented and the leaf density is uniformly vertically distributed (Sellers, 1985). This is required in the formula for the calculation of stomatal resistance (Eq. 5).

The resistances (in $\mathrm{s\,m^{-1}}$) in the big-leaf approach account for mass and energy transfer mainly exerted by the boundary layer turbulence (R_a), molecular diffusion via the quasi-laminar boundary layer (R_qbr) and heterogeneous losses at the surface (R_s) (Kerkweg et al., 2006). With these, the dry deposition velocity v_d of a trace gas X (in $\mathrm{s\,m^{-1}}$) is defined as follows:

$$v_\mathrm{d}(X) = \frac{1}{R_\mathrm{a} + R_\mathrm{qbr}(X) + R_\mathrm{s}(X)}. \tag{1}$$

The dry deposition flux $f_\mathrm{d}(X)$ (in $\mathrm{molecules\,m^{-2}\,s^{-1}}$) is determined by multiplying the dry deposition velocity with the trace gas concentration $C(X)$ (in $\mathrm{molecules\,m^{-3}}$):

$$f_\mathrm{d}(X) = -v_\mathrm{d}(X) \cdot C(X). \tag{2}$$

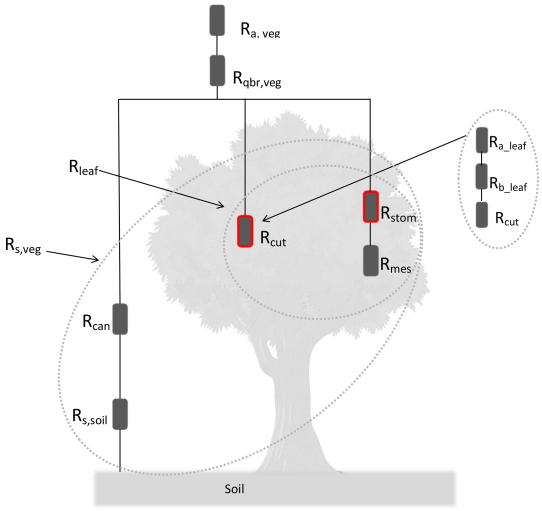

Figure 1. Dry deposition resistance analogy (adapted from Zhang et al., 2003); modified resistors are marked with red boxes.

The total resistance over land combines the resistances over snow, soil, vegetation (veg) and wet skin (ws) weighted by the respective land-covered fraction of a grid box (Kerkweg et al., 2006). In the following, only the latter two are considered. The resistances R_a and R_qbr are commonly parameterized with standard formulations from micrometeorology (Kerkweg et al., 2006; Wesely and Hicks, 1977). For the surface resistance over vegetation ($R_\mathrm{s,veg}$), the parameterization according to Zhang et al. (2003) is used:

$$\frac{1}{R_\mathrm{s,veg}(X)} = \frac{1}{R_\mathrm{can} + R_\mathrm{s,soil}(X)} + \underbrace{\frac{1}{R_\mathrm{cut}(X)} + \frac{1}{R_\mathrm{stom,corr}(X) + R_\mathrm{mes}(X)}}_{R_\mathrm{leaf}(X)}, \tag{3}$$

which consists of the soil resistance ($R_\mathrm{s,soil}(X)$), the in-canopy aerodynamic resistance (R_can) (as in Kerkweg et al., 2006) and the leaf resistance ($R_\mathrm{leaf}(X)$). The gas uptake by leaves (leaf) can be separated in two parallel pathways: the cuticular (cut) and the stomatal (stom) with its associated mesophilic pathway (mes), where the latter has negligible resistance for ozone and highly soluble species (Wesely, 1989). In contrast to the default formulation in MESSy (Eq. A1), the resistances in the updated scheme are provided at canopy scale in order to avoid linear scaling with the leaf area index (LAI, area of leaves [$\mathrm{m^2}$]/surface area [$\mathrm{m^2}$]). In fact, the linear scaling of resistances with LAI assumes that the

leaves act in parallel and overestimates the uptake for high LAI values (> 3–4) (Ganzeveld et al., 1998; Baldocchi et al., 1987). Furthermore, the quasi-laminar boundary resistance of individual leaves is included through the cuticular deposition scheme (see Sect. 2.2.2), whereas $R_{\mathrm{qbr,veg}}$ is a separate term in the old formulation (Eq. A1).

Due to the importance of stomatal and cuticular uptake for ozone dry deposition, their respective parameterizations are modified in this study (see Sect. 2.2.1 and 2.2.2). Also, ozone deposition to soil might be an important pathway (Schwede et al., 2011; Fares et al., 2012) but process understanding remains limited due to scant observational constraints (Clifton et al., 2020b, a). Stella et al. (2011) showed an exponential increase of soil resistance with surface relative humidity in three agricultural data sets which, however, varies much between different sites (Stella et al., 2019) and contradicts previous findings (Altimir et al., 2006; Lamaud et al., 2002; Zhang et al., 2002). Models by, e.g. Mészáros et al. (2009); Lamaud et al. (2009) apply a linear dependence on soil water content for parameterizing soil resistance. These parameterizations rely on input variables like the minimum soil resistance (Stella et al., 2011) which introduce an uncertainty due to measurement constraints. Also, the performance of a mechanistic model as proposed by Clifton et al. (2020b) depends on many input variables and parameters whose estimation is challenging and mostly biome dependent. Due to these uncertainties and limitations, the current parameterization of soil resistance in MESSy (see Kerkweg et al., 2006 for details) was not modified in this study.

2.2.1 Uptake through plant stomata

The stomata are actively regulated openings between the plant cells. They are scattered mostly over the lower (hypostomatous) epidermis of leaves. They control the H_2O and CO_2 exchange by plants which is the essential coupling of vegetation to the atmosphere and therefore to weather and climate. Here, the default parameterization of stomatal resistance (Eq. A2) is extended by adding dependencies on meteorological variables according to the Simple Biosphere Model (SiB) by Sellers et al. (1986) based on previous work by Jarvis (1976) for temperature (T) and vapour pressure deficit (VPD):

$$R_{\mathrm{stom,corr}}(X) = \frac{R_{\mathrm{stom}}(\mathrm{PAR},\mathrm{LAI})}{f(W_{\mathrm{s}}) \cdot f(T) \cdot f(\mathrm{VPD})} \cdot \frac{D_{\mathrm{H_2O}}}{D(X)}. \tag{4}$$

The optimal stomatal resistance for water ($R_{\mathrm{stom}}(\mathrm{PAR},\mathrm{LAI})$) is corrected with the ratio of the molecular diffusivity of the species ($D(X)$) and water ($D_{\mathrm{H_20}}$). The optimal stomatal resistance depends on the photosynthetically active radiation (PAR) and LAI (Ganzeveld and Lelieveld, 1995; Sellers, 1985):

$$R_{\mathrm{stom}}(\mathrm{PAR},\mathrm{LAI}) = \frac{kc}{\left[\frac{b}{\mathrm{dPAR}} \ln\left(\frac{d\exp(k\mathrm{LAI})+1}{d+1}\right) - \ln\left(\frac{d+\exp(-k\mathrm{LAI})}{d+1}\right)\right]}, \tag{5}$$

where $k = 0.9$ is the extinction coefficient, $c = 100\,\mathrm{s\,m^{-1}}$ is the minimum stomatal resistance, and $a = 5000\,\mathrm{J\,m^{-3}}$, $b = 10\,\mathrm{W\,m^{-2}}$ and $d = \frac{a+b\cdot c}{c\cdot \mathrm{PAR}}$ are fitting parameters (Sellers, 1985). For historical reasons, LAI was set to 1 in order to obtain the stomatal resistance at leaf level (Ganzeveld and Lelieveld, 1995). This has been changed and the seasonal evolution of stomatal resistance now follows the LAI which, in our study, is based on a 5-year climatology of monthly normalized difference vegetation index (NDVI) satellite data (Ganzeveld et al., 2002).

First, the stomatal resistance is corrected by the inverse of the temperature stress factor ($1/f(T)$) derived by Jarvis (1976):

$$f(T) = b_3(T - T_l)(T_h - T)^{b_4} \tag{6}$$

$$b_3 = (T_0 - T_l)(T_h - T_0)^{-b_4} \tag{7}$$

$$b_4 = (T_h - T_0)/(T_h - T_l), \tag{8}$$

where the empirical parameters are $T_h = 318.15\,\mathrm{K}$, $T_l = 268.15\,\mathrm{K}$ and $T_0 = 298.15\,\mathrm{K}$.

Secondly, following the analysis by Katul et al. (2009), a stress factor dependent on vapour pressure deficit ($1/f(\mathrm{VPD})$) was added to the calculation of stomatal resistance in VERTEX:

$$p_{\mathrm{H_2O,sat}}(T) = 0.61078 \exp\left(\frac{17.1 \cdot T(p_{\mathrm{H_2O}})}{235 + T(p_{\mathrm{H_2O}})}\right) \tag{9}$$

$$\mathrm{VPD} = p_{\mathrm{H_2O,sat}}(T) - p_{\mathrm{H_2O}} = \left(1 - \frac{\mathrm{RH}}{100}\right) p_{\mathrm{H_2O,sat}}(T) \tag{10}$$

$$f(\mathrm{VPD}) = \mathrm{VPD}^{-\frac{1}{2}}, \tag{11}$$

with $T(p_{\mathrm{H_2O}})$ (in K) as the surface temperature, $p_{\mathrm{H_2O}}$ (in kPa) as the pressure of water vapour and $p_{\mathrm{H_2O}}(T)$ [kPa] the pressure of saturated air. The vapour pressure deficit is calculated according to Kraus (2007).

While the stomatal resistance at canopy scale is actually calculated within the MESSy VERTEX submodel, the submodel DDEP uses it for the calculation of dry deposition fluxes. Thus, in DDEP, the user can choose between the old scheme based on Ganzeveld and Lelieveld (1995) and the new scheme actually using the stomatal resistance at canopy scale. The latter is activated by setting the DDEP *&CTRL* namelist parameter *l_ganzeori* to *.FALSE.*. How the stomatal resistance is calculated is chosen in VERTEX by the *&CTRL* namelist parameter *irstom*.

- *irstom=0* activates the original parameterization.
- Separate modifications:

  - *irstom=2*: variable LAI,
  - *irstom=3*: T dependency and
  - *irstom=4*: VPD dependency, respectively.
- *irstom=5*: all modifications.
- *irstom=1*: stomatal resistance with variable LAI at leaf scale. Instead of choosing LAI of 1 in Eq. (5) to represent the stomatal resistance at leaf level, as is done by the original code, Eq. (5) is calculated at canopy level using the actual LAI and then multiplied by LAI to obtain the average stomatal resistance at leaf level. For this case, the DDEP namelist parameter *l_ganzeori* has to be set to *.TRUE.*.

The stomatal activity of plants and the strength of surface–atmosphere coupling strongly depend on the parameterized plant–water stress (Combe et al., 2016). The soil water budget is represented by a "bucket scheme" where the soil water in a single layer is prescribed by a geographically varying predefined field capacity and soil wetness governed by transpiration, precipitation, runoff, snow melt and drainage (Roeckner et al., 2003). This scheme is used by so-called "first-generation" models. However, EMAC controls evapotranspiration through the stomatal resistance (Appendix B), which is the most important feature of biophysical ("second-generation") land surface models. Thereby, the stomatal resistance is calculated often like the one described here (Eq. 4) including temperature, VPD and soil moisture stress (Seneviratne et al., 2010; Sellers et al., 1997). The originally used plant–water stress function of Jarvis (1976) and Sellers et al. (1986), however, relies on leaf water potential ($f(\psi)$) for different plant types, which is difficult to estimate. Hence, EMAC uses a plant–water stress function dependent on soil moisture ($f(W_\mathrm{s})$. The default parameterization (Eq. A3, *ifws* $= 0$ in VERTEX *&CTRL*), applies the permanent wilting point of plants (W_pwp, 35 % of field capacity[1]) as a lower threshold in the calculation of the soil moisture stress factor ($f(W_\mathrm{s})$). However, soil moisture is significantly underpredicted by the model in some regions and the calculated $f(W_\mathrm{s})$ can be 0 for long periods. This is unrealistic and effectively shuts down dry deposition, e.g. during the dry season in the Amazon region. For this reason, $f(W_\mathrm{s})$ is parameterized here according to the original formulation by Delworth and Manabe (1988) by removing the lower limit:

$$f(W_\mathrm{s}) = \begin{cases} 1 & W_\mathrm{s}(t) > W_\mathrm{cr} \\ \frac{W_\mathrm{s}(t)}{W_\mathrm{cr}} & W_\mathrm{s}(t) \leq W_\mathrm{cr}, \end{cases} \tag{12}$$

where $W_\mathrm{s}(t)$ is the surface soil wetness (in m). W_cr (in m) is defined as the critical soil moisture level (75 % of the field capacity) at which the transpiration of plants is reduced. The modified parameterization in Eq. (12) can be applied by setting the *&CTRL* parameter *ifws* = in the VERTEX namelist.

[1] maximum amount of water the soil can hold against gravity over periods of several days

2.2.2 Cuticular deposition

According to several field studies (e.g. Van Pul and Jacobs, 1994; Hogg et al., 2007; Fares et al., 2012), cuticular deposition is an important contributor to ozone uptake and should not be neglected in models. Therefore, an explicit parameterization of cuticular deposition as used in many North American air quality modelling studies (Huang et al., 2016; Kharol et al., 2018) has been implemented. The gas uptake by leaf surfaces is based on two parallel routes, for which an analogy to ozone (highly reactive) and sulfur dioxide (very soluble) is used. The cuticular resistance is calculated as

$$R_\mathrm{cut}(X) = \frac{R_\mathrm{cut,d}(\mathrm{O_3})}{10^{-5} \cdot H(X) + s_\mathrm{reac}(X)}, \tag{13}$$

where $H(X)$ is the effective Henry's law coefficient as a measure of the solubility. The reactivity of a species is rated by the parameter s_reac. For highly reactive species ($s_\mathrm{reac} = 1$), the same property as for ozone is assumed (second term in Eq. 13), while for less reactive species ($s_\mathrm{reac} = 0.1, 0$) the uptake is effectively reduced (Wesely, 1989). For soluble species, the uptake at wet skin is assumed to be similar to the one of sulfur dioxide and is calculated as

$$R_\mathrm{ws}(X) = \left[\frac{1/3}{R_\mathrm{cut,w}(\mathrm{SO_2})} + 10^{-7} \cdot H(X) + \frac{s_\mathrm{reac}(X)}{R_\mathrm{cut,w}(\mathrm{O_3})} \right]^{-1}, \tag{14}$$

where $R_\mathrm{cut,w}(\mathrm{SO_2})$ and $R_\mathrm{cut,w}(\mathrm{O_3})$ are the resistances of sulfur dioxide and ozone at wet surfaces, respectively. The constant values of the default formulae (Eqs. A4, A5) are replaced by parameterizations which account for the meteorological dependence of cuticular uptake according to Zhang et al. (2002):

$$R_\mathrm{cut,d}(\mathrm{O_3/SO_2}) = \frac{R_\mathrm{cut,d0}(\mathrm{O_3/SO_2})}{\exp(0.03 \cdot \mathrm{RH}) \cdot \mathrm{LAI}^{0.25} \cdot u_*} \tag{15}$$

$$R_\mathrm{cut,w}(\mathrm{O_3/SO_2}) = \frac{R_\mathrm{cut,w0}(\mathrm{O_3/SO_2})}{\mathrm{LAI}^{0.5} \cdot u_*}, \tag{16}$$

where the cuticular resistance of O_3 and SO_2, respectively, is distinguished for dry canopies ($R_\mathrm{cut,d}$) and wet canopies ($R_\mathrm{cut,w}$) depending on relative humidity (RH in %), LAI (in $\mathrm{m^2\,m^{-2}}$) and friction velocity (u_* in $\mathrm{m\,s^{-1}}$). The input parameters are $R_\mathrm{cut,d0}(\mathrm{O_3})$=5000 $\mathrm{s\,m^{-1}}$, $R_\mathrm{cut,w0}(\mathrm{O_3}) = 300\,\mathrm{s\,m^{-1}}$ and $R_\mathrm{cut,d0}(\mathrm{SO_2}) = 2000\,\mathrm{s\,m^{-1}}$ (Zhang et al., 2002). For rain and dew conditions, values of $50\,\mathrm{s\,m^{-1}}$ and $100\,\mathrm{s\,m^{-1}}$ are prescribed for $R_\mathrm{cut,w0}(\mathrm{SO_2})$. In contrast to traditional approaches, these parameterizations also consider the aerodynamic and the quasi-laminar boundary resistances of individual leaves. For the usage in MESSy, this can be switched on via *l_ganzeori=.FALSE.* in the *&CTRL* namelist of DDEP.

2.3 Simulations

In order to answer the different research questions of this study, two different types of simulations have been performed (Table 1).

1. The first kind were simulations to investigate dry deposition and the effect of the modifications in VERTEX:
   these simulations are based on the Chemistry-Climate Model Initiative (CCMI) setup (Jöckel et al., 2016). To allow for comparison with measurements, the model dynamics have been nudged towards realistic meteorology by the assimilation of data from the European Centre for Medium-Range Weather Forecasts (ECMWF) (Jöckel et al., 2010). Additionally, the QCTM mode is used; i.e. the chemistry does not feed back to the dynamics, resulting in the same meteorology for all simulations (Deckert et al., 2011). All modifications for the dry deposition scheme are employed in a 7-year simulation (REV, 2009–2015). Additionally, a 1.5-year simulation covering the period 2017 to July 2018 (2017 as spin-up) has been performed to cover the measurement periods (Sect. 4). For the same periods, simulations with the same configuration, except applying the default dry deposition scheme (DEF), have been conducted. The individual effects of the different modifications are investigated by two 2-year simulations employing the different namelist switches (Sect. 2.2). Moreover, a free-running sensitivity simulation with an additional temperature and drought stress factor for evapotranspiration (Appendix B) has been performed aiming at an improved representation of local meteorology especially in the Amazon. The station simulation output and the global output are analysed in Sects. 4 and 5, respectively. In addition, two 2-year simulations are realized for different horizontal resolutions (REST42, REST63) to investigate the resolution dependency of dry deposition (Sect. 7). All these simulations use 31 model layers with the top at 10 hPa and take the first year of simulation as spin-up.

2. The second kind were simulations for the evaluation of VERTEX as the boundary layer scheme:
   two pure dynamical (i.e. without chemistry) 30-year simulations with the old (clim-E5) and the new boundary layer description (clim-VER), respectively, have been performed.

All simulations were performed at the Jülich Supercomputing Centre with the JURECA Cluster (Jülich Supercomputing Centre, 2018).

3 VERTEX evaluation

In order to advise the usage of VERTEX (with the default settings) as the default vertical exchange submodel in MESSy, the dynamics produced by both submodels are compared. Therefore, two dynamical, free-running 30-year simulations have been performed using the E5VDIFF or the VERTEX submodels, respectively. To obtain a comparable radiative imbalance at TOA (top of the atmosphere) with VERTEX, the four cloud parameters have been tuned in advance according to Mauritsen et al. (2012). The tuning factors can be found in Table 2. The radiative imbalance at TOA is slightly positive at present-day conditions (Mauritsen et al., 2012; Stephens et al., 2012); here, E5VDIFF gives a negative value. The difference between the tuned VERTEX and E5VDIFF is small and within the uncertainty range of $\pm 0.4\,\mathrm{W\,m^{-2}}$.

Additionally, global mean values of surface temperature, cloud liquid water, relative humidity and planetary boundary layer height of EMAC using E5VDIFF and EMAC using VERTEX with the respective uncertainty range for the period 1979–2008 are represented in Fig. 2. The results for cloud liquid water and planetary boundary height show no significant differences between the VERTEX and E5VDIFF simulations since the annual mean of each falls in the confidence interval of the other. This is not always the case for surface temperature and relative humidity. However, the 30-year means of surface temperature and relative humidity simulated by E5VDIFF and VERTEX are not significantly different.

4 Evaluation with deposition measurements

To assess the impact of the code revision/modifications on the variability of dry deposition, we compare the sensitivity simulations DEF, REV, REV-fTfVPD, REV-fws and REV-NNTR (see Table 1, all at T106L31 resolution) with dry deposition measurements at four field sites (listed in Table 3). The chosen data sets are the best available of ozone dry deposition (flux data and ozone mixing ratio or velocity data) with the required temporal resolution and coverage of diverse biomes of the world. The analysis is aimed at covering the recent decade, which includes the most extreme drought and heat events (where the stomatal stress factors are aimed). For the reason of uniqueness and importance of atmospheric processes in a remote and pristine forest like the Amazon, we included measurements from, among others, the Amazon Tall Tower Observatory (ATTO). Ozone dry deposition fluxes were measured with the eddy covariance and gradient method (Ontario). From these data, deposition velocities were calculated by the means of ozone concentration data. The eddy covariance technique determines a turbulent flux by the covariance of the measured vertical velocity and the gas concentration. Due to the stochastic nature of turbulence, these measurements have an uncertainty of 10 % to 20 % under typical observation conditions (Rannik et al., 2016). For the gradient method used at the Borden forest research station, the dry deposition flux was estimated from concentration gradients below and above the canopy and the eddy diffusivity according to the Monin–Obukhov similarity theory. The estimated dry deposition velocities (V_d) show an uncertainty of $\approx 20\,\%$, which is due to the assigned canopy, the inherent limitations of the algorithm and the measurement uncertainties in concentrations. However, results are in good

Table 1. List of EMAC simulations

Simulation	Spatial resolution	Time period	Remarks
(1) Dry deposition mechanism: CCMI chemistry, nudged, no feedbacks (QCTM)			
REST42	T42L31 (2.8° × 2.8°)	2009/2010	irstom=5, ifws=1, l_ganzeori=F
REST63	T63L31 (1.9° × 1.9°)	2009/2010	irstom=5, ifws=1, l_ganzeori=F
REV (revised)	T106L31 (1.1° × 1.1°)	2009–2015, 2017–June 2018	irstom=5, ifws=1, l_ganzeori=F
DEF (default)	T106L31 (1.1° × 1.1°)	2009–2015, 2017–June 2018	default ddep scheme
REV-fws	T106L31 (1.1° × 1.1°)	2009/2010	irstom=5, ifws=0, l_ganzeori=F
REV-fTfD	T106L31 (1.1° × 1.1°)	2009/2010	irstom=2, ifws=1, l_ganzeori=F
REV-NNTR	T106L31 (1.1° × 1.1°)	2014/2015	free-running, all ddep modifications (as REV), all stress factors applied to evapotranspiration (izwet=1)
(2) Climatology comparison: no chemistry, free-running			
clim-E5	T42L90 (2.8° × 2.8°, up to 0.01 hPa)	1979–2008	E5VDIFF for vertical exchange
clim-VER	T42L90 (2.8° × 2.8°, up to 0.01 hPa)	1979–2008	VERTEX for vertical exchange

Table 2. Overview of tuning parameter settings and global mean properties.

Parameters		EMAC (E5VDIFF)	EMAC (VERTEX)
Cloud mass flux above level of non-buoyancy		0.3	0.3
Entrainment rate for shallow convection		1×10^{-3}	1×10^{-3}
Entrainment rate for deep convection		1×10^{-4}	1×10^{-4}
Conversion rate to rain in convective clouds		1.5×10^{-4}	1.6×10^{-4}
Properties	**Observed***	**EMAC (E5VDIFF)**	**EMAC (VERTEX)**
Total cloud cover [%]		67.12	67.27
Water vapour path [$\mathrm{kg\,m^{-2}}$]		25.03	24.83
Liquid water path [$\mathrm{kg\,m^{-2}}$]		0.077	0.077
Total precipitation [$\mathrm{mm\,d^{-1}}$]		1.28	1.31
Surface net shortwave [$\mathrm{W\,m^{-2}}$]	152–167	158.27	158.32
Surface net longwave [$\mathrm{W\,m^{-2}}$]	−(40–57)	−54.82	−54.93
Surface sensible heat flux [$\mathrm{W\,m^{-2}}$]	−(16–19)	−18.75	−19.65
Surface latent heat flux [$\mathrm{W\,m^{-2}}$]	−(75–87)	−87.45	−88.73
Planetary albedo [%]		32.38	32.37
Shortwave net at TOA [$\mathrm{W\,m^{-2}}$]	238–244	230.99	231.00
Longwave net at TOA [$\mathrm{W\,m^{-2}}$]	−(237–241)	−232.46	−232.55
Radiation imbalance at TOA [$\mathrm{W\,m^{-2}}$]		−1.47	−1.55

* Stevens and Schwartz (2012)

agreement with other eddy covariance measurements (Wu et al., 2016).

4.1 Annual cycle of dry deposition

The annual cycle of dry deposition is mainly driven by the evolution of vegetation and is generally represented well in models (Silva and Heald, 2018). Here, we use the long time series measured at Borden and Hyytiälä to identify the impact of the code modifications on the annual cycle of dry deposition velocity. The available micrometeorological data help to distinguish the different effects. From the hourly data, we calculated multiyear (2010–2012) monthly means. To explore the contribution of stomatal and cuticular uptake, the individual velocities are calculated for O_3 according to the model calculations (Kerkweg et al., 2006):

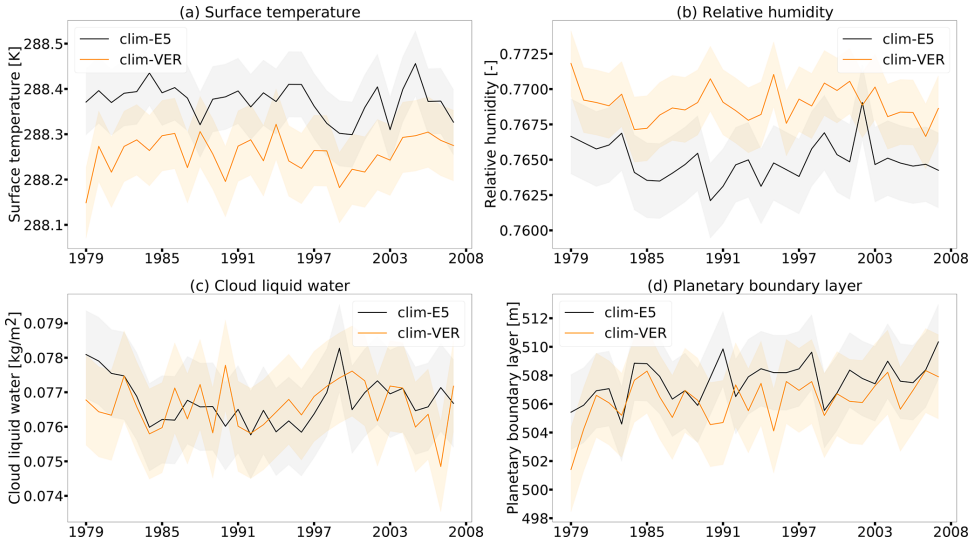

Figure 2. Global mean properties and the uncertainty range (95 % confidence interval in shaded) of the climatology simulations with E5VDIFF (clim-E5) and with VERTEX (clim-VER) for the period 1979–2008.

$$G_{\mathrm{cut,d}} = \frac{(1-\mathrm{ws})\cdot(1-\mathrm{cvs})\cdot\mathrm{veg}}{R_{\mathrm{cut,d}}(\mathrm{O_3})}$$

$$G_{\mathrm{cut,w}} = \frac{\mathrm{ws}\cdot(1-\mathrm{cvs})}{R_{\mathrm{cut,w}}(\mathrm{O_3})} \tag{17}$$

$$G_{\mathrm{ns}} = G_{\mathrm{cut,d}} + G_{\mathrm{cut,w}} \tag{18}$$

$$G_{\mathrm{stom}} = \frac{(1-\mathrm{ws})\cdot(1-\mathrm{cvs})\cdot\mathrm{veg}}{R_{\mathrm{stom,corr}}(\mathrm{O_3})} \tag{19}$$

$$v_{\mathrm{p}} = \frac{G_{\mathrm{p}}}{G_{\mathrm{stom}} + G_{\mathrm{ns}}}\cdot v_{\mathrm{d}}, \tag{20}$$

where G names the individual conductances (inverse of resistance) of stomata (stom), dry cuticle (cut,d), wet cuticle (cut,w) and non-stomata (ns). Here, veg, ws and cvs give the vegetation fraction, the wet skin fraction and the snow-covered fraction, respectively. G_{p} and v_{p} are the individual conductance and the velocity of one pathway. Further terms are described in Sect. 2.2.

The multiyear (2010–2012) annual cycle of the simulated dry deposition velocity at Borden forest (Fig. 3a) captures the observed cycle well until June. The new scheme reproduces the observations better than the old scheme. This is a consequence of the increase in nighttime mean velocities due to the much larger cuticular contribution (Fig. B1a, b). However, due to the overestimated stomatal uptake in the default scheme (see Sect. 2.2.1), only slight deviations from the new dry deposition scheme are visible in the daily mean shown in Fig. 3a. The mismatch of the simulated and measured V_{d} from August to October is a consequence of the underestimation of relative humidity leading to too-low simulated cuticular deposition (Fig. 3c, e). This effect exceeds the impact of the overestimation of relative humidity (only) in summer, because the LAI is higher in summer. In general, the cuticular uptake parameterization accounting for LAI, friction velocity, RH and surface wetness conditions performs, in our simulations, better than parameterizations without these dependencies as expected from the study of Wu et al. (2018). Unfortunately, the cuticular uptake parameterization also introduces uncertainties to the modelled non-stomatal uptake. Moreover, accounting for biogenic volatile organic compounds (BVOCs) like in Makar et al. (2017) would enhance in-canopy loss of ozone, significantly increase non-stomatal dry deposition and lead to improved simulation results (Wu et al., 2018). The representation of in-canopy air chemistry is outside the scope of the present study but planned within a subsequent study.

In contrast, the amplitude of the annual cycle and the mean of dry deposition fluxes in Hyytiälä are overestimated by both schemes during spring and summer (Fig. 3b). For the default scheme, this is due to the oversimplification of the stomatal uptake that only accounts for a constant LAI of $1\,\mathrm{m^2\,m^{-2}}$ (see Sect. 2.2.1), which is far from the measured LAI of 3–4 $\mathrm{m^2\,m^{-2}}$ during this period (Keronen et al., 2003). Enabling the new scheme (REV), increases the dry deposition velocity which reproduces the measured values in autumn better. The contribution of non-stomatal dry deposition of 25 %–45 % during the day reported by Rannik et al. (2012) is represented partly by that. However, the new scheme leads to an even higher overestimation by the model from April

Table 3. Dry deposition measurements. In the description of vegetation/climate, the reported LAI (in $m^2\,m^{-2}$) is given in brackets; v_d^{mod} and v_d^{obs} are the average measured and modelled dry deposition velocity.

Site	Vegetation/climate	Location (height)	Time period	v_d^{mod} (v_d^{obs}) $cm\,s^{-1}$	Reference
Hyytiälä, southern Finland (SMEAR II)	Boreal forest, Scots Pine, (LAI of 3–4)/cold temperate	61.85° N, 24.28° E (22 m/16 m[a])	2010–2012	0.29 (0.28)	Keronen et al. (2003)
Lindcove research station, California, USA	Citrus orchard (LAI of 3)/Mediterranean	36.35° N, 119.09° W (131 m)	Oct 2009–Nov 2010	0.22 (0.49)	Fares et al. (2012) and Fares et al. (2012–2014)[b]
Borden research station, Ontario, Canada	Mixed forest (LAI of 4.6)/temperate	44.19° N, 79.56° W (33 m)	2010–2012	0.34 (0.47)	Wu et al. (2018)
Amazon Tall Tower (ATTO), Manaus, Brazil	Rainforest (LAI of 6)/tropical humid	2.15° S, 59.01° W (41 m)	Nov 2015, Apr/May 2018	0.18 (0.67), 0.33 (1.0)	Available on request: Matthias Sörgel (m.soergel@mpic.de)

[a] Meteorological measurement height. [b] Ozone data are not available here.

to July. The sensitivity simulation REV-fws (default $f(W_s)$) points to the increase of the soil moisture stress function (see Sect. 2.2.1, Eq. 12) as one reason for the overestimation of V_d in summer (Fig. 3b, f). Moreover, the overestimation in June/July is partly ($\sim 10\,\%$) due to the too-high model LAI compared to the measured values of 3–4 (Fig. B2a). The remaining gap (Fig. 3f) can be explained by restricting the analysis to wet conditions (RH $> 70\,\%$) only and the analysis of the sensitivity simulation REF-fTfD (no $f(T)$ and $f(\mathrm{VPD})$). This suggests that the overestimated V_d (Fig. B2c) in summer is due to the stress factors for stomatal uptake since the modelled and measured temperatures are a mismatch. VPD has been identified by Rannik et al. (2012) as a strong driver of daytime total deposition velocity, which confirms the importance of inclusion of VPD dependence for stomatal uptake.

4.2 Importance of stress factors for the diurnal variation of deposition

The short-term measurements at Lindcove research station and at ATTO are used to assess the impact of the stress factors on the diurnal cycle of dry deposition velocity in spring and summer. Additionally, micrometeorological and additional flux data make possible to consider the stomatal resistance ($\sim$ inverse of the velocity, calculations according to Fares et al., 2012) and the underlying meteorological conditions. Since the respective micrometeorological measurements are not available at ATTO, data extracted from the ERA5 global climate reanalysis at the 1000 hPa pressure level (Copernicus, 2017) are used here.

The diurnal cycle of dry deposition velocity at the Lindcove research station follows the solar variation (Fares et al., 2012) and is generally well reproduced by the model with the best match in spring (Fig. 4). The revised dry deposition scheme reduces the underestimation of measured nighttime V_d due to the inclusion of cuticular uptake, which Fares et al. (2012) identified as an important ozone sink for exactly this measurement site. The measured dry deposition velocity increases at sunrise (around 15:00 UTC) and remains almost constant during the day. This is only reproduced by the revised dry deposition scheme. The comparison of the dry deposition velocity from the revised scheme (red line) and the velocity without stomatal T and VPD stress (gray line) in Fig. 4a illustrates the necessity of accounting for the stress factors. This is consistent with Fares et al. (2012), who reported a high negative correlation of $V_d(\mathrm{sto})$ with VPD and temperature and related it to stomatal stress. The direct comparison of the stomatal resistances calculated from measured and modelled variables (Fig. 4c) shows an improvement of the modelled resistances (comparing DEF and REV). However, the modelled daytime stomatal resistance is still too high compared to the measurements. This points to an underestimation of stomatal uptake by the model during the day. A small fraction can be explained by the direct effect of the stomatal soil moisture stress in the model which does

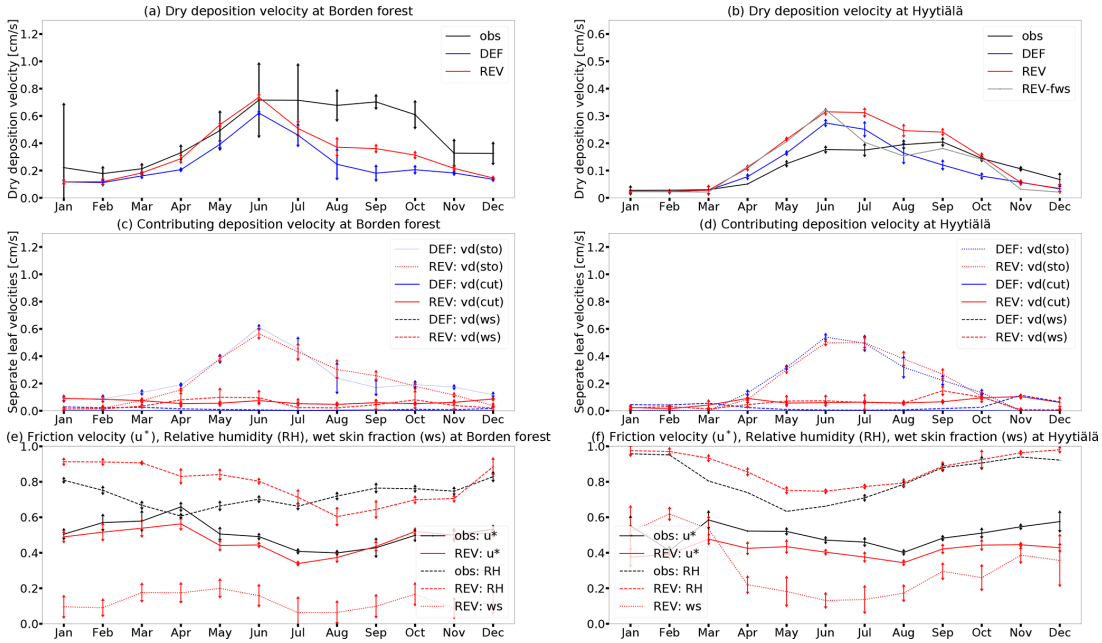

Figure 3. Measured (obs) and modelled (DEF, REV) multiyear mean (2010–2012) and REV-fws (2010) annual cycle. **(a, c, e)** Borden forest and **(b, d, f)** Hyytiälä; arrows indicate 1σ.

not occur in reality since the citrus orchard was watered during the measurement campaign. Contrastingly, in summer, the model underestimation of V_d is higher than in spring (Fig. 4b). As seen from the comparison of stomatal resistance values (Fig. 4d), the model underestimates the stomatal uptake. This is because the irrigation of the orchard leads to cooling sustained evapotranspiration and keeps $f(T)$ low. Thus, in the model, a too-high temperature stress acts on the stomata. Moreover, neglecting the soil moisture stress on stomata would bring the stomatal resistance values closer since the irrigation at the site ensures a constant and high soil moisture. The irrigation of the citrus orchard during the day also enhances surface wetness and favours deposition at cuticles (Fares et al., 2012; Altimir et al., 2006) which cannot be captured by the model. Fares et al. (2012) estimate the stomatal contribution to only account for 20 %–45 % of the total daytime dry deposition flux during both seasons and point to soil deposition and reactions of ozone with NO and VOCs as major sinks at the citrus orchard, especially during flowering season. The contribution of these pathways is expected to be enhanced by the inclusion of further BVOCs within the chemical mechanism and the explicit parameterization of in-canopy residence and transport.

Tropical forests are known to be effective O_3 sinks with observed mean midday maximum dry deposition velocity of $2.3\,\mathrm{cm\,s^{-1}}$ (Rummel et al., 2007) due to much higher LAI compared to other sites (e.g. Lindcove). The measured dry deposition velocity at ATTO shown in Fig. 5a and b is no exception but shows a high variability (standard deviation). The diurnal cycle follows the solar radiation with maximum V_d at 15:00 UTC and highest amplitude during the wet season (April–May 2018). The amplitude of the diurnal cycle is highly underestimated in both EMAC simulations, with the highest mismatch during daytime. This is similar for other models. In fact, Hardacre et al. (2015) report a general and large underestimation of dry deposition velocities by models over tropical forests with highest predicted values of $0.25\,\mathrm{cm\,s^{-1}}$. Here, the simulation with the revised dry deposition scheme (REV) shows only a minor increase of V_d during the wet season. Since stomatal uptake is known to be an important daytime sink (Freire et al., 2017), the underestimation of the total dry deposition flux is partly attributed to a too-low simulated stomatal uptake caused by the overestimation of temperature and the underestimation of relative humidity (Fig. B3). The increase of dry deposition velocity by the new scheme is mainly due to the lowered soil moisture stress on stomata ($f(W_s)$) shown in Fig. 5e. Freire et al. (2017) also links stomatal uptake to the efficiency of turbulent mixing in transporting ozone down to the canopy. In general, 10 % of the total ozone sink during daytime and 39 % during night are associated with in-canopy processes (Freire et al., 2017). Freire et al. (2017) and Bourtsoukidis

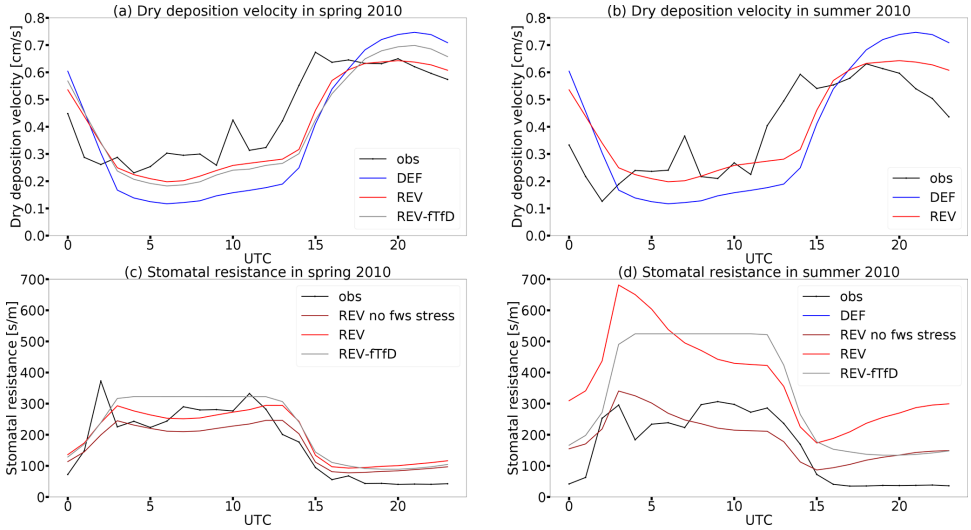

Figure 4. Diurnal cycles of measured (obs) and modelled (DEF, REV, REV-fTfD) ozone dry deposition velocity and stomatal resistance in spring and summer 2010 at Lindcove research station.

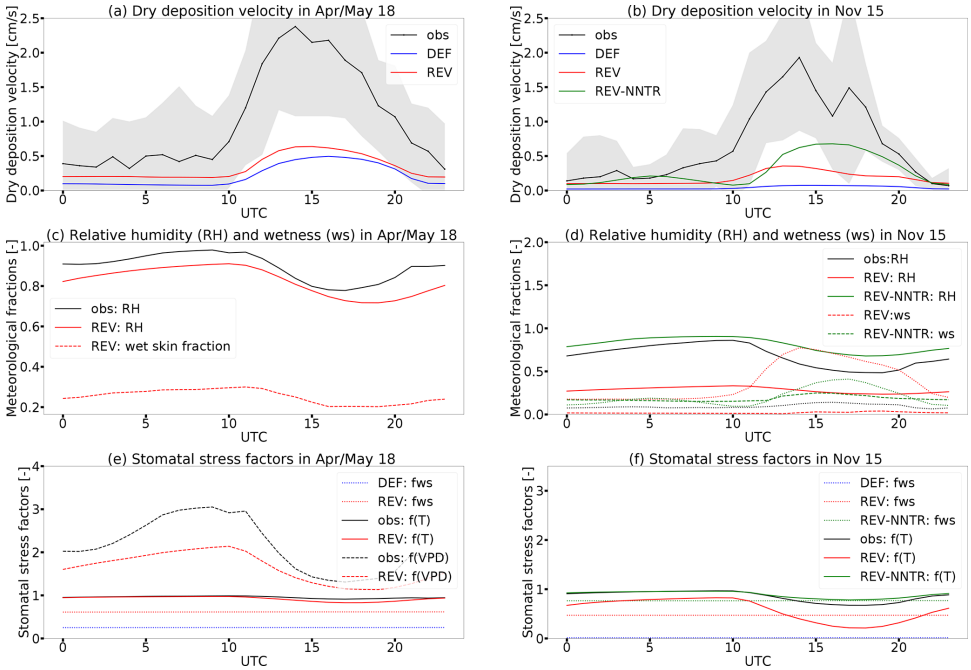

Figure 5. Diurnal cycles of measured (obs) and modelled (DEF, REV, REV-NNTR: free-running $f(T)$ and $f(\mathrm{VPD})$ for evapotranspiration) ozone dry deposition velocities in wet and dry seasons at ATTO (gray: standard deviation).

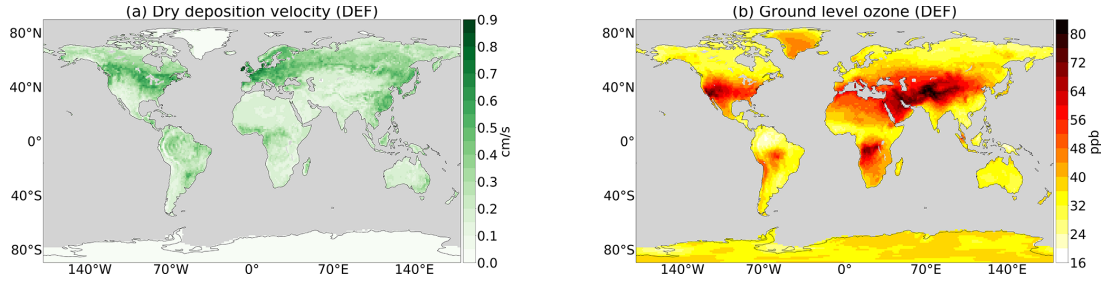

Figure 6. Multiyear (2010–2015) mean absolute values in boreal summer.

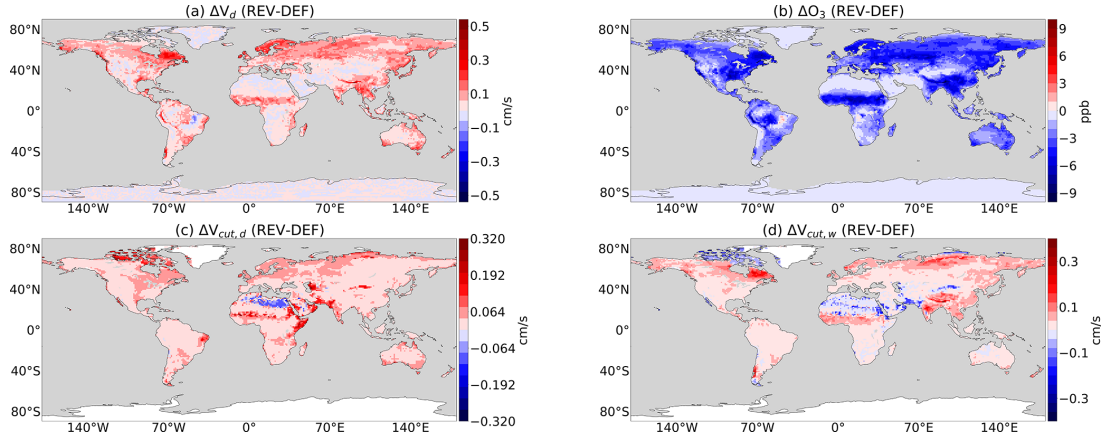

Figure 7. Multiyear (2010–2015) mean absolute changes in boreal summer: i.e. difference between the revised and default scheme (REV – DEF).

et al. (2018) identified the oxidation of sesquiterpenes as an important contributor to the chemical nighttime sink. Cuticular deposition might also play a role in humid conditions during night (Rummel et al., 2007), which is underestimated by the model due to the biased relative humidity (Fig. 5c).

The uncertainty introduced by the mismatching meteorology becomes even more obvious when comparing measurements and simulations for November 2015. This month was characterized by temperatures of 2 to 3 degreeC above average and unusually little rainfall (compared to usual conditions in this season) due to a strong El Niño event (National Centers for Environmental Information, 2016). The dryness is overestimated by the model with a too-high temperature ($\Delta = +5$ to $+8$ K), too-low relative humidity ($\Delta = -30\,\%$ to $-40\,\%$)) and too-dry soil. The lack of available soil moisture ($f(W_s) = 0$) effectively shuts down stomatal deposition in the default simulation (DEF), whereas the modification of the soil moisture stress function (neglecting the artificial lower limit; see Eq. 12) in the revised model (REV) allows for an increased deposition (Fig. 5b). The temperature and relative humidity biases result in corresponding mismatching stress factors for the stomata that are double the ones derived from reanalysis data (Fig. 5f). This mismatch leads to an underestimation of stomatal uptake. This result is confirmed by the sensitivity simulation REV-NNTR for which no meteorological nudging has been applied, and the stress factors $f(T)$ and $f(\mathrm{VPD})$ are also used for the calculation of evapotranspiration. The REV-NNTR simulation yields much more realistic results compared to the measurements, capturing at least 50 % of the measured V_d during the day (Fig. 5b). This improvement is partly due to the omission of nudging, as the latter can have a detrimental effect on precipitation and evaporation (Jeuken et al., 1996). The temperature bias of the model is associated with the missing soil moisture buffer simulated by the bucket scheme. Incorporating a 5-layer scheme has been shown to lead to a more realistic soil water storage capacity, especially in the Amazon, and to a removal of this bias (Hagemann and Stacke, 2013). Nevertheless, the REV-NNTR simulation suggests that the stress factors $f(T)$ and $f(\mathrm{VPD})$ significantly contribute to buffer soil moisture and ameliorate the dryness bias.

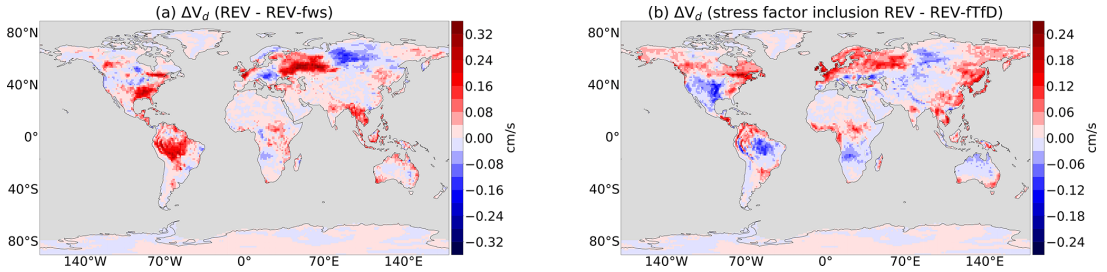

Figure 8. Mean changes (2010) of dry deposition velocity in boreal summer. **(a)** $f(W_s)$ modification; **(b)** temperature and VPD stress.

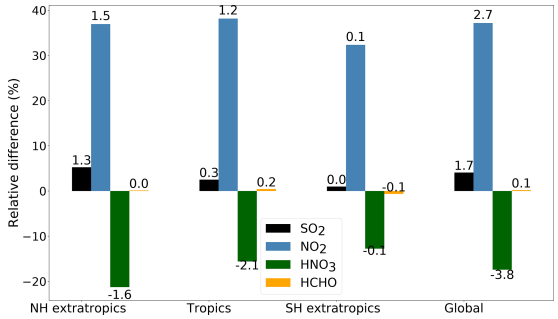

Figure 9. Relative change [%] and absolute change [Tg yr^{-1}] (numbers on bars) of annual global loss by dry deposition of O_3, SO_2, HNO_3 and HCHO (REV – DEF).

5 Global impact on ground-level ozone

Given the importance of dry deposition for ground-level ozone and the uncertainty of dry deposition parameterizations in models (Young et al., 2018; Hardacre et al., 2015), the global impact of the implemented code changes is assessed in this section. The global (boreal) summer mean distributions of deposition velocity and ground-level mixing ratio for O_3 shown in Fig. 6a–b are generally in the same range as reported for global models (e.g. Val Martin et al., 2014; Hardacre et al., 2015). However, like most global models, EMAC overestimates tropospheric ozone in comparison to satellite observations (Righi et al., 2015). Applying the revised dry deposition scheme increases the mean summer V_d by up to 0.5 cm s^{-1} (Fig. 7a). The highest fraction of this increase arises from the inclusion of cuticular uptake at wet surfaces ($V_{cut,w}$) (Fig. B4b). The effect is large over the most northern continental regions (Fig. 7d) and even more pronounced where LAI is high like in Scandinavia and eastern Canada (for LAI distribution, see Fig. B4a). Additionally, the uptake at dry surfaces ($V_{cut,d}$) is enhanced with up to 0.3 cm s^{-1} higher dry deposition velocity (Fig. 7c). This is because the default scheme applies a very high constant resistance for this process.

Concerning the stomatal deposition, the impacts of three different stress factors are considered. First, over relatively dry soil, i.e. where soil moisture exceeds 35 % of field capacity (wilting point of plants), the soil moisture stress is reduced by the modified parameterization. Neglecting the plants' wilting point as the lower limit for soil moisture stress on stomata weakens the dependency on field capacity. Thus, dry deposition is enhanced by up to 0.32 cm s^{-1}, as illustrated in Fig. 8a. Second, the inclusion of temperature and (third) VPD adjustment factors, indeed, leads to a spatially varying impact of ±0.27 cm s^{-1} change in V_d (Fig. 8b). In humid and cold temperate regions, like Siberia and Canada, no temperature stress appears and the VPD adjustment factor increases the stomatal uptake. In the eastern US, Kazakhstan and central Amazon during boreal summer, stomata are stressed by temperature and VPD. This effect is overpredicted by the model, as the humidity over the Amazon forest is probably too low in the model (see Fig. B3). The stress factors are shown in Fig. B4c and d.

However, the overall decrease in ozone concentration dampens the impact of the change in dry deposition flux. In total, the changes by the revised dry deposition scheme increase the multiyear mean (2010–2015) loss of ozone by dry deposition from 946 to 1001 Tg yr^{-1} (Young et al., 2018; Hu et al., 2017). Accordingly, (boreal) summer ground-level ozone over land is reduced by up to 12 ppb (24 %), peaking over Scandinavia, Asia, central Africa and eastern Canada (Fig. 7b). In the Northern Hemisphere, also the zonal mean of the tropospheric ozone mixing ratio show a noticeable reduction far from the ground compared to the default scheme (Fig. 11a). This has the potential to reduce the positive bias of tropospheric ozone on the Northern Hemisphere (20 %) reported by Young et al. (2018). However, besides ozone, also other atmospheric tracer gases are affected by the change in dry deposition. The global annual dry deposition flux of odd oxygen (O_x)[2], which includes many important tropospheric trace gases, increases from 978 to 1032 Tg yr^{-1} due to the revision. This is in good agreement with the reported numbers by Hu et al. (2017) and Young et al. (2018). In Fig. 9,

[2] $O_x \equiv O + O_3 + NO_2 + 2NO_3 + 3N_2O_5 + HNO_3 + HNO_4 + BrO + HOBr + BrNO_2 + 2BrNO_3 + PAN$

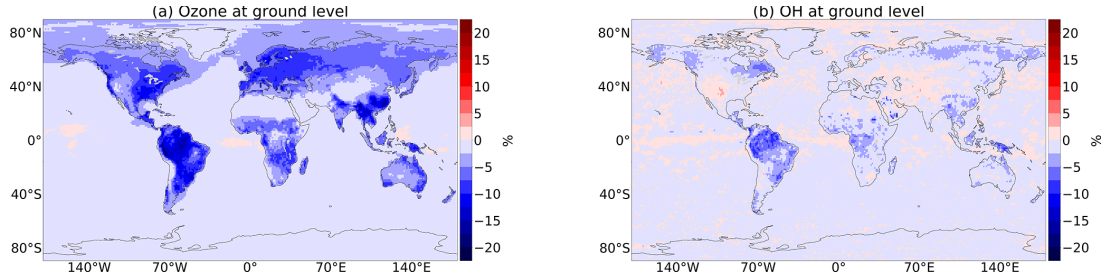

Figure 10. Relative change of multiyear (2010–2015) mean at ground level (DEF – REV).

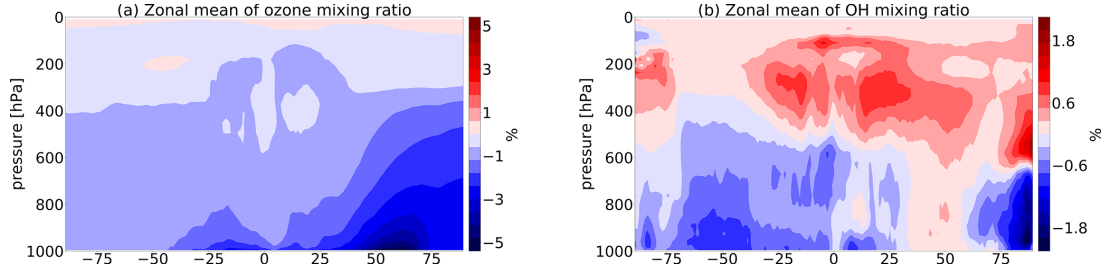

Figure 11. Relative change of multiyear (2010–2015) zonal mean (DEF – REV).

we show additionally the absolute and relative change of the multiyear annual average dry deposition loss of SO_2, NO_2, HNO_3 and HCHO. As a very soluble species, the loss of SO_2 is increased by the revised dry deposition scheme, whereas the predefined low cuticular and wet skin resistance of HNO_3 in the old scheme were replaced with the new mechanism, leading to an decrease in dry deposition. The altered loss of NO_2 and HCHO and other ozone precursors at ground level, especially soluble oxygenated VOCs, contributes to the total change in ozone loss. NO_2 is deposited almost 40 % more significantly, contributing to the net reduction in ozone production but is mostly counterbalanced by other processes. The change of HCHO dry deposition flux is small on a global and annual scale and only important regionally, mostly in (boreal) summer, when it decreases HCHO at ground level (Fig. 12b) by up to 25 %. Thereby, the change in wet uptake is highest but is partially counterbalanced by other effects. This leads to lower HO_2 production from HCHO photooxidation and lower NO-to-NO_2 conversion and thus lower ozone production (Seinfeld and Pandis, 2016). These effects also impact the OH mixing ratio (Figs. 10b, 11b) which controls the methane lifetime predicted by the model. However, for a clearer effect, a longer simulated time period would be needed. A detailed analysis of the trace gas budgets is beyond the scope of this paper and will be investigated in a subsequent study.

6 Uncertainties in modelling stomatal conductance

Dry deposition is a highly uncertain term in modelling ozone pollution (Young et al., 2018; Clifton et al., 2020a). Its representation is generally limited by a lack of measurements and process understanding but also to a large extent driven by the quality of land cover information (Hardacre et al., 2015; Clifton et al., 2020b). Although the dry deposition scheme by Wesely (1989) is commonly used in global and regional models (e.g. MOZART, GEOS-Chem), the approach has some constraints (Hardacre et al., 2015). The disadvantage of the big-leaf approach used in MESSy is that a vertical variation of leaf properties, affecting, for instance, the attenuation of solar radiation, is not considered (e.g. Clifton et al., 2020b). Regarding stomatal uptake, we neglect the mesophyll resistance as reactions inside the leaf are commonly assumed to not limit stomatal ozone uptake, whereas, besides mostly supporting laboratory studies (e.g. Sun et al., 2016), a few contradicting findings exist (e.g. Tuzet et al., 2011). The here-used empirical multiplicative algorithm by Jarvis (1976) for stomatal modelling has one general drawback concerning that the environmental responses to stomata are treated clearly in contrast to experimental evidence (Damour et al., 2010). However, Jarvis-type models have been shown to be able to compete with the semi-mechanistic $A_{net} - g_s$ models which link stomatal uptake to the CO_2 assimilation during plant photosynthesis (Fares et al., 2013; Lu, 2018). The critics in Fares et al. (2013) state that the Jarvis

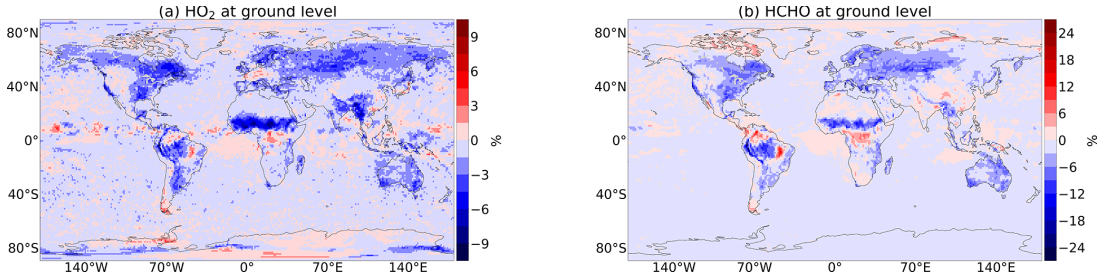

Figure 12. Relative change of multiyear (2010–2015) boreal summer mean (DEF – REV).

model cannot capture the afternoon depression of ozone dry deposition is due to the original used VPD stress factor which has been replaced here by a mechanistic one based on the optimized exchange of CO_2 and water by plants (Katul et al., 2009). Furthermore, a larger set of land cover types is expected to improve the vegetation-dependent variation of dry deposition. The parameters used to model dry deposition of stomata, cuticle and soil are biome dependent and using generalized ones like for the input cuticular resistance can lead to differences in dry deposition (Hoshika et al., 2018). Exemplary discrepancies for the stomatal conductance calculated with different parameter sets are shown in Fig. 13 as the summer mean of 2010. Thereby, the temperature stress factor has been calculated as in Eq. (6) using the obtained surface temperature by EMAC (Fig. 13a, c) and applied to the model (DEFAULT) stomatal conductance (Eq. 17) with two different parameter sets for coniferous and mixed forest by Simpson et al. (2012)[3] and Zhang et al. (2003)[4]. Jarvis (1976) obtained the parameters from a set of measurements in mixed hardwood/coniferous forest in Washington. In general, the parameters are related to measurements where the absolute values are influenced by multiple factors like genotype and local climatic conditions (Sulis et al., 2015; Tuovinen et al., 2009; Hoshika et al., 2018). So, for global modelling, mostly simplified parameters have to be used like in the European Monitoring and Evaluation Programme (EMEP) (Simpson et al., 2012).

7 Sensitivity to model resolution

The simulation of dry deposition depends on meteorology including boundary layer processes, radiation (cloud distribution and reflectivity) and ozone chemistry as well as on input fields like vegetation density (LAI) (Jones, 1992). Model horizontal resolution inherently affects the amplitude and distribution of (regridded) surface processes and the artificial dilution of ozone precursors that are emitted. This aspect is investigated here by analysing simulations at three different spatial resolutions: $2.8° \times 2.8°$, $1.9° \times 1.9°$ and $1.1° \times 1.1°$ (REST42, REST63, and REV (T106) in Table 1).

In Fig. 14a, the resolution dependency is shown for the annual dry deposition flux of ozone on different continental regions. The annual dry deposition fluxes differ by up to $40\,\mathrm{Tg\,yr^{-1}}$ globally between the different resolutions, with highest dry deposition at high resolution (T106). For the Northern Hemisphere (and consequently globally), this difference is driven by the higher annual mean ground-level ozone compared to the lower resolutions (Fig. 14c). However, this effect cannot be disentangled from the effect of decreased dry deposition velocity on ground-level ozone. Globally, increasing differences in O_3 are anti-correlated with relative humidity as shown in Fig. 15a ($\rho = -0.8$). The impact of humidity on ozone chemistry is considered to be relatively weak (Jacob and Winner, 2009), but Kavassalis and Murphy (2017) showed for the US that only dry deposition establishes the observed anti-correlation between ozone and relative humidity. A dominating positive correlation of the dry deposition flux with the velocity only occurs on the Southern Hemisphere extratropics (SH_exT), which is highest between T63 and T106 (Fig. 15c). This can be attributed to discrepancies in stomatal deposition (Fig. 15d) driven by differences in humidity which might be caused by different moisture cycles and transpiration.

8 Conclusion and recommendations

Dry deposition to the Earth's surface is a key process for the representation of ground-level ozone in global models. Its parameterizations constitutes a relevant part of the model uncertainty (Hardacre et al., 2015; Wu et al., 2018). Revising the dry deposition scheme of EMAC leads to an improved representation of surface ozone in regions with a positive model ozone bias (e.g. Europe). The highest increase in ozone dry deposition is due to the implementation of cuticular uptake whose contribution is important especially during night over moist surfaces. The extension of the stomatal uptake with temperature and VPD adjustment factors accounts for the desired link of plant activity to hydroclimate

[3]Used parameters: $T_{min} = 0\,°C$, $T_{opt} = 18\,°C$, $T_{max} = 36\,°C$.
[4]Used parameters: $T_{min} = -3\,°C$, $T_{opt} = 21\,°C$, $T_{max} = 42\,°C$.

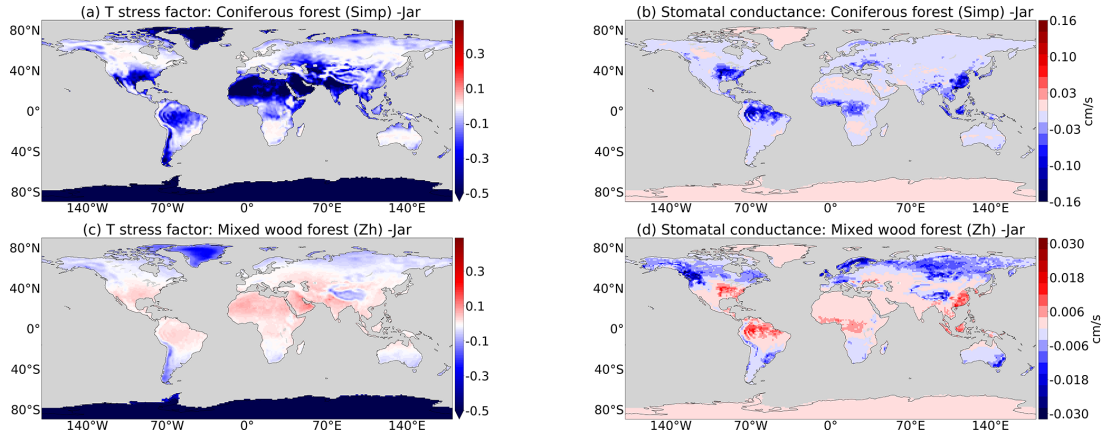

Figure 13. Absolute difference of stomatal conductance applied with the temperature stress factor calculated for two different parameter sets by Simpson et al. (2012) (Simp) and Zhang et al. (2003) (Zh) in a comparison with the here-used parameter set by Jarvis (1976) (Jar).

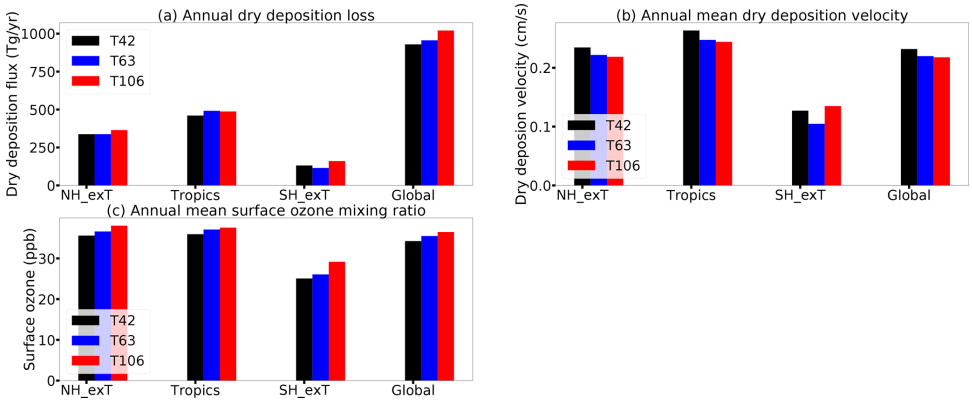

Figure 14. Ozone and dry deposition at three different resolutions (T42: 2.8° × 2.8°, T63: 1.9° × 1.9°, T106: 1.1° × 1.1°) and the different regions: Northern Hemisphere extratropics (NH_exT: 90–30° N), tropics (30° N–30° S), Southern Hemisphere extratropics (SH_exT: 90–30° S) and the whole Earth (global).

as recommended by Lin et al. (2019). Especially in drought-stressed regions (e.g. citrus orchards), the dependence on vapour pressure deficit leads to a realistic depression of stomatal uptake at noon. Also the dependence of dry deposition on soil moisture has been modified since the current representation of soil moisture in the model is not satisfactory. Specifically, the model simulates a too-dry soil for the Amazon basin, causing stomatal closure and thus an underestimation of dry deposition (Sect. 4.2). We have indications that the dry bias is a consequence of meteorological nudging in EMAC and also the missing representation of organized convection in the tropics (Mauritsen and Stevens, 2015). The sensitivity of the vegetation to droughts is comparably high in the Amazon region because the model soil cannot hold water in the catchment for a realistic time period and exhibits a memory effect (Hagemann and Stacke, 2013). Deeper root zones or buffering of the soil moisture below the root zone would improve the water holding capacity (Hagemann and Stacke, 2013; Fisher et al., 2007). With an improved representation of soil moisture, the more realistic parameterization of the soil moisture stress on stomatal uptake could be re-enabled. In general, the inclusion of the strong link between dry deposition and meteorology reveals some limitations of the dry deposition scheme associated with the inaccurate representation of local meteorology. The results also indicate that an improved representation of important non-stomatal dry deposition like in-canopy reactions of ozone with volatile organic compounds (e.g. citrus orchards; Sect. 4.2) would lower the positive model–observation discrepancy. This can be achieved with the inclusion of further BVOCs and an

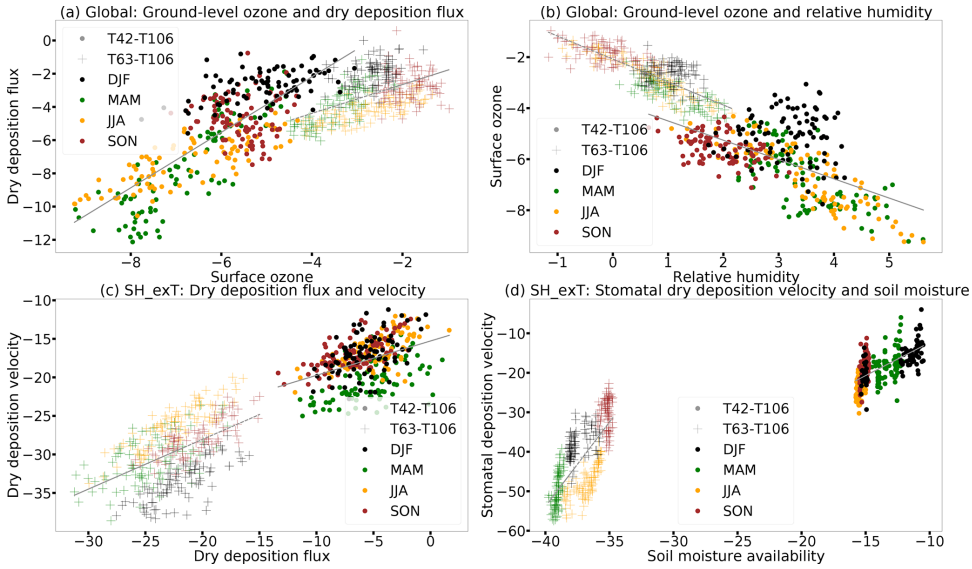

Figure 15. Correlations of resolution dependent relative differences of ozone, dry deposition and meteorological variables for the whole Earth (global) and the Southern Hemisphere extratropics (SH_exT) for the four boreal seasons: spring (MAM), summer (JJA), autumn (SON) and winter (DJF).

explicit parameterization of the transport dynamics in the boundary layer in model simulations (Makar et al., 2017). Explicit field measurements could foster further process understanding, which is required for a detailed process description within the models, especially over tropical rainforests. The seasonal variability of the simulated dry deposition velocity could be further improved by using as model input the time series of vegetation cover from imaging products which also capture land use changes and vegetation trend that are known to impact dry deposition significantly (Wong et al., 2019).

9 Outlook

The representation of gaseous dry deposition in MESSy will be further improved by using the MODIS time series of LAI which captures multi-annual vegetation changes. As the next step of dry deposition modelling in MESSy, a biome-dependent dry deposition model coupled to CO_2 assimilation (White et al., 2004) will be applied. Biome-dependent vegetation cover information, required for this scheme, is then provided by global input data which, however, represent only the annual cycle of vegetation. Coupling MESSy to the recently available dynamic vegetation model LPJ-GUESS, which provides detailed vegetation information with the temporal variability required for a climate model, could be a further improvement. By now, the one-way coupling of LPJ-GUESS as a MESSy submodel is only in the initial evaluation phase of the coupling with the atmospheric model (Forrest et al., 2020).

Appendix A: Default dry deposition scheme

The default dry deposition scheme of MESSy uses the following equations described in Kerkweg et al. (2006).

For surface resistance over vegetation (in $\mathrm{s\,m^{-1}}$),

$$\frac{1}{R_{\mathrm{s,veg}}(X)} = \frac{1}{R_{\mathrm{can}} + R_{\mathrm{s,soil}}(X) + R_{\mathrm{qbr,veg}}(X)} + \frac{\mathrm{LAI}}{r_{\mathrm{cut}}(X)} + \frac{LAI}{r_{\mathrm{stom,corr}}(X) + r_{\mathrm{mes}}(X)}, \tag{A1}$$

where $R_{\mathrm{can}}(X)$, $R_{\mathrm{s,soil}}(X)$ and $R_{\mathrm{qbr,veg}}(X)$ are the in-canopy aerodynamic resistance, the soil resistance and the quasi-laminar boundary resistance at canopy scale (in $\mathrm{s\,m^{-1}}$). $r_{\mathrm{cut}}(X)$, $r_{\mathrm{stom,corr}}(X)$ and $r_{\mathrm{mes}}(X)$ are the cuticular resistance, stomatal resistance and mesophyll resistance at leaf scale scaled with LAI (in $\mathrm{m^2\ m^{-2}}$) to canopy scale.
For stomatal resistance,

$$r_{\mathrm{stom,corr}} = \frac{r_{\mathrm{stom}}(\mathrm{PAR})}{\mathrm{fws}} \cdot \frac{D_{\mathrm{H_2O}}}{D(\mathrm{O_3})}. \tag{A2}$$

For soil moisture stress function,

$$f(W_{\mathrm{s}}) = \begin{cases} 1 & W_{\mathrm{s}}(t) \geq W_{\mathrm{cr}}(=75\,\%) \\ \frac{W_{\mathrm{s}}(t) - W_{\mathrm{pwp}}}{W_{\mathrm{cr}} - W_{\mathrm{pwp}}} & W_{\mathrm{pwp}} < W_{\mathrm{s}}(t) < W_{\mathrm{cr}} \\ 0 & W_{\mathrm{s}}(t) \leq W_{\mathrm{pwp}}(=35\,\%). \end{cases} \tag{A3}$$

For cuticular resistance,

$$r_{\mathrm{cut}}(X) = \frac{r_{\mathrm{cut}}(\mathrm{O_3})}{10^{-5} \cdot H(\mathrm{O_3}) + s_{\mathrm{reac}}(\mathrm{O_3})}, \tag{A4}$$

where $r_{\mathrm{cut}}\mathrm{O_3} = 1 \times 10^{-5}\,\mathrm{s\,m^{-1}}$, $H(\mathrm{O_3}) = 0.01$ and $s_{\mathrm{reac}} = 1$.
For wet skin resistance,

$$R_{\mathrm{ws}}(\mathrm{O_3}) = \left[\frac{1/3}{R_{\mathrm{ws}}(\mathrm{SO_2})} + 10^{-7} \cdot H(\mathrm{O_3}) + \frac{s_{\mathrm{reac}}(\mathrm{O_3})}{R_{\mathrm{cut,w}}(\mathrm{O_3})} \right]^{-1}, \tag{A5}$$

where $R_{\mathrm{ws}}(\mathrm{O_3}) = 2000\,\mathrm{s\,m^{-1}}$ and $R_{\mathrm{ws}}(\mathrm{SO_2}) = 100\,\mathrm{s\,m^{-1}}$.

Appendix B: Evapotranspiration

Plants play a key role in the water and energy cycle and thus contribute to the land–atmosphere coupling, which drives the global climate. In this context, transpiration is an important process, as plants lose water during the necessary CO_2 uptake via their stomata. The amount depends on the aperture behaviour of the respective plant in the respective environmental conditions (Katul et al., 2012). Thus, the latent heat flux incorporates the canopy resistance. The formulation is based on the Monin–Obukhov stability theory:

$$E = \rho C_{\mathrm{h}} |\boldsymbol{v}| \beta (q_{\mathrm{a}} - h q_{\mathrm{s}}(T_{\mathrm{s}}, p_{\mathrm{s}}))$$
$$\beta = \left[1 + \frac{C_{\mathrm{h}} |\boldsymbol{v}| R_{\mathrm{stom}}}{\mathrm{fws}} \right]^{-1}, \tag{B1}$$

where ρ is the density of air, $|\boldsymbol{v}|$ is the absolute value of the horizontal wind speed and C_{h} is the transfer coefficient of heat, whereas $r_a = 1/(C_{\mathrm{h}}|\boldsymbol{v}|)$. q_{s} and q_a are the saturation-specific humidity and the atmospheric specific humidity, whereas the relative humidity h at the surface limits the evapotranspiration from bare soil. β determines the ratio of transpiration between water-stressed plants ($\beta < 1$) and well-watered plants ($\beta = 1$) (Giorgetta et al., 2013; Schulz et al., 2001). The formula for the canopy stomatal resistance R_{stom} is given in Eq. (5). In order to adapt the transpiration to temperature and vapour pressure deficit, the T and VPD adjustment factors can be applied to R_{stom} inversely like in the new dry deposition scheme via izwet = 1 in the VERTEX *&CTRL* namelist. The modification of the soil moisture stress function $f(W_{\mathrm{s}})$ (old: Eq. A3; new: Eq. 12) affects evapotranspiration directly.

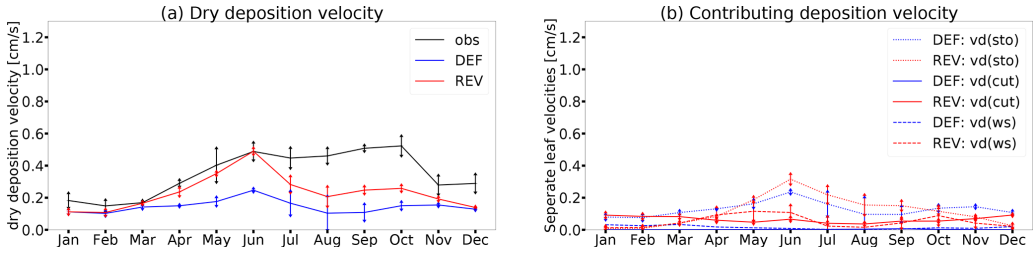

Figure B1. Measured and modelled (DEF, REV) annual cycles at Borden forest.

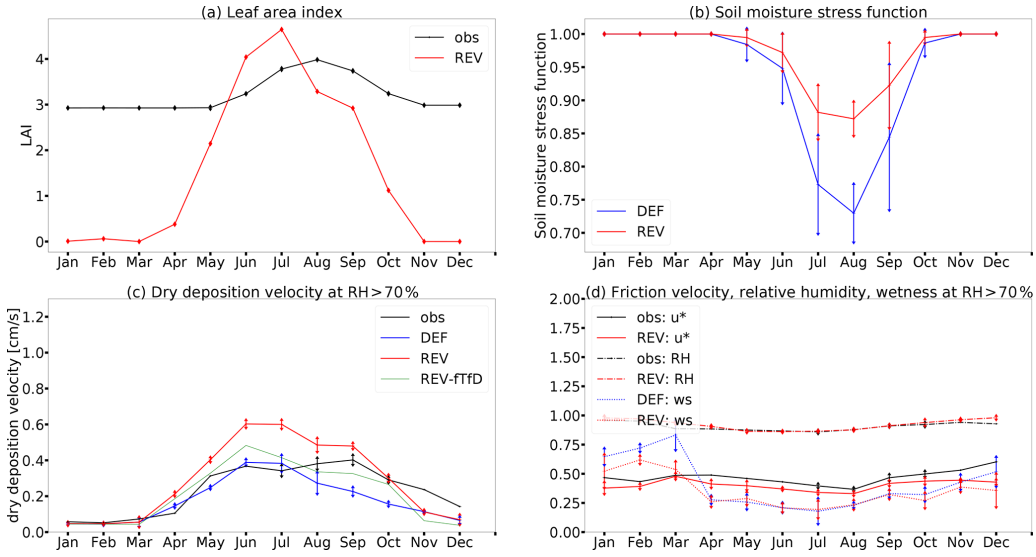

Figure B2. Measured (obs) and modelled (DEF, REV) multiyear (2010–2012) and REV-fTfD (2010) annual cycles at Hyytiälä.

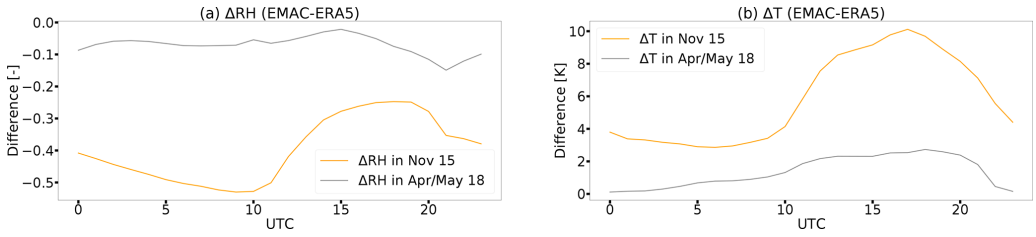

Figure B3. Differences of meteorology between EMAC and ERA5 at ATTO.

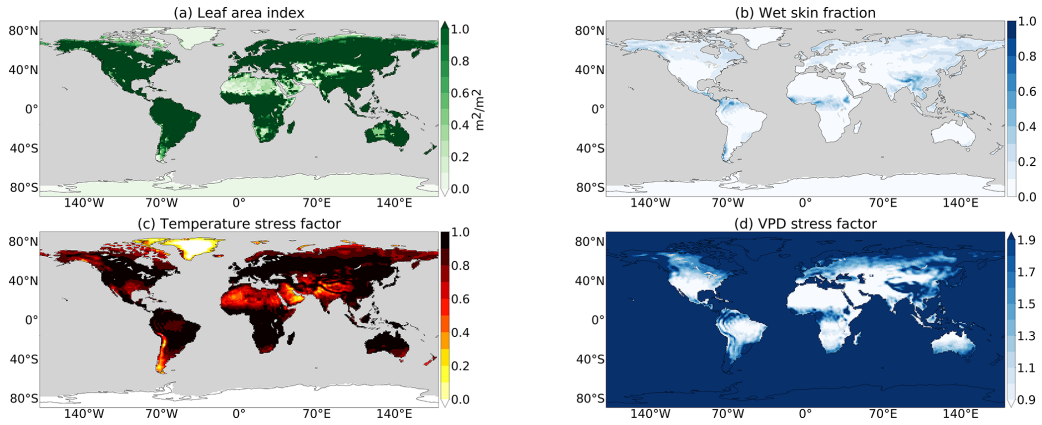

Figure B4. Boreal summer mean vegetation and meteorological variables predicted by EMAC.

Code availability. The Modular Earth Submodel System (MESSy) is continuously further developed and applied by a consortium of institutions. The usage of MESSy and access to the source code is licensed to all affiliates of institutions which are members of the MESSy Consortium. Institutions can become a member of the MESSy Consortium by signing the MESSy Memorandum of Understanding. More information can be found on the MESSy Consortium Website http://www.messy-interface.org (last access: 17 August 2020). The code presented here has been based on MESSy version 2.54 and will be available in the next official release (version 2.55). The exact code version used to produce the results of this paper is archived in the MESSy code repository and can be made available to members of the MESSy community upon request.

Data availability. The measurement data from Ontario are freely available at http://data.ec.gc.ca/data/air/monitor/special-studies-of-atmospheric-gases-particles-and-precipitation-chemistry/borden-forest-ozone-and-sulphur-dioxide-dry-deposition-study (Wu et al., 2016) with the "Open Government Licence-Canada" (https://open.canada.ca/en/open-government-licence-canada, last access: 14 November 2019). The measurement data from Hyytiälä (Creative Commons 4.0 Attribution (CC BY) license https://creativecommons.org/licenses/by/4.0/, last access: 5 May 2020) can be accessed at https://avaa.tdata.fi/web/smart/smear/download (Mammarella et al., 2020). The data from Lindcove station (Fares et al., 2012–2014) were provided by Silvano Fares (Fares et al., 2012). The dry deposition measurement data from the Amazon Tall Tower Observatory were provided by Matthias Sörgel and are available upon request. The used ERA5 global climate reanalysis by ECMWF is available through the Climate Data Store (https://cds.climate.copernicus.eu, Copernicus, 2017).

Supplement. The supplement related to this article is available online at: https://doi.org/10.5194/gmd-14-495-2021-supplement.

Author contributions. DT (and AK) initiated and supervised the study. DT and TE discussed the model developments which were implemented by AK and TE. HO originally wrote the MESSy VERTEX vertical diffusion submodel. SF provided the measurement data from Lindcove and further related theoretical calculations. IM conducted the dry deposition measurements at Hyytiälä and gave related support. TE performed the EMAC simulations and the data analyses, prepared the figures and wrote the manuscript.

Competing interests. The authors declare that they have no conflict of interest.

Acknowledgements. The work described in this paper has received funding from the Initiative and Networking Fund of the Helmholtz Association through the project "Advanced Earth System Modelling Capacity (ESM)". The content of this paper is the sole responsibility of the author(s) and it does not represent the opinion of the Helmholtz Association, and the Helmholtz Association is not responsible for any use that might be made of the information contained. The author(s) acknowledge the Environment and Climate Change Canada and the United States Environmental Protection Agency for the provision of the dry deposition velocity data at the Borden forest research station. Moreover, the personnel at the SMEAR II station of INAR – Institute for Atmospheric and Earth System Research, University of Helsinki, Finland, is acknowledged. Concerning the measurement data from Amazon Tall Tower, we thank the Instituto Nacional de Pesquisas da Amazônia (INPA) and the Max Planck Society for continuous support. We thank for the support by the German Federal Ministry of Education and Research (BMBF contracts 01LB1001A, 01LK1602B and 01LP1606B) and the Brazilian Ministério da Ciência, Tecnologia e Inovação (MCTI/FINEP contract 01.11.01248.00) as well as the Amazon State University (UEA), FAPEAM, LBA/INPA and SDS/CEUC/RDS-Uatumã. The measurements were conducted by Matthias Sörgel, Anywhere Tsokankunku, Stefan Wolff and Rodrigo Souza. For the usage of data from the ERA5 global climate reanalysis (generated using Copernicus Atmosphere Monitoring Service Information, 2020), we acknowledge the Copernicus Climate Change and Atmosphere Monitoring Service (https://apps.ecmwf.int/datasets/licences/copernicus/, last access: 10 March 2020). Neither the European Commission nor ECMWF is responsible for any use that may be made of the Copernicus information or data it contains.

Financial support. The article processing charges for this open-access publication were covered by a Research Centre of the Helmholtz Association.

Review statement. This paper was edited by Jason Williams and reviewed by Dennis Baldocchi and two anonymous referees.

References

Altimir, N., Kolari, P., Tuovinen, J.-P., Vesala, T., Bäck, J., Suni, T., Kulmala, M., and Hari, P.: Foliage surface ozone deposition: a role for surface moisture?, Biogeosciences, 3, 209–228, https://doi.org/10.5194/bg-3-209-2006, 2006.

Andersson, C. and Engardt, M.: European ozone in a future climate: Importance of changes in dry deposition and isoprene emissions, J. Geophys. Res.-Atmos., 115, D02303, https://doi.org/10.1029/2008JD011690, 2010.

Baldocchi, D. D., Hicks, B. B., and Camara, P.: A canopy stomatal resistance model for gaseous deposition to vegetated surfaces, Atmos. Environ., 21, 91–101, 1987.

Ball, J. T., Woodrow, I. E., and Berry, J. A.: A model predicting stomatal conductance and its contribution to the control of photosynthesis under different environmental conditions, in: Progress in photosynthesis research, Springer, Dordrecht, 221–224, 1987.

Bourtsoukidis, E., Behrendt, T., Yañez-Serrano, A. M., Hellén, H., Diamantopoulos, E., Catão, E., Ashworth, K., Pozzer, A., Quesada, C., Martins, D., Sá, M., Araujo, A., Brito, J., Artaxo, P., Kesselmeier, J., Lelieveld, J., and Williams, J.: Strong sesquiterpene emissions from Amazonian soils, Nat. Commun., 9, 1–11, https://doi.org/10.1038/s41467-018-04658-y, 2018.

Clifton, O., Paulot, F., Fiore, A., Horowitz, L., Correa, G., Baublitz, C., Fares, S., Goded, I., Goldstein, A., Gruening, C., Hogg, A. J., Loubet, B., Mammarella, I., Munger, J. W., Neil, L., Stella, P., Uddling, J., Vesala, T., and Weng, E.: Influence of dynamic ozone dry deposition on ozone pollution, J. Geophys. Res.-Atmos., 125, e2020JD032398, https://doi.org/10.1029/2020JD032398, 2020a.

Clifton, O. E., Fiore, A. M., Munger, J., Malyshev, S., Horowitz, L., Shevliakova, E., Paulot, F., Murray, L., and Griffin, K.: Interannual variability in ozone removal by a temperate deciduous forest, Geophys. Res. Lett., 44, 542–552, https://doi.org/10.1002/2016GL070923, 2017.

Clifton, O. E., Fiore, A. M., Massman, W. J., Baublitz, C. B., Coyle, M., Emberson, L., Fares, S., Farmer, D. K., Gentine, P., Gerosa, G., Guenther, A. B., Helmig, D., Lombardozzi, D. L., Munger, J. W., Patton, E. G., Pusede, S. E., Schwede, D. B., Silva, S. J., Sörgel, M., Steiner, S. L., and Tai, A. P. K.: Dry deposition of ozone over land: processes, measurement, and modeling, Rev. Geophys., 58, e2019RG000670, https://doi.org/10.1029/2019RG000670, 2020b.

Collatz, G. J., Ribas-Carbo, M., and Berry, J.: Coupled photosynthesis-stomatal conductance model for leaves of C4 plants, Funct. Plant Biol., 19, 519–538, 1992.

Combe, M., de Arellano, J. V.-G., Ouwersloot, H. G., and Peters, W.: Plant water-stress parameterization determines the strength of land–atmosphere coupling, Agr. Forest Meteorol., 217, 61–73, https://doi.org/10.1016/j.agrformet.2015.11.006, 2016.

Copernicus: ERA5: Fifth generation of ECMWF atmospheric reanalyses of the global climate, https://doi.org/10.24381/cds.adbb2d47, available at: https://cds.climate.copernicus.eu/cdsapp#!/home (last access: 8 April 2020), 2017.

Coumou, D. and Rahmstorf, S.: A decade of weather extremes, Nature Clim. Change, 2, 491, https://doi.org/10.1038/NCLIMATE1452, 2012.

Cowan, I. and Farquhar, G.: Stomatal function in relation to leaf metabolism and environment, Symp. Soc. Exp. Biol., 31, 471–505, 1977.

Damour, G., Simonneau, T., Cochard, H., and Urban, L.: An overview of models of stomatal conductance at the leaf level, Plant Cell Environ., 33, 1419–1438, https://doi.org/10.1111/j.1365-3040.2010.02181.x, 2010.

Deckert, R., Jöckel, P., Grewe, V., Gottschaldt, K.-D., and Hoor, P.: A quasi chemistry-transport model mode for EMAC, Geosci. Model Dev., 4, 195–206, https://doi.org/10.5194/gmd-4-195-2011, 2011.

Delworth, T. L. and Manabe, S.: The influence of potential evaporation on the variabilities of simulated soil wetness and climate, J. Climate, 1, 523–547, 1988.

Emberson, L., Ashmore, M., Cambridge, H., Simpson, D., and Tuovinen, J.-P.: Modelling stomatal ozone flux across Europe, Environ. Pollut., 109, 403–413, 2000.

Fares, S., Savi, F., and Conte, A.: Measurement data at Lindcove Orange Orchard, FLUXNET2015 IT-Cp2 Castelporziano2, Dataset, https://doi.org/10.18140/FLX/1440233, 2012–2014.

Fares, S., Weber, R., Park, J.-H., Gentner, D., Karlik, J., and Goldstein, A. H.: Ozone deposition to an orange orchard: Partitioning between stomatal and non-stomatal sinks, Environ. Pollut., 169, 258–266, https://doi.org/10.1016/j.envpol.2012.01.030, 2012.

Fares, S., Matteucci, G., Mugnozza, G. S., Morani, A., Calfapietra, C., Salvatori, E., Fusaro, L., Manes, F., and Loreto, F.: Testing of models of stomatal ozone fluxes with field measurements in a mixed Mediterranean forest, Atmos. Environ., 67, 242–251, https://doi.org/10.1016/j.atmosenv.2012.11.007, 2013.

Fisher, R., Williams, M., Da Costa, A. L., Malhi, Y., Da Costa, R., Almeida, S., and Meir, P.: The response of an Eastern Amazonian rain forest to drought stress: results and modelling analyses from a throughfall exclusion experiment, Glob. Change Biol., 13, 2361–2378, https://doi.org/10.1111/j.1365-2486.2007.01417.x, 2007.

Freire, L., Gerken, T., Ruiz-Plancarte, J., Wei, D., Fuentes, J., Katul, G., Dias, N., Acevedo, O., and Chamecki, M.: Turbulent mixing and removal of ozone within an Amazon rainforest canopy, J. Geophys. Res.-Atmos., 122, 2791–2811, https://doi.org/10.1002/2016JD026009, 2017.

Ganzeveld, L. and Lelieveld, J.: Dry deposition parameterization in a chemistry general circulation model and its influence on the distribution of reactive trace gases, J. Geophys. Res.-Atmos., 100, 20999–21012, 1995.

Ganzeveld, L., Lelieveld, J., and Roelofs, G.-J.: A dry deposition parameterization for sulfur oxides in a chemistry and general circulation model, J. Geophys. Res.-Atmos., 103, 5679–5694, 1998.

Ganzeveld, L., Lelieveld, J., Dentener, F., Krol, M., Bouwman, A., and Roelofs, G.-J.: Global soil-biogenic NOx emissions and the role of canopy processes, J. Geophys. Res.-Atmos., 107, 4298, https://doi.org/10.1029/2001JD0012892002, 2002.

Giorgetta, M. A., Roeckner, E., Mauritsen, T., Bader, J., Crueger, T., Esch, M., Rast, S., Kornblueh, L., Schmidt, H., Kinne, S., Hohenegger, C., Möbis, B., Krismer, T., Wieners, K.-H., and Stevens, B.: The atmospheric general circulation model ECHAM6-model description, Reports on Earth System Science, No.135, Max-Planck-Institut für Meteorologie, Hamburg, 2013.

Hagemann, S. and Stacke, T.: Impact of the soil hydrology scheme on simulated soil moisture memory in a GCM, Clim. Dynam., 44.7, 1731–1750, https://doi.org/10.1007/s00382-014-2221-6, 2013.

Hardacre, C., Wild, O., and Emberson, L.: An evaluation of ozone dry deposition in global scale chemistry climate models, Atmos. Chem. Phys., 15, 6419–6436, https://doi.org/10.5194/acp-15-6419-2015, 2015.

Hogg, A., Uddling, J., Ellsworth, D., Carroll, M. A., Pressley, S., Lamb, B., and Vogel, C.: Stomatal and non-stomatal fluxes of ozone to a northern mixed hardwood forest, Tellus B, 59, 514–525, https://doi.org/10.1111/j.1600-0889.2007.00269.x, 2007.

Hoshika, Y., Osada, Y., De Marco, A., Penuelas, J., and Paoletti, E.: Global diurnal and nocturnal parameters of stomatal conductance in woody plants and major crops, Global Ecol. Biogeogr., 27, 257–275, https://doi.org/10.1016/j.agrformet.2017.01.005, 2018.

Hu, L., Jacob, D. J., Liu, X., Zhang, Y., Zhang, L., Kim, P. S., Sulprizio, M. P., and Yantosca, R. M.: Global budget of tropospheric ozone: Evaluating recent model advances with satellite (OMI), aircraft (IAGOS), and ozonesonde observations, Atmos. Environ., 167, 323–334, https://doi.org/10.1016/j.atmosenv.2017.08.036, 2017.

Huang, L., McDonald-Buller, E. C., McGaughey, G., Kimura, Y., and Allen, D. T.: The impact of drought on ozone dry de-

position over eastern Texas, Atmos. Environ., 127, 176–186, https://doi.org/10.1016/j.atmosenv.2015.12.022, 2016.

Jacob, D. J. and Winner, D. A.: Effect of climate change on air quality, Atmos. Environ., 43, 51–63, https://doi.org/10.1016/j.atmosenv.2008.09.051, 2009.

Jarvis, P.: The interpretation of the variations in leaf water potential and stomatal conductance found in canopies in the field, Phil. Trans. R. Soc. Lond. B, 273, 593–610, 1976.

Jeuken, A. B. M., Siegmund, P. C., Heijboer, L. C., Feichter, J., and Bengtsson, L.: On the potential of assimilating meteorological analyses in a global climate model for the purpose of model validation, J. Geophys. Res.-Atmos., 101, 16939–16950, https://doi.org/10.1029/96JD01218, 1996.

Jöckel, P., Kerkweg, A., Pozzer, A., Sander, R., Tost, H., Riede, H., Baumgaertner, A., Gromov, S., and Kern, B.: Development cycle 2 of the Modular Earth Submodel System (MESSy2), Geosci. Model Dev., 3, 717–752, https://doi.org/10.5194/gmd-3-717-2010, 2010.

Jöckel, P., Tost, H., Pozzer, A., Kunze, M., Kirner, O., Brenninkmeijer, C. A. M., Brinkop, S., Cai, D. S., Dyroff, C., Eckstein, J., Frank, F., Garny, H., Gottschaldt, K.-D., Graf, P., Grewe, V., Kerkweg, A., Kern, B., Matthes, S., Mertens, M., Meul, S., Neumaier, M., Nützel, M., Oberländer-Hayn, S., Ruhnke, R., Runde, T., Sander, R., Scharffe, D., and Zahn, A.: Earth System Chemistry integrated Modelling (ESCiMo) with the Modular Earth Submodel System (MESSy) version 2.51, Geosci. Model Dev., 9, 1153–1200, https://doi.org/10.5194/gmd-9-1153-2016, 2016.

Jones, H.: Plants and Microclimate, Cambridge University Press, Cambridge, 1992.

Jülich Supercomputing Centre: JURECA: Modular supercomputer at Jülich Supercomputing Centre, J. Large-Scale Res. Facilities, 4, p. 132, https://doi.org/10.17815/jlsrf-4-121-1, 2018.

Katul, G. G., Palmroth, S., and Oren, R.: Leaf stomatal responses to vapour pressure deficit under current and CO_2-enriched atmosphere explained by the economics of gas exchange, Plant Cell Environ., 32, 968–979, https://doi.org/10.1111/j.1365-3040.2009.01977.x, 2009.

Katul, G. G., Oren, R., Manzoni, S., Higgins, C., and Parlange, M. B.: Evapotranspiration: a process driving mass transport and energy exchange in the soil-plant-atmosphere-climate system, Rev. Geophys., 50, RG3002, https://doi.org/10.1029/2011RG000366, 2012.

Kavassalis, S. C. and Murphy, J. G.: Understanding ozone-meteorology correlations: A role for dry deposition, Geophys. Res. Lett., 44, 2922–2931, https://doi.org/10.1002/2016GL071791, 2017.

Kerkweg, A., Buchholz, J., Ganzeveld, L., Pozzer, A., Tost, H., and Jöckel, P.: Technical Note: An implementation of the dry removal processes DRY DEPosition and SEDImentation in the Modular Earth Submodel System (MESSy), Atmos. Chem. Phys., 6, 4617–4632, https://doi.org/10.5194/acp-6-4617-2006, 2006.

Keronen, P., Reissell, A., Rannik, U., Pohja, T., Siivola, E., Hiltunen, V., Hari, P., Kulmala, M., and Vesala, T.: Ozone flux measurements over a Scots pine forest using eddy covariance method: performance evaluation and comparison with flux-profile method, Boreal Environ. Res., 8, 425–444, 2003.

Kharol, S., Shephard, M., McLinden, C., Zhang, L., Sioris, C., O'Brien, J., Vet, R., Cady-Pereira, K., Hare, E., Siemons, J., and Krotkov, N. A.: Dry deposition of reactive nitrogen from satellite observations of ammonia and nitrogen dioxide over North America, Geophys. Res. Lett., 45, 1157–1166, https://doi.org/10.1002/2017GL075832, 2018.

Klimarechenzentrum: The ECHAM3 atmospheric general circulation model, Deutsches Klimarechenzentrum, Hamburg, Techn. Rep, 6, 1992.

Kraus, H.: Die Atmosphäre der Erde: Eine Einführung in die Meteorologie, Springer-Verlag, Berlin, Heidelberg, 2007 (in German).

Lamaud, E., Carrara, A., Brunet, Y., Lopez, A., and Druilhet, A.: Ozone fluxes above and within a pine forest canopy in dry and wet conditions, Atmos. Environ., 36, 77–88, 2002.

Lamaud, E., Loubet, B., Irvine, M., Stella, P., Personne, E., and Cellier, P.: Partitioning of ozone deposition over a developed maize crop between stomatal and non-stomatal uptakes, using eddy-covariance flux measurements and modelling, Agr. Forest Meteorol., 149, 1385–1396, https://doi.org/10.1016/j.agrformet.2009.03.017, 2009.

Lin, M., Malyshev, S., Shevliakova, E., Paulot, F., Horowitz, L. W., Fares, S., Mikkelsen, T. N., and Zhang, L.: Sensitivity of ozone dry deposition to ecosystem-atmosphere interactions: A critical appraisal of observations and simulations, Global Biogeochem. Cy., 33, 1264–1288, https://doi.org/10.1029/2018GB006157, 2019.

Lu, Y.-S.: Propagation of land surface model uncertainties in simulated terrestrial system states, PhD thesis, Bonner Meteorologische Abhandlungen Heft 84, University of Bonn, Germany, 120 pp., 2018.

Makar, P., Staebler, R., Akingunola, A., Zhang, J., McLinden, C., Kharol, S., Pabla, B., Cheung, P., and Zheng, Q.: The effects of forest canopy shading and turbulence on boundary layer ozone, Nat. Commun., 8, 15243, https://doi.org/10.1038/ncomms15243, 2017.

Mammarella, I., Rannik, Ü., and Launiainen, S.: SMEAR II Hyytiälä forest eddy covariance, Institute for Atmospheric and Earth System Research, available at: https://avaa.tdata.fi/web/smart/smear/download, last access: 12 June 2020.

Mauritsen, T. and Stevens, B.: Missing iris effect as a possible cause of mutedhydrological change and high climate sensitivity in models, Nat, Geosci., 8, 346–351, https://doi.org/10.1038/NGEO2414, 2015.

Mauritsen, T., Stevens, B., Roeckner, E., Crueger, T., Esch, M., Giorgetta, M., Haak, H., Jungclaus, J., Klocke, D., Matei, D., Mikolajewicz, U., Notz, D., Pincus, R., Schmidt, H., and Tomassini, L.: Tuning the climate of a global model, J. Adv. Model. Earth Sy., 4, M00A01, https://doi.org/10.1029/2012MS000154, 2012.

Mészáros, R., Horváth, L., Weidinger, T., Neftel, A., Nemitz, E., Dämmgen, U., Cellier, P., and Loubet, B.: Measurement and modelling ozone fluxes over a cut and fertilized grassland, Biogeosciences, 6, 1987–1999, https://doi.org/10.5194/bg-6-1987-2009, 2009.

National Centers for Environmental Information: State of the Climate: Global Climate Report for Annual 2015, Tech. rep., available at: https://www.ncdc.noaa.gov/sotc/global/201513 (last access: 3 March 2020), 2016.

Ran, L., Pleim, J., Song, C., Band, L., Walker, J. T., and Binkowski, F. S.: A photosynthesis-based two-leaf canopy stomatal conductance model for meteorology and air quality modeling with

WRF/CMAQ PX LSM, J. Geophys. Res.-Atmos., 122, 1930–1952, https://doi.org/10.1002/2016JD025583, 2017.

Rannik, Ü., Altimir, N., Mammarella, I., Bäck, J., Rinne, J., Ruuskanen, T. M., Hari, P., Vesala, T., and Kulmala, M.: Ozone deposition into a boreal forest over a decade of observations: evaluating deposition partitioning and driving variables, Atmos. Chem. Phys., 12, 12165–12182, https://doi.org/10.5194/acp-12-12165-2012, 2012.

Rannik, Ü., Peltola, O., and Mammarella, I.: Random uncertainties of flux measurements by the eddy covariance technique, Atmos. Meas. Tech., 9, 5163–5181, https://doi.org/10.5194/amt-9-5163-2016, 2016.

Righi, M., Eyring, V., Gottschaldt, K.-D., Klinger, C., Frank, F., Jöckel, P., and Cionni, I.: Quantitative evaluation of ozone and selected climate parameters in a set of EMAC simulations, Geosci. Model Dev., 8, 733–768, https://doi.org/10.5194/gmd-8-733-2015, 2015.

Roeckner, E., Bäuml, G., Bonaventura, L., Brokopf, R., Esch, M., Giorgetta, M., Hagemann, S., Kirchner, I., Kornblueh, L., Manzini, E., Rhodin, A., Schlese, U., Schulzweida, U., and Tompkins, A.: The atmospheric general circulation model ECHAM 5. PART I: Model description, report no. 349, Max Planck Institute for Meteorology, Hamburg, 2003.

Rummel, U., Ammann, C., Kirkman, G. A., Moura, M. A. L., Foken, T., Andreae, M. O., and Meixner, F. X.: Seasonal variation of ozone deposition to a tropical rain forest in southwest Amazonia, Atmos. Chem. Phys., 7, 5415–5435, https://doi.org/10.5194/acp-7-5415-2007, 2007.

Schulz, J.-P., Dümenil, L., and Polcher, J.: On the land surface–atmosphere coupling and its impact in a single-column atmospheric model, J. Appl. Meteorol., 40, 642–663, 2001.

Schwede, D., Zhang, L., Vet, R., and Lear, G.: An intercomparison of the deposition models used in the CASTNET and CAPMoN networks, Atmos. Environ., 45, 1337–1346, 2011.

Seinfeld, J. H. and Pandis, S. N.: Atmospheric chemistry and physics: from air pollution to climate change, John Wiley & Sons, Hoboken, NJ, 2016.

Sellers, P., Mintz, Y., Sud, Y. E. A., and Dalcher, A.: A simple biosphere model (SiB) for use within general circulation models, J. Atmos. Sci., 43, 505–531, 1986.

Sellers, P., Dickinson, R. E., Randall, D., Betts, A., Hall, F., Berry, J., Collatz, G., Denning, A., Mooney, H., Nobre, C., Sato, N., Field, C. B., and Henderson-Sellers, A.: Modeling the exchanges of energy, water, and carbon between continents and the atmosphere, Science, 275, 502–509, 1997.

Sellers, P. J.: Canopy reflectance, photosynthesis and transpiration, Int. J. Remote Sens., 6, 1335–1372, 1985.

Seneviratne, S. I., Corti, T., Davin, E. L., Hirschi, M., Jaeger, E. B., Lehner, I., Orlowsky, B., and Teuling, A. J.: Investigating soil moisture–climate interactions in a changing climate: A review, Earth-Sci. Rev., 99, 125–161, https://doi.org/10.1016/j.earscirev.2010.02.004, 2010.

Silva, S. J. and Heald, C. L.: Investigating dry deposition of ozone to vegetation, J. Geophys. Res.-Atmos., 123, 559–573, 2018.

Simpson, D., Benedictow, A., Berge, H., Bergström, R., Emberson, L. D., Fagerli, H., Flechard, C. R., Hayman, G. D., Gauss, M., Jonson, J. E., Jenkin, M. E., Nyíri, A., Richter, C., Semeena, V. S., Tsyro, S., Tuovinen, J.-P., Valdebenito, Á., and Wind, P.: The EMEP MSC-W chemical transport model – technical description, Atmos. Chem. Phys., 12, 7825–7865, https://doi.org/10.5194/acp-12-7825-2012, 2012.

Solberg, S., Hov, Ø., Søvde, A., Isaksen, I., Coddeville, P., De Backer, H., Forster, C., Orsolini, Y., and Uhse, K.: European surface ozone in the extreme summer 2003, J. Geophys. Res.-Atmos., 113, D07307, https://doi.org/10.1029/2007JD009098, 2008.

Stella, P., Loubet, B., Lamaud, E., Laville, P., and Cellier, P.: Ozone deposition onto bare soil: a new parameterisation, Agr. Forest Meteorol., 151, 669–681, 2011.

Stella, P., Loubet, B., de Berranger, C., Charrier, X., Ceschia, E., Gerosa, G., Finco, A., Lamaud, E., Serça, D., George, C., and Ciuraru, R.: Soil ozone deposition: Dependence of soil resistance to soil texture, Atmos. Environ., 199, 202–209, 2019.

Stephens, G. L., Li, J., Wild, M., Clayson, C. A., Loeb, N., Kato, S., L'ecuyer, T., Stackhouse, P. W., Lebsock, M., and Andrews, T.: An update on Earth's energy balance in light of the latest global observations, Nat. Geosci., 5, 691–696, https://doi.org/10.1038/NGEO1580, 2012.

Stevens, B. and Schwartz, S. E.: Observing and modeling Earth's energy flows, Surv. Geophys., 33, 779–816, https://doi.org/10.1007/s10712-012-9184-0, 2012.

Sulis, M., Langensiepen, M., Shrestha, P., Schickling, A., Simmer, C., and Kollet, S. J.: Evaluating the influence of plant-specific physiological parameterizations on the partitioning of land surface energy fluxes, J. Hydrometeorol., 16, 517–533, https://doi.org/10.1175/JHM-D-14-0153.1, 2015.

Sun, S., Moravek, A., von der Heyden, L., Held, A., Sörgel, M., and Kesselmeier, J.: Twin-cuvette measurement technique for investigation of dry deposition of O_3 and PAN to plant leaves under controlled humidity conditions, Atmos. Meas. Tech., 9, 599–617, https://doi.org/10.5194/amt-9-599-2016, 2016.

Tuovinen, J.-P., Emberson, L., and Simpson, D.: Modelling ozone fluxes to forests for risk assessment: status and prospects, Ann. Forest Sci., 66, 1–14, https://doi.org/10.1051/forest/2009024, 2009.

Tuzet, A., Perrier, A., Loubet, B., and Cellier, P.: Modelling ozone deposition fluxes: The relative roles of deposition and detoxification processes, Agr. Forest Meteorol., 151, 480–492, https://doi.org/10.1016/j.agrformet.2010.12.004, 2011.

Val Martin, M., Heald, C., and Arnold, S.: Coupling dry deposition to vegetation phenology in the Community Earth System Model: Implications for the simulation of surface O_3, Geophys. Res. Lett., 41, 2988–2996, https://doi.org/10.1002/2014GL059651, 2014.

Van Pul, W. and Jacobs, A.: The conductance of a maize crop and the underlying soil to ozone under various environmental conditions, Bound.-Lay. Meteorol., 69, 83–99, 1994.

Wang, Y., Sperry, J. S., Anderegg, W. R., Venturas, M. D., and Trugman, A. T.: A theoretical and empirical assessment of stomatal optimization modeling, New Phytol., 227, 311–325, https://doi.org/10.1111/nph.16572, 2020.

Wesely, M.: Parameterization of surface resistances to gaseous dry deposition in regional-scale numerical models, Atmos. Environ., 23, 1293–1304, 1989.

Wesely, M. and Hicks, B.: Some factors that affect the deposition rates of sulfur dioxide and similar gases on vegetation, J. Air Pollut. Con. Ass., 27, 1110–1116, 1977.

Wesely, M. and Hicks, B.: A review of the current status of knowledge on dry deposition, Atmos. Environ., 34, 2261–2282, 2000.

Wong, A. Y. H., Geddes, J. A., Tai, A. P. K., and Silva, S. J.: Importance of dry deposition parameterization choice in global simulations of surface ozone, Atmos. Chem. Phys., 19, 14365–14385, https://doi.org/10.5194/acp-19-14365-2019, 2019.

Wu, Z., Staebler, R., Vet, R., and Zhang, L.: Dry deposition of O3 and SO2 estimated from gradient measurements above a temperate mixed forest, Environ. Pollut., 210, 202–210, https://doi.org/10.1016/j.envpol.2015.11.052, 2016.

Wu, Z., Schwede, D. B., Vet, R., Walker, J. T., Shaw, M., Staebler, R., and Zhang, L.: Evaluation and intercomparison of five North American dry deposition algorithms at a mixed forest site, J. Adv. Model. Earth Sy., 10, 1571–1586, https://doi.org/10.1029/2017MS001231, 2018.

Young, P. J., Naik, V., Fiore, A. M., Gaudel, A., Guo, J., Lin, M., Neu, J., Parrish, D., Rieder, H., Schnell, J., Tilmes, S., Wild, O., Zhang, L., Ziemke, J., Brandt, J., Delcloo, A., Doherty, R. M., Geels, C., Hegglin, M. I., Hu, L., Im, U., Kumar, R., Luhar, A., Murray, L., Plummer, D., Rodriguez, J., Saiz-Lopez, A., Schultz, M. G., Woodhouse, M. T., and Zeng, G.: Tropospheric Ozone Assessment Report: Assessment of global-scale model performance for global and regional ozone distributions, variability, and trends, Elem. Sci. Anth., 6, 10, https://doi.org/10.1525/elementa.265, 2018.

Zhang, L., Brook, J. R., and Vet, R.: On ozone dry deposition – with emphasis on non-stomatal uptake and wet canopies, Atmos. Environ., 36, 4787–4799, 2002.

Zhang, L., Brook, J. R., and Vet, R.: A revised parameterization for gaseous dry deposition in air-quality models, Atmos. Chem. Phys., 3, 2067–2082, https://doi.org/10.5194/acp-3-2067-2003, 2003.

Bibliography

Akagi, S. K., Yokelson, R. J., Wiedinmyer, C., Alvarado, M. J., Reid, J. S., Karl, T., Crounse, J. D., and Wennberg, P. O.: Emission factors for open and domestic biomass burning for use in atmospheric models, Atmospheric Chemistry and Physics, 11, 4039–4072, https://doi.org/10.5194/acp-11-4039-2011, 2011.

Altimir, N., Kolari, P., Tuovinen, J.-P., Vesala, T., Bäck, J., Suni, T., Kulmala, M., and Hari, P.: Foliage surface ozone deposition: a role for surface moisture?, Biogeosciences, https://doi.org/10.5194/bg-3-209-2006, 2006.

Amedro, D., Bunkan, A. J. C., Berasategui, M., and Crowley, J. N.: Kinetics of the $OH + NO_2$ reaction: rate coefficients (217–333 K, 16–1200 mbar) and fall-off parameters for N_2 and O_2 bath gases, Atmospheric Chemistry and Physics, 19, 10 643–10 657, https://doi.org/10.5194/acp-19-10643-2019, 2019.

Amedro, D., Berasategui, M., Bunkan, A. J. C., Pozzer, A., Lelieveld, J., and Crowley, J. N.: Kinetics of the $OH + NO_2$ reaction: effect of water vapour and new parameterization for global modelling, Atmospheric Chemistry and Physics, 20, 3091–3105, https://doi.org/10.5194/acp-20-3091-2020, 2020.

Andela, N., Kaiser, J., Heil, A., van Leeuwen, T., Wooster, M., van der Werf, G., Remy, S., and Schultz, M.: Assessment of the Global Fire Assimilation System (GFASv1), ECMWF Technical Memoranda, p. 72, https://doi.org/10.21957/7pg36pe5m, 2013.

Andersson, C. and Engardt, M.: European ozone in a future climate: Importance of changes in dry deposition and isoprene emissions, Journal of Geophysical Research: Atmospheres, 115, https://doi.org/10.1029/2008JD011690, 2010.

Andreae, M. O.: Emission of trace gases and aerosols from biomass burning – an updated assessment, Atmospheric Chemistry and Physics, 19, 8523–8546, https://doi.org/10.5194/acp-19-8523-2019, 2019.

Archer-Nicholls, S., Abraham, N. L., Shin, Y. M., Weber, J., Russo, M. R., Lowe, D., Utembe, S. R., O'Connor, F. M., Kerridge, B., Latter, B., Siddans, R., Jenkin, M., Wild, O., and Archibald, A. T.: The Common Representative Intermediates Mechanism Version 2 in the United Kingdom Chemistry and Aerosols Model, Journal of Advances in Modelling Earth Systems, 13, e2020MS002 420, https://doi.org/10.1029/2020MS002420, 2021.

Barriopedro, D., Fischer, E. M., Luterbacher, J., Trigo, R. M., and García-Herrera, R.: The Hot Summer of 2010: Redrawing the Temperature Record Map of Europe, Science, 332, 220–224, https://doi.org/10.1126/science.1201224, 2011.

Bauwens, M., Stavrakou, T., Müller, J.-F., De Smedt, I., Van Roozendael, M., van der Werf, G. R., Wiedinmyer, C., Kaiser, J. W., Sindelarova, K., and Guenther, A.: Nine years of global hydrocarbon emissions based on source inversion of OMI formaldehyde observations, Atmospheric Chemistry and Physics, 16, 10 133–10 158, https://doi.org/10.5194/acp-16-10133-2016, 2016.

Boynard, A., Hurtmans, D., Koukouli, M. E., Goutail, F., Bureau, J., Safieddine, S., Lerot, C., Hadji-Lazaro, J., Wespes, C., Pommereau, J.-P., et al.: Seven years of IASI ozone retrievals from FORLI: validation with independent total column and vertical profile measurements, Atmospheric Measurement Techniques, https://doi.org/10.5194/amt-2016-11, 2016.

Boynard, A., Hurtmans, D., Garane, K., Goutail, F., Hadji-Lazaro, J., Koukouli, M. E., Wespes, C., Vigouroux, C., Keppens, A., Pommereau, J.-P., Pazmino, A., Balis, D., Loyola, D., Valks, P., Sussmann, R., Smale, D., Coheur, P.-F., and Clerbaux, C.: Validation of the IASI FORLI/EUMETSAT ozone products using satellite (GOME-2), ground-based (Brewer–Dobson, SAOZ, FTIR) and ozonesonde measurements, Atmospheric Measurement Techniques, 11, 5125–5152, https://doi.org/10.5194/amt-11-5125-2018, 2018.

Burkholder, J. B., Sander, S. P., Abbatt, J., Barker, J., Huie, R. E., Kolb, C. E., J.Kurylo, M., Orkin, V. L., Wilmouth, D. M., and Wine, P.: Chemical Kinetics and Photochemical Data for Use in Atmospheric Studies, Evaluation No. 18, JPL Publication 15-10, Jet Propulsion Laboratory, Pasadena, URL `http://jpldataeval.jpl.nasa.gov`, 2015.

Burkholder, J. B., Sander, S. P., J. Abbatt, J. B., C.Cappa, J.D.Crounse, Dibble, T., Huie, R. E., Kolb, C. E., J.Kuryl, M., Orkin, V. L., C.J.Percival, Wilmouth, D. M., and Wine, P.: Chemical Kinetics and Photochemical Data for Use in Atmospheric Studies, Evaluation No. 19, JPL Publication 19-5, Jet Propulsion Laboratory, Pasadena, URL `http://jpldataeval.jpl.nasa.gov`, 2020.

Buszek, R. J., Francisco, J. S., and Anglada, J. M.: Water effects on atmospheric reactions, International Reviews in Physical Chemistry, 30, 335–369, https://doi.org/10.1080/0144235X.2011.634128, 2011.

Butkovskaya, N., Kukui, A., and Le Bras, G.: HNO_3 Forming Channel of the HO_2+NO Reaction as a Function of Pressure and Temperature in the Ranges of 72-600 Torr and 223-323 K, The Journal of Physical Chemistry A, 111, 9047–9053, https://doi.org/10.1021/jp074117m, pMID: 17718462, 2007.

Butkovskaya, N., Rayez, M.-T., Rayez, J.-C., Kukui, A., and Le Bras, G.: Water vapor effect on the HNO_3 yield in the HO_2+NO reaction: experimental and theoretical evidence, The Journal of Physical Chemistry A, 113, 11 327–11 342, https://doi.org/10.1021/jp811428p, 2009.

Butkovskaya, N. I., Kukui, A., Pouvesle, N., and Le Bras, G.: Formation of Nitric Acid in the Gas-Phase HO_2+NO Reaction: Effects of Temperature and Water Vapor, The Journal of Physical Chemistry A, 109, 6509–6520, https://doi.org/10.1021/jp051534v, pMID: 16833996, 2005.

Cabrera-Perez, D., Taraborrelli, D., Sander, R., and Pozzer, A.: Global atmospheric budget of simple monocyclic aromatic compounds, Atmospheric Chemistry and Physics, 16, 6931–6947, https://doi.org/10.5194/acp-16-6931-2016, 2016.

Cao, Y., Yue, X., Liao, H., Yang, Y., Zhu, J., Chen, L., Tian, C., Lei, Y., Zhou, H., and Ma, Y.: Ensemble projection of global isoprene emissions by the end of 21st century using CMIP6 models, Atmospheric Environment, 267, 118 766, https://doi.org/https://doi.org/10.1016/j.atmosenv.2021.118766, 2021.

Cariolle, D., Evans, M. J., Chipperfield, M. P., Butkovskaya, N., Kukui, A., and Le Bras, G.: Impact of the new HNO_3-forming channel of the HO_2+NO reaction on tropospheric HNO_3, NO_x, HO_x and ozone, Atmospheric Chemistry and Physics, 8, 4061–4068, https://doi.org/10.5194/acp-8-4061-2008, 2008.

Clark, J., Call, S. T., Austin, D. E., and Hansen, J. C.: Computational Study of Isoprene Hydroxyalkyl Peroxy Radical-Water Complexes (C5H8 (OH) O2- H2O), The Journal of Physical Chemistry A, 114, 6534–6541, https://doi.org/10.1021/jp102655g, 2010.

Clerbaux, C., Boynard, A., Clarisse, L., George, M., Hadji-Lazaro, J., Herbin, H., Hurtmans, D., Pommier, M., Razavi, A., Turquety, S., Wespes, C., and Coheur, P.-F.: Monitoring of atmospheric composition using the thermal infrared IASI/MetOp sounder, Atmospheric Chemistry and Physics, 9, 6041–6054, https://doi.org/10.5194/acp-9-6041-2009, 2009.

Clifton, O. E., Fiore, A. M., Massman, W. J., Baublitz, C. B., Coyle, M., Emberson, L., Fares, S., Farmer, D. K., Gentine, P., Gerosa, G., Guenther, A. B., Helmig, D., Lombardozzi, D. L., Munger, J. W., Patton, E. G., Pusede, S. E., Schwede, D. B., Silva, S. J., Sörgel, M., Steiner, A. L., and Tai, A. P. K.: Dry Deposition of Ozone Over Land: Processes, Measurement, and Modeling, Reviews of Geophysics, 58, e2019RG000 670, https://doi.org/10.1029/2019RG000670, e2019RG000670 2019RG000670, 2020.

Day, D. A., Dillon, M. B., Wooldridge, P. J., Thornton, J. A., Rosen, R. S., Wood, E. C., and Cohen, R. C.: On alkyl nitrates, O3, and the "missing NOy", Journal of Geophysical Research: Atmospheres, 108, https://doi.org/10.1029/2003JD003685, 2003.

Deckert, R., Jöckel, P., Grewe, V., Gottschaldt, K.-D., and Hoor, P.: A quasi chemistry-transport model mode for EMAC, Geoscientific Model Development, 4, 195, https://doi.org/10.5194/gmd-4-195-2011, 2011.

Delworth, T. L. and Manabe, S.: The influence of potential evaporation on the variabilities of simulated soil wetness and climate, Journal of Climate, 1, 523–547, 1988.

Dietmüller, S., Jöckel, P., Tost, H., Kunze, M., Gellhorn, C., Brinkop, S., Frömming, C., Ponater, M., Steil, B., Lauer, A., and Hendricks, J.: A new radiation infrastructure for the Modular Earth Submodel System (MESSy, based on version 2.51), Geoscientific Model Development, 9, 2209–2222, https://doi.org/10.5194/gmd-9-2209-2016, 2016.

Duncianu, M., Lahib, A., Tomas, A., Stevens, P. S., and Dusanter, S.: Characterization of a chemical amplifier for peroxy radical measurements in the atmosphere, Atmospheric Environment, 222, 117 106, https://doi.org/10.1016/j.atmosenv.2019.117106, 2020.

ECMWF: IFS Documentation CY41R1 - Part IV: Physical Processes, chap. 8, no. 4 in IFS Documentation, ECMWF, https://doi.org/10.21957/p50qmwprw, operational implementation 12 May 2015, 2015.

Emmerichs, T., Kerkweg, A., Ouwersloot, H., Fares, S., Mammarella, I., and Taraborrelli, D.: A revised dry deposition scheme for land–atmosphere exchange of trace gases in ECHAM/MESSy v2.54, Geoscientific Model Development, 14, 495–519, https://doi.org/10.5194/gmd-14-495-2021, 2021.

Emmons, L. K., Walters, S., Hess, P. G., Lamarque, J.-F., Pfister, G. G., Fillmore, D., Granier, C., Guenther, A., Kinnison, D., Laepple, T., Orlando, J., Tie, X., Tyndall, G., Wiedinmyer, C., Baughcum, S. L., and Kloster, S.: Description and evaluation of the Model for Ozone and Related chemical Tracers, version 4 (MOZART-4), Geoscientific Model Development, 3, 43–67, https://doi.org/10.5194/gmd-3-43-2010, 2010.

Fares, S., Weber, R., Park, J.-H., Gentner, D., Karlik, J., and Goldstein, A. H.: Ozone deposition to an orange orchard: Partitioning between stomatal and non-stomatal sinks, Environmental Pollution, 169, 258–266, https://doi.org/10.1016/j.envpol.2012.01.030, 2012.

Ferracci, V., Bolas, C. G., Freshwater, R. A., Staniaszek, Z., King, T., Jaars, K., Otu-Larbi, F., Beale, J., Malhi, Y., Waine, T. W., Jones, R. L., Ashworth, K., and Harris, N. R. P.: Continuous Isoprene Measurements in a UK Temperate Forest for a Whole Growing Season: Effects of Drought Stress During the 2018 Heatwave, Geophysical Research Letters, 47, e2020GL088 885, https://doi.org/10.1029/2020GL088885, 2020.

Fiore, A. M., Jacob, D. J., Bey, I., Yantosca, R. M., Field, B. D., Fusco, A. C., and Wilkinson, J. G.: Background ozone over the United States in summer: Origin, trend, and contribution to pollution episodes, Journal of Geophysical Research: Atmospheres, 107, ACH 11–1–ACH 11–25, https://doi.org/10.1029/2001JD000982, 2002.

Fleming, Z. L., Doherty, R. M., Von Schneidemesser, E., Malley, C. S., Cooper, O. R., Pinto, J. P., Colette, A., Xu, X., Simpson, D., Schultz, M. G., et al.: Tropospheric Ozone Assessment Report: Present-day ozone distribution and trends relevant to human health, Elementa: Science of the Anthropocene, https://doi.org/10.1525/elementa.273, 2018.

Fowler, D., Pilegaard, K., Sutton, M., Ambus, P., Raivonen, M., Duyzer, J., Simpson, D., Fagerli, H., Fuzzi, S., Schjørring, J. K., et al.: Atmospheric composition change: ecosystems–atmosphere interactions, Atmospheric Environment, 43, 5193–5267, 2009.

Franco, B., Blumenstock, T., Cho, C., Clarisse, L., Clerbaux, C., Coheur, P.-F., De Mazière, M., De Smedt, I., Dorn, H.-P., Emmerichs, T., et al.: Ubiquitous atmospheric production of organic acids mediated by cloud droplets, Nature, 593, 233–237, https://doi.org/10.1038/s41586-021-03462-x, 2021.

Ganzeveld, L. and Lelieveld, J.: Dry deposition parameterization in a chemistry general circulation model and its influence on the distribution of reactive trace gases, Journal of Geophysical Research: Atmospheres, 100, 20 999–21 012, 1995.

Ganzeveld, L., Lelieveld, J., Dentener, F., Krol, M., Bouwman, A., and Roelofs, G.-J.: Global soil-biogenic NOx emissions and the role of canopy processes, Journal of Geophysical Research: Atmospheres, 107, 2002.

Gaudel, A., Cooper, O., Ancellet, G., Barret, B., Boynard, A., Burrows, J., Clerbaux, C., Coheur, P.-F., Cuesta, J., Cuevas Agulló, E., et al.: Tropospheric Ozone Assessment Report: Present-day distribution and trends of tropospheric ozone relevant to climate and global atmospheric chemistry model evaluation, Elementa: Science of the Anthropocene, 2018.

Giorgetta, M. A., Roeckner, E., Mauritsen, T., Bader, J., Crueger, T., Esch, M., Rast, S., Kornblueh, L., Schmidt, H., Kinne, S., et al.: The atmospheric general circulation model ECHAM6-model description, 2013.

Gottschaldt, K., Voigt, C., Jöckel, P., Righi, M., Deckert, R., and Dietmüller, S.: Global sensitivity of aviation NO_x effects to the HNO_3-forming channel of the HO_2 + NO reaction, Atmospheric Chemistry and Physics, 13, 3003–3025, https://doi.org/10.5194/acp-13-3003-2013, 2013.

Grewe, V., Brunner, D., Dameris, M., Grenfell, J., Hein, R., Shindell, D., and Staehelin, J.: Origin and variability of upper tropospheric nitrogen oxides and ozone at northern mid-latitudes, Atmospheric Environment, 35, 3421–3433, https://doi.org/10.1016/S1352-2310(01)00134-0, 2001.

Griffiths, P. T., Keeble, J., Shin, Y. M., Abraham, N. L., Archibald, A. T., and Pyle, J. A.: On the Changing Role of the Stratosphere on the Tropospheric Ozone Budget: 1979–2010, Geophysical Research Letters, 47, e2019GL086 901, https://doi.org/https://doi.org/10.1029/2019GL086901, 2020.

Griffiths, P. T., Murray, L. T., Zeng, G., Shin, Y. M., Abraham, N. L., Archibald, A. T., Deushi, M., Emmons, L. K., Galbally, I. E., Hassler, B., Horowitz, L. W., Keeble, J., Liu, J., Moeini, O., Naik, V., O'Connor, F. M., Oshima, N., Tarasick, D., Tilmes, S., Turnock, S. T., Wild, O., Young, P. J., and Zanis, P.: Tropospheric ozone in CMIP6 simulations, Atmospheric Chemistry and Physics, 21, 4187–4218, https://doi.org/10.5194/acp-21-4187-2021, 2021.

Gromov, S., Jöckel, P., Sander, R., and Brenninkmeijer, C. A. M.: A kinetic chemistry tagging technique and its application to modelling the stable isotopic composition of atmospheric trace gases, Geoscientific Model Development, 3, 337–364, https://doi.org/10.5194/gmd-3-337-2010, 2010.

Grote, R., Lavoir, A.-V., Rambal, S., Staudt, M., Zimmer, I., and Schnitzler, J.-P.: Modelling the drought impact on monoterpene fluxes from an evergreen Mediterranean forest canopy, Oecologia, 160, 213–223, https://doi.org/10.1007/s00442-009-1298-9, 2009.

Guenther, A., Hewitt, C. N., Erickson, D., Fall, R., Geron, C., Graedel, T., Harley, P., Klinger, L., Lerdau, M., Mckay, W. A., Pierce, T., Scholes, B., Steinbrecher, R., Tallamraju, R., Taylor, J., and Zimmerman, P.: A global model of natural volatile organic compound emissions, Journal of Geophysical Research: Atmospheres, 100, 8873–8892, https://doi.org/https://doi.org/10.1029/94JD02950, 1995.

Guenther, A., Karl, T., Harley, P., Wiedinmyer, C., Palmer, P., and Geron, C.: Estimates of global terrestrial isoprene emissions using MEGAN (Model of Emissions of Gases and Aerosols from Nature), Atmospheric Chemistry and Physics, 6, 3181–3210, 2006.

Guenther, A. B., Jiang, X., Heald, C. L., Sakulyanontvittaya, T., Duhl, T., Emmons, L. K., and Wang, X.: The Model of Emissions of Gases and Aerosols from Nature version 2.1 (MEGAN2.1): an extended and updated framework for modeling biogenic emissions, Geoscientific Model Development, 5, 1471–1492, https://doi.org/10.5194/gmd-5-1471-2012, 2012.

Hagemann, S. and Stacke, T.: Impact of the soil hydrology scheme on simulated soil moisture memory, Climate Dynamics, 44, 1731–1750, https://doi.org/10.1007/s00382-014-2221-6, 2015.

Hardacre, C., Wild, O., and Emberson, L.: An evaluation of ozone dry deposition in global scale chemistry climate models, Atmospheric Chemistry and Physics, 15, 6419–6436, https://doi.org/10.5194/acp-15-6419-2015, 2015.

Held, I. M. and Soden, B. J.: Robust responses of the hydrological cycle to global warming, Journal of climate, 19, 5686–5699, https://doi.org/10.1175/JCLI3990.1, 2006.

Henrot, A.-J., Stanelle, T., Schröder, S., Siegenthaler, C., Taraborrelli, D., and Schultz, M. G.: Implementation of the MEGAN (v2. 1) biogenic emission model in the ECHAM6-HAMMOZ chemistry climate model, Geoscientific model development, 10, 903–926, https://doi.org/10.5194/gmd-10-903-2017, 2017.

Hens, K., Novelli, A., Martinez, M., Auld, J., Axinte, R., Bohn, B., Fischer, H., Keronen, P., Kubistin, D., Nölscher, A. C., Oswald, R., Paasonen, P., Petäjä, T., Regelin, E., Sander, R., Sinha, V., Sipilä, M., Taraborrelli, D., Tatum Ernest, C., Williams, J., Lelieveld, J., and Harder, H.: Observation and modelling of HO_x radicals in a boreal forest, Atmospheric Chemistry and Physics, 14, 8723–8747, https://doi.org/10.5194/ACP-14-8723-2014, 2014.

Hogg, A., Uddling, J., Ellsworth, D., Carroll, M. A., Pressley, S., Lamb, B., and Vogel, C.: Stomatal and non-stomatal fluxes of ozone to a northern mixed hardwood forest, Tellus B: Chemical and Physical Meteorology, 59, 514–525, https://doi.org/10.1111/j.1600-0889.2007.00269.x, 2007.

Hou, P. and Wu, S.: Long-term changes in extreme air pollution meteorology and the implications for air quality, Scientific reports, 6, 23 792, 2016.

Huang, L., McGaughey, G., McDonald-Buller, E., Kimura, Y., and Allen, D. T.: Quantifying regional, seasonal and interannual contributions of environmental factors on isoprene and monoterpene emissions estimates over eastern Texas, Atmospheric Environment, 106, 120–128, https://doi.org/10.1016/j.atmosenv.2015.01.072, 2015.

Hudman, R. C., Moore, N. E., Mebust, A. K., Martin, R. V., Russell, A. R., Valin, L. C., and Cohen, R. C.: Steps towards a mechanistic model of global soil nitric oxide emissions: implementation and space based-constraints, Atmospheric Chemistry and Physics, 12, 7779–7795, https://doi.org/10.5194/acp-12-7779-2012, 2012.

Hurtmans, D., Coheur, P.-F., Wespes, C., Clarisse, L., Scharf, O., Clerbaux, C., Hadji-Lazaro, J., George, M., and Turquety, S.: FORLI radiative transfer and retrieval code for IASI, Journal of Quantitative Spectroscopy and Radiative Transfer, 113, 1391–1408, https://doi.org/10.1016/j.jqsrt.2012.02.036, 2012.

Iturbide, M., Gutiérrez, J. M., Alves, L. M., Bedia, J., Cerezo-Mota, R., Cimadevilla, E., Cofiño, A. S., Di Luca, A., Faria, S. H., Gorodetskaya, I. V., Hauser, M., Herrera, S., Hennessy, K., Hewitt, H. T., Jones, R. G., Krakovska, S., Manzanas, R., Martínez-Castro, D., Narisma, G. T., Nurhati, I. S., Pinto, I., Seneviratne, S. I., van den Hurk, B., and Vera, C. S.: An update of IPCC climate reference regions for subcontinental analysis of climate model data: definition and aggregated datasets, Earth System Science Data, 12, 2959–2970, https://doi.org/10.5194/essd-12-2959-2020, 2020.

Jarvis, P.: The interpretation of the variations in leaf water potential and stomatal conductance found in canopies in the field, Phil. Trans. R. Soc. Lond. B, 273, 593–610, 1976.

Jeuken, A. B. M., Siegmund, P. C., Heijboer, L. C., Feichter, J., and Bengtsson, L.: On the potential of assimilating meteorological analyses in a global climate model for the purpose of model validation, Journal of Geophysical Research: Atmospheres, 101, 16 939–16 950, https://doi.org/10.1029/96JD01218, 1996.

Jiang, X., Guenther, A., Potosnak, M., Geron, C., Seco, R., Karl, T., Kim, S., Gu, L., and Pallardy, S.: Isoprene emission response to drought and the impact on global atmospheric chemistry, Atmospheric Environment, 183, 69–83, https://doi.org/10.1016/j.atmosenv.2018.01.026, 2018.

Jöckel, P., Sander, R., Kerkweg, A., Tost, H., and Lelieveld, J.: Technical Note: The Modular Earth Submodel System (MESSy) - a new approach towards Earth System Modeling, Atmospheric Chemistry and Physics, 5, 433–444, https://doi.org/10.5194/acp-5-433-2005, 2005.

Jöckel, P., Tost, H., Pozzer, A., Brühl, C., Buchholz, J., Ganzeveld, L., Hoor, P., Kerkweg, A., Lawrence, M. G., Sander, R., Steil, B., Stiller, G., Tanarhte, M., Taraborrelli, D., van Aardenne, J., and Lelieveld, J.: The atmospheric chemistry general circulation model ECHAM5/MESSy1: consistent simulation of ozone from the surface to the mesosphere, Atmospheric Chemistry and Physics, 6, 5067–5104, https://doi.org/10.5194/acp-6-5067-2006, 2006.

Jöckel, P., Kerkweg, A., Buchholz-Dietsch, J., Tost, H., Sander, R., and Pozzer, A.: Technical Note: Coupling of chemical processes with the Modular Earth Submodel System (MESSy) submodel TRACER, Atmospheric Chemistry and Physics, 8, 1677–1687, https://doi.org/10.5194/acp-8-1677-2008, 2008.

Jöckel, P., Kerkweg, A., Pozzer, A., , R., Tost, H., Riede, H., Baumgaertner, A., Gromov, S., and Kern, B.: Development cycle 2 of the modular earth submodel system (MESSy2), Geoscientific Model Development, 3, 717–752, https://doi.org/10.5194/gmd-3-717-2010, 2010.

Jöckel, P., Tost, H., Pozzer, A., Kunze, M., Kirner, O., Brenninkmeijer, C. A. M., Brinkop, S., Cai, D. S., Dyroff, C., Eckstein, J., Frank, F., Garny, H., Gottschaldt, K.-D., Graf, P., Grewe, V., Kerkweg, A., Kern, B., Matthes, S., Mertens, M., Meul, S., Neumaier, M., Nützel, M., Oberländer-Hayn, S., Ruhnke, R., Runde, T., Sander, R., Scharffe, D., and Zahn, A.: Earth System Chemistry integrated Modelling (ESCiMo) with the Modular Earth Submodel System (MESSy) version 2.51, Geoscientific Model Development, 9, 1153–1200, https://doi.org/10.5194/gmd-9-1153-2016, 2016.

Jülich Supercomputing Centre: JURECA: Modular supercomputer at Jülich Supercomputing Centre, Journal of large-scale research facilities, 4, https://doi.org/10.17815/jlsrf-4-121-1, 2018.

Kaiser, J. W., Heil, A., Andreae, M. O., Benedetti, A., Chubarova, N., Jones, L., Morcrette, J.-J., Razinger, M., Schultz, M. G., Suttie, M., and van der Werf, G. R.: Biomass burning emissions estimated with a global fire assimilation system based

on observed fire radiative power, Biogeosciences, 9, 527–554, https://doi.org/10.5194/bg-9-527-2012, 2012.

Karl, T., Harley, P., Emmons, L., Thornton, B., Guenther, A., Basu, C., Turnipseed, A., and Jardine, K.: Efficient atmospheric cleansing of oxidized organic trace gases by vegetation, Science, 330, 816–819, https://doi.org/10.1126/science.1192534, 2010.

Katul, G. G., Palmroth, S., and Oren, R.: Leaf stomatal responses to vapour pressure deficit under current and CO_2-enriched atmosphere explained by the economics of gas exchange, Plant, Cell & Environment, 32, 968–979, https://doi.org/10.1111/j.1365-3040.2009.01977.x, 2009.

Kerkweg, A., Buchholz, J., Ganzeveld, L., Pozzer, A., Tost, H., and Jöckel, P.: An implementation of the dry removal processes DRY DEPosition and SEDImentation in the Modular Earth Submodel System (MESSy), Atmospheric Chemistry and Physics, 6, 4617–4632, https://doi.org/10.5194/acp-6-4617-2006, 2006a.

Kerkweg, A., Sander, R., Tost, H., and Jöckel, P.: Technical note: Implementation of prescribed (OFFLEM), calculated (ONLEM), and pseudo-emissions (TNUDGE) of chemical species in the Modular Earth Submodel System (MESSy), Atmospheric Chemistry and Physics, 6, 3603–3609, https://doi.org/10.5194/acp-6-3603-2006, 2006b.

Khan, M., Cooke, M., Utembe, S., Morris, W., Archibald, A., Derwent, R., Jenkin, M., Orr-Ewing, A., Higgins, C., Percival, C., Leather, K., and Shallcross, D.: Global modeling of the C1–C3 alkyl nitrates using STOCHEM-CRI, Atmospheric Environment, 123, 256–267, https://doi.org/https://doi.org/10.1016/j.atmosenv.2015.10.088, 2015.

Klingmüller, K., Metzger, S., Abdelkader, M., Karydis, V., Stenchikov, G. L., Pozzer, A., and Lelieveld, J.: Revised mineral dust emissions in the atmospheric chemistry-climate model EMAC (based on MESSy 2.52), Geoscientific Model Development, https://doi.org/10.5194/gmd-11-989-2018, 2017.

Koppmann, R.: Volatile organic compounds in the atmosphere, John Wiley & Sons, https://doi.org/10.1002/9780470988657, 2008.

Krol, M., Peters, W., Hooghiemstra, P., George, M., Clerbaux, C., Hurtmans, D., McInerney, D., Sedano, F., Bergamaschi, P., El Hajj, M., Kaiser, J. W., Fisher, D., Yershov, V., and Muller, J.-P.: How much CO was emitted by the 2010 fires around Moscow?, Atmospheric Chemistry and Physics, 13, 4737–4747, https://doi.org/10.5194/acp-13-4737-2013, 2013.

Kumbhani, S. R., Cline, T. S., Killian, M. C., Clark, J. M., Keeton, W. J., Hansen, L. D., Shirts, R. B., Robichaud, D. J., and Hansen, J. C.: Water Vapor Enhancement of Rates of Peroxy Radical Reactions, International Journal of Chemical Kinetics, 47, 395–409, https://doi.org/10.1002/kin.20917, 2015.

Lamarque, J.-F., Bond, T. C., Eyring, V., Granier, C., Heil, A., Klimont, Z., Lee, D., Liousse, C., Mieville, A., Owen, B., Schultz, M. G., Shindell, D., Smith, S. J., Stehfest, E., Van Aardenne, J., Cooper, O. R., Kainuma, M., Mahowald, N., McConnell, J. R., Naik, V., Riahi, K., and van Vuuren, D. P.: Historical (1850–2000) gridded anthropogenic and biomass burning emissions of reactive gases and aerosols: methodology and application, Atmospheric Chemistry and Physics, 10, 7017–7039, https://doi.org/10.5194/acp-10-7017-2010, 2010.

Lelieveld, J., Gromov, S., Pozzer, A., and Taraborrelli, D.: Global tropospheric hydroxyl distribution, budget and reactivity, Atmospheric Chemistry and Physics, 16, 12 477, https://doi.org/10.5194/acp-2016-160, 2016.

Li, W. and Fu, R.: Transition of the large-scale atmospheric and land surface conditions from the dry to the wet season over Amazonia as diagnosed by the ECMWF re-analysis, Journal of Climate, 17, 2637–2651, https://doi.org/10.1175/1520-0442(2004)017<2637:TOTLAA>2.0.CO;2, 2004.

Liao, H. and Seinfeld, J. H.: Global impacts of gas-phase chemistry-aerosol interactions on direct radiative forcing by anthropogenic aerosols and ozone, Journal of Geophysical Research: Atmospheres, 110, https://doi.org/https://doi.org/10.1029/2005JD005907, 2005.

Lin, S.-J. and Rood, R. B.: Multidimensional Flux-Form Semi-Lagrangian Transport Schemes, Monthly Weather Review, 124, 2046–2070, 1996.

Lu, Y.-S.: Propagation of land surface model uncertainties in simulated terrestrial system states, Bonner Meteorologische Abhandlungen, 2018.

Mauritsen, T., Stevens, B., Roeckner, E., Crueger, T., Esch, M., Giorgetta, M., Haak, H., Jungclaus, J., Klocke, D., Matei, D., et al.: Tuning the climate of a global model, Journal of advances in modeling Earth systems, 4, https://doi.org/10.1029/2012MS000154, 2012.

Monks, P. S.: Gas-phase radical chemistry in the troposphere, Chemical Society Reviews, 34, 376–395, https://doi.org/10.1039/B307982C, 2005.

Monks, P. S., Archibald, A. T., Colette, A., Cooper, O., Coyle, M., Derwent, R., Fowler, D., Granier, C., Law, K. S., Mills, G. E., Stevenson, D. S., Tarasova, O., Thouret, V., von Schneidemesser, E., Sommariva, R., Wild, O., and Williams, M. L.: Tropospheric ozone and its precursors from the urban to the global scale from air quality to short-lived climate forcer, Atmospheric Chemistry and Physics, 15, 8889–8973, https://doi.org/10.5194/acp-15-8889-2015, 2015.

Myhre, G., Shindell, D., Bréon, F., Collins, W., Fuglestvedt, J., Huang, J., Koch, D., Lamarque, J., Lee, D., Mendoza, B., et al.: Anthropogenic and Natural Radiative Forcing, in: Climate Change 2013 – The Physical Science Basis: Working Group I Contribution to the Fifth Assessment Report of the Intergovernmental Panel on Climate Change, p. 659–740, Cambridge University Press, https://doi.org/10.1017/CBO9781107415324.018, 2014.

Myriokefalitakis, S., Daskalakis, N., Gkouvousis, A., Hilboll, A., van Noije, T., Williams, J. E., Le Sager, P., Huijnen, V., Houweling, S., Bergman, T., Nüß, J. R., Vrekoussis, M., Kanakidou, M., and Krol, M. C.: Description and evaluation of a detailed gas-phase chemistry scheme in the TM5-MP global chemistry transport model (r112), Geoscientific Model Development, 13, 5507–5548, https://doi.org/10.5194/gmd-13-5507-2020, 2020.

Nguyen, T. B., Crounse, J. D., Teng, A. P., Clair, J. M. S., Paulot, F., Wolfe, G. M., and Wennberg, P. O.: Rapid deposition of oxidized biogenic compounds to a temperate forest, Proceedings of the National Academy of Sciences, 112, E392–E401, 2015.

Nölscher, A., Butler, T., Auld, J., Veres, P., Muñoz, A., Taraborrelli, D., Vereecken, L., Lelieveld, J., and Williams, J.: Using total OH reactivity to assess isoprene photooxidation via measurement and model, Atmos. Environ., 89, 453–463, https://doi.org/10.1016/j.atmosenv.2014.02.024, 2014.

O'Gorman, P. A. and Schneider, T.: The physical basis for increases in precipitation extremes in simulations of 21st-century climate change, Proceedings of the National Academy of Sciences, 106, 14 773–14 777, https://doi.org/10.1073/pnas.0907610106, 2009.

Paton-Walsh, C., Emmerson, K. M., Garland, R. M., Keywood, M., Hoelzemann, J. J., Huneeus, N., Buchholz, R. R., Humphries, R. S., Altieri, K., Schmale, J., Wilson, S. R., Labuschagne, C., Kalisa, E., Fisher, J. A., Deutscher, N. M., van Zyl, P. G., Beukes, J. P., Joubert, W., Martin, L., Mkololo, T., Barbosa, C., de Fatima Andrade, M., Schofield, R., Mallet, M. D., Harvey, M. J., Formenti, P., Piketh, S. J., and Olivares, G.: Key challenges for tropospheric chemistry in the Southern Hemisphere, Elementa: Science of the Anthropocene, 10, https://doi.org/10.1525/elementa.2021.00050, 00050, 2022.

Pegoraro, E., Rey, A., Greenberg, J., Harley, P., Grace, J., Malhi, Y., and Guenther, A.: Effect of drought on isoprene emission rates from leaves of Quercus virginiana Mill., Atmospheric Environment, 38, 6149–6156, https://doi.org/10.1016/j.atmosenv.2004.07.028, 2004.

Porter, W. C. and Heald, C. L.: The mechanisms and meteorological drivers of the summertime ozone–temperature relationship, Atmospheric Chemistry and Physics, 19, 13 367–13 381, https://doi.org/10.5194/acp-19-13367-2019, 2019.

Pozzer, A., Jöckel, P., Sander, R., Williams, J., Ganzeveld, L., and Lelieveld, J.: Technical Note: The MESSy-submodel AIRSEA calculating the air-sea exchange of chemical species, Atmospheric Chemistry and Physics, 6, 5435–5444, https://doi.org/10.5194/acp-6-5435-2006, 2006.

Pozzer, A., Jöckel, P., and Van Aardenne, J.: The influence of the vertical distribution of emissions on tropospheric chemistry, Atmospheric Chemistry and Physics, 9, 9417–9432, https://doi.org/10.5194/acp-9-9417-2009, 2009.

Pozzer, A., de Meij, A., Pringle, K. J., Tost, H., Doering, U. M., van Aardenne, J., and Lelieveld, J.: Distributions and regional budgets of aerosols and their precursors simulated with the EMAC chemistry-climate model, Atmospheric Chemistry and Physics, 12, 961–987, https://doi.org/10.5194/acp-12-961-2012, 2012.

Pusede, S. E., Steiner, A. L., and Cohen, R. C.: Temperature and recent trends in the chemistry of continental surface ozone, Chemical reviews, 115, 3898–3918, 2015.

Ramo, R., Roteta, E., Bistinas, I., van Wees, D., Bastarrika, A., Chuvieco, E., and van der Werf, G. R.: African burned area and fire carbon emissions are strongly impacted by small fires undetected by coarse resolution satellite data, Proceedings of the National Academy of Sciences, 118, https://doi.org/10.1073/pnas.2011160118, 2021.

Ran, L., Pleim, J., Song, C., Band, L., Walker, J. T., and Binkowski, F. S.: A photosynthesis-based two-leaf canopy stomatal conductance model for meteorology and air quality modeling with WRF/CMAQ PX LSM, Journal of Geophysical Research: Atmospheres, 122, 1930–1952, https://doi.org/https://doi.org/10.1002/2016JD025583, 2017.

Rannik, Ü., Altimir, N., Mammarella, I., Bäck, J., Rinne, J., Ruuskanen, T., Hari, P., Vesala, T., and Kulmala, M.: Ozone deposition into a boreal forest over a decade of observations: evaluating deposition partitioning and driving variables, Atmospheric Chemistry and Physics, 12, 12 165–12 182, https://doi.org/10.5194/acp-12-12165-2012, 2012.

Rannik, Ü., Peltola, O., and Mammarella, I.: Random uncertainties of flux measurements by the eddy covariance technique, Atmospheric Measurement Techniques, 9, 5163, https://doi.org/0.5194/amt-9-5163-2016, 2016.

Ridder, N., Ukkola, A., Pitman, A., and Perkins-Kirkpatrick, S.: Increased occurrence of high impact compound events under climate change, npj Climate and Atmospheric Science, 5, 1–8, https://doi.org/10.1038/s41612-021-00224-4, 2022.

Righi, M., Eyring, V., Gottschaldt, K.-D., Klinger, C., Frank, F., Jöckel, P., and Cionni, I.: Quantitative evaluation of ozone and selected climate parameters in a set of EMAC simulations, Geoscientific Model Development, 8, 733–768, https://doi.org/10.5194/gmd-8-733-2015, 2015.

Rodgers, C. D.: Inverse Methods for Atmospheric Sounding, WORLD SCIENTIFIC, https://doi.org/10.1142/3171, 2000.

Roeckner, E., Bäuml, G., Bonaventura, L., Brokopf, R., Esch, M., Giorgetta, M., Hagemann, S., Kirchner, I., Kornblueh, L., Manzini, E., et al.: The atmospheric general circulation model ECHAM 5. PART I: Model description, MPI report, 2003.

Roeckner, E., Brokopf, R., Esch, M., Giorgetta, M., Hagemann, S., Kornblueh, L., Manzini, E., Schlese, U., and Schulzweida, U.: Sensitivity of simulated climate to horizontal and vertical resolution in the ECHAM5 atmosphere model, Journal of Climate, 19, 3771–3791, https://doi.org/10.1175/JCLI3824.1, 2006.

Rosanka, S., Franco, B., Clarisse, L., Coheur, P.-F., Wahner, A., and Taraborrelli, D.: Organic pollutants from tropical peatland fires: regional influences and its impact on lower stratospheric ozone, Atmospheric Chemistry and Physics Discussions, 2020, 1–41, https://doi.org/10.5194/acp-2020-1130, 2020.

Rosanka, S., Sander, R., Wahner, A., and Taraborrelli, D.: Oxidation of low-molecular-weight organic compounds in cloud droplets: development of the Jülich Aqueous-phase Mechanism of Organic Chemistry (JAMOC) in CAABA/MECCA (version 4.5.0), Geoscientific Model Development, 14, 4103–4115, https://doi.org/10.5194/gmd-14-4103-2021, 2021a.

Rosanka, S., Sander, R., Franco, B., Wespes, C., Wahner, A., and Taraborrelli, D.: Oxidation of low-molecular-weight organic compounds in cloud droplets: global impact on tropospheric oxidants, Atmospheric Chemistry and Physics, 21, 9909–9930, https://doi.org/10.5194/acp-21-9909-2021, 2021b.

Sadiq, M., Tai, A. P. K., Lombardozzi, D., and Val Martin, M.: Effects of ozone–vegetation coupling on surface ozone air quality via biogeochemical and meteorological feedbacks, Atmospheric Chemistry and Physics, 17, 3055–3066, https://doi.org/10.5194/acp-17-3055-2017, 2017.

Sander, R., Baumgaertner, A., Cabrera-Perez, D., Frank, F., Gromov, S., Grooß, J.-U., Harder, H., Huijnen, V., Jöckel, P., Karydis, V. A., et al.: The community atmospheric chemistry box model CAABA/MECCA-4.0, Geoscientific model development, 12, 1365–1385, https://doi.org/10.5194/gmd-12-1365-2019, 2019.

Sander, S. P., Finlayson-Pitts, B. J., Friedl, R. R., Golden, D. M., Huie, R. E., Kolb, C. E., Kurylo, M. J., Molina, M. J., Moortgat, G. K., Orkin, V. L., and Ravishankara, A. R.: Chemical Kinetics and Photochemical Data for Use in Atmospheric Studies, Evaluation Number 14, JPL Publication 02-25, Jet Propulsion Laboratory, Pasadena, CA, URL `http://jpldataeval.jpl.nasa.gov`, 2003.

Schultz, M. G., Schröder, S., Lyapina, O., Cooper, O., Galbally, I., Petropavlovskikh, I., Von Schneidemesser, E., Tanimoto, H., Elshorbany, Y., Naja, M., et al.: Tropospheric Ozone Assessment Report: Database and metrics data of global surface ozone observations, Elementa: Science of the Anthropocene, https://doi.org/10.1525/elementa.244, 2017.

Schulz, J.-P., Dümenil, L., and Polcher, J.: On the land surface–atmosphere coupling and its impact in a single-column atmospheric model, Journal of Applied Meteorology, 40, 642–663, https://doi.org/10.1175/1520-0450(2001)040<0642:OTLSAC>2.0.CO;2, 2001.

Seinfeld, J. H. and Pandis, S. N.: Atmospheric chemistry and physics: from air pollution to climate change, John Wiley & Sons, 2016.

Sellers, P. J.: Canopy reflectance, photosynthesis and transpiration, International Journal of Remote Sensing, 6, 1335–1372, https://doi.org/10.1080/01431168508948283, 1985.

Shepherd, T. G., Boyd, E., Calel, R. A., Chapman, S. C., Dessai, S., Dima-West, I. M., Fowler, H. J., James, R., Maraun, D., Martius, O., et al.: Storylines: an alternative approach to representing uncertainty in physical aspects of climate change, Climatic change, 151, 555–571, https://doi.org/10.1007/s10584-018-2317-9, 2018.

Sherwen, T., Evans, M. J., Carpenter, L. J., Andrews, S. J., Lidster, R. T., Dix, B., Koenig, T. K., Sinreich, R., Ortega, I., Volkamer, R., Saiz-Lopez, A., Prados-Roman, C., Mahajan, A. S., and Ordonez, C.: Iodine's impact on tropospheric oxidants: a global model study in GEOS-Chem, Atmospheric Chemistry and Physics, 16, 1161–1186, https://doi.org/10.5194/acp-16-1161-2016, 2016.

Simpson, D., Benedictow, A., Berge, H., Bergström, R., Emberson, L. D., Fagerli, H., Flechard, C. R., Hayman, G. D., Gauss, M., Jonson, J. E., Jenkin, M. E., Nyíri, A., Richter, C., Semeena, V. S., Tsyro, S., Tuovinen, J.-P., Valdebenito, A., and Wind, P.: The EMEP MSC-W chemical transport model; technical description, Atmospheric Chemistry and Physics, 12, 7825–7865, https://doi.org/10.5194/acp-12-7825-2012, 2012.

Sindelarova, K., Granier, C., Bouarar, I., Guenther, A., Tilmes, S., Stavrakou, T., Muller, J.-F., Kuhn, U., Stefani, P., and Knorr, W.: Global data set of biogenic VOC emissions calculated by the MEGAN model over the last 30 years, Atmospheric Chemistry and Physics, 14, 9317–9341, https://doi.org/10.5194/acp-14-9317-2014, 2014.

Solazzo, E., Crippa, M., Guizzardi, D., Muntean, M., Choulga, M., and Janssens-Maenhout, G.: Uncertainties in the Emissions Database for Global Atmospheric Research (EDGAR) emission inventory of greenhouse gases, Atmospheric Chemistry and Physics, 21, 5655–5683, https://doi.org/10.5194/acp-21-5655-2021, 2021.

Steinkamp, J., Ganzeveld, L. N., Wilcke, W., and Lawrence, M. G.: Influence of modelled soil biogenic NO emissions on related trace gases and the atmospheric oxidizing efficiency, Atmospheric Chemistry and Physics, 9, 2663–2677, https://doi.org/10.5194/acp-9-2663-2009, 2009.

Stella, P., Loubet, B., Lamaud, E., Laville, P., and Cellier, P.: Ozone deposition onto bare soil: a new parameterisation, Agricultural and Forest Meteorology, 151, 669–681, 2011.

Su, H., Cheng, Y., Oswald, R., Behrendt, T., Trebs, I., Meixner, F. X., Andreae, M. O., Cheng, P., Zhang, Y., and Pöschl, U.: Soil Nitrite as a Source of Atmospheric HONO and OH Radicals, Science, 333, 1616–1618, https://doi.org/10.1126/science.1207687, 2011.

Taraborrelli, D., Lawrence, M. G., Butler, T. M., Sander, R., and Lelieveld, J.: Mainz Isoprene Mechanism 2 (MIM2): an isoprene oxidation mechanism for regional and global atmospheric modelling, Atmospheric Chemistry and Physics, 9, 2751–2777, https://doi.org/10.5194/ACP-9-2751-2009, 2009.

Taraborrelli, D., Lawrence, M. G., Crowley, J. N., Dillon, T. J., Gromov, S., Groß, C. B. M., Vereecken, L., and Lelieveld, J.: Hydroxyl radical buffered by isoprene oxidation over tropical forests, Nature Geosci., 5, 190–193, https://doi.org/10.1038/NGEO1405, 2012.

Taraborrelli, D., Cabrera-Perez, D., Bacer, S., Gromov, S., Lelieveld, J., Sander, R., and Pozzer, A.: Influence of aromatics on tropospheric gas-phase composition, Atmospheric Chemistry and Physics, 21, 2615–2636, https://doi.org/10.5194/acp-21-2615-2021, 2021.

Tarasick, D. W., Galbally, I. E., Cooper, O. R., Schultz, M., Ancellet, G., Leblanc, T., Wallington, T. J., Ziemke, J., Xiong, L., Steinbacher, M., et al.: Tropospheric Ozone Assessment Report: Tropospheric ozone from 1877 to 2016, observed levels, trends and uncertainties, Elementa: Science of the Anthropocene, https://doi.org/10.1525/elementa.376, 2019.

Tawfik, A. B. and Steiner, A. L.: A proposed physical mechanism for ozone-meteorology correlations using land–atmosphere coupling regimes, Atmospheric Environment, 72, 50–59, https://doi.org/10.1016/j.atmosenv.2013.03.002, 2013.

Tost, H.: Global Modelling of Cloud, Convection and Precipitation Influences on Trace Gases and Aerosols, Ph.D. thesis, Rheinische Friedrich-Wilhelms-Universität Bonn, 2006.

Tost, H., Jöckel, P., Kerkweg, A., Sander, R., and Lelieveld, J.: Technical note: A new comprehensive SCAVenging submodel for global atmospheric chemistry modelling, Atmospheric Chemistry and Physics, 6, 565–574, https://doi.org/10.5194/acp-6-565-2006, 2006a.

Tost, H., Jöckel, P., and Lelieveld, J.: Influence of different convection parameterisations in a GCM, Atmospheric Chemistry and Physics, 6, 5475–5493, https://doi.org/10.5194/acp-6-5475-2006, 2006b.

Tost, H., Jöckel, P., and Lelieveld, J.: Lightning and convection parameterisations - uncertainties in global modelling, Atmospheric Chemistry and Physics, 7, 4553–4568, https://doi.org/10.5194/acp-7-4553-2007, 2007.

Vinken, G. C. M., Boersma, K. F., Maasakkers, J. D., Adon, M., and Martin, R. V.: Worldwide biogenic soil NO_x emissions inferred from OMI NO_2 observations, Atmospheric Chemistry and Physics, 14, 10 363–10 381, https://doi.org/10.5194/acp-14-10363-2014, 2014.

Wang, J., Ge, B., and Wang, Z.: Ozone production efficiency in highly polluted environments, Current Pollution Reports, 4, 198–207, https://doi.org/10.1007/s40726-018-0093-9, 2018.

Wells, K. C., Millet, D. B., Payne, V. H., Deventer, M. J., Bates, K. H., de Gouw, J. A., Graus, M., Warneke, C., Wisthaler, A., and Fuentes, J. D.: Satellite isoprene retrievals constrain emissions and atmospheric oxidation, Nature, 585, 225–233, https://doi.org/10.1038/s41586-020-2664-3, 2020.

Weng, H., Lin, J., Martin, R., Millet, D. B., Jaeglé, L., Ridley, D., Keller, C., Li, C., Du, M., and Meng, J.: Global high-resolution emissions of soil NO x, sea salt aerosols, and biogenic volatile organic compounds, Scientific Data, 7, 1–15, https://doi.org/10.1038/s41597-020-0488-5, 2020.

Wesely, M.: Parameterization of surface resistances to gaseous dry deposition in regional-scale numerical models, Atmospheric Environment (1967), 23, 1293–1304, https://doi.org/10.1016/0004-6981(89)90153-4, 1989.

Wesely, M. and Hicks, B.: A review of the current status of knowledge on dry deposition, Atmospheric environment, 34, 2261–2282, https://doi.org/10.1016/S1352-2310(99)00467-7, 2000.

Wespes, C., Hurtmans, D., Clerbaux, C., and Coheur, P.-F.: O3 variability in the troposphere as observed by IASI over 2008–2016: Contribution of atmospheric chemistry and dynamics, Journal of Geophysical Research: Atmospheres, 122, 2429–2451, https://doi.org/10.1002/2016JD025875, 2017.

Whitehouse, L. E., Tomlin, A. S., and Pilling, M. J.: Systematic reduction of complex tropospheric chemical mechanisms, Part II: Lumping using a time-scale based approach, Atmospheric Chemistry and Physics, 4, 2057–2081, https://doi.org/10.5194/acp-4-2057-2004, 2004.

Wiedinmyer, C., Akagi, S. K., Yokelson, R. J., Emmons, L. K., Al-Saadi, J. A., Orlando, J. J., and Soja, A. J.: The Fire INventory from NCAR (FINN): a high resolution global model to estimate the emissions from open burning, Geoscientific Model Development, 4, 625–641, https://doi.org/10.5194/gmd-4-625-2011, 2011.

Wong, A. Y. H., Geddes, J. A., Tai, A. P. K., and Silva, S. J.: Importance of dry deposition parameterization choice in global simulations of surface ozone, Atmospheric Chemistry and Physics, 19, 14 365–14 385, https://doi.org/10.5194/acp-19-14365-2019, URL `https://acp.copernicus.org/articles/19/14365/2019/`, 2019.

Wu, Z., Staebler, R., Vet, R., and Zhang, L.: Dry deposition of O3 and SO2 estimated from gradient measurements above a temperate mixed forest, Environmental pollution, 210, 202–210, https://doi.org/10.1016/j.envpol.2015.11.052, 2016.

Xing, Y., Li, H., Huang, L., Wu, H., Shen, H., and Chen, Z.: The production of formaldehyde and hydroxyacetone in methacrolein photooxidation: New insights into mechanism and effects of water vapor, Journal of Environmental Sciences, 66, 1–11, https://doi.org/10.1016/j.jes.2017.05.037, 2018.

Yan, Y., Lin, J., Chen, J., and Hu, L.: Improved simulation of tropospheric ozone by a global-multi-regional two-way coupling model system, Atmospheric Chemistry and Physics, 16, 2381–2400, https://doi.org/10.5194/acp-16-2381-2016, 2016.

Yang, W., Yuan, H., Han, C., Yang, H., and Xue, X.: Photochemical emissions of HONO, NO_2 and NO from the soil surface under simulated sunlight, Atmospheric Environment, 234, 117 596, https://doi.org/10.1016/j.atmosenv.2020.117596, 2020.

Yienger, J. and Levy II, H.: Empirical model of global soil-biogenic NO_x emissions, J. Geophys. Res., 100, 464, https://doi.org/10.1029/95JD00370, 1995.

Young, P., Archibald, A., Bowman, K., Lamarque, J.-F., Naik, V., Stevenson, D., Tilmes, S., Voulgarakis, A., Wild, O., Bergmann, D., et al.: Pre-industrial to end 21st century projections of tropospheric ozone from the Atmospheric Chemistry and Climate Model Intercomparison Project (ACCMIP), Atmospheric Chemistry and Physics, 13, 2063–2090, https://doi.org/10.5194/acp-13-2063-2013, 2013.

Young, P. J., Arneth, A., Schurgers, G., Zeng, G., and Pyle, J. A.: The CO_2 inhibition of terrestrial isoprene emission significantly affects future ozone projections, Atmospheric Chemistry and Physics, 9, 2793–2803, https://doi.org/10.5194/acp-9-2793-2009, 2009.

Young, P. J., Naik, V., Fiore, A. M., Gaudel, A., Guo, J., Lin, M., Neu, J., Parrish, D., Rieder, H., Schnell, J., et al.: Tropospheric Ozone Assessment Report: Assessment of global-scale model performance for global and regional ozone distributions, variability, and trends, Elem Sci Anth, 6, https://doi.org/10.1525/elementa.265, 2018.

Zhang, L., Brook, J. R., and Vet, R.: On ozone dry deposition–with emphasis on non-stomatal uptake and wet canopies, Atmospheric Environment, 36, 4787–4799, https://doi.org/10.1016/S1352-2310(02)00567-8, 2002.

Acknowledgements

General

The work described in this thesis has received funding from the Initiative and Networking Fund of the Helmholtz Association through the project "Advanced Earth System Modelling Capacity (ESM)". The content of this work is the sole responsibility of the author and it does not represent the opinion of the Helmholtz Association, and the Helmholtz Association is not responsible for any use that might be made of the information contained.

The author gratefully acknowledges the computing time granted through JARA-HPC on the supercomputer Jülich Research on Exascale Cluster Architectures (JURECA, Jülich Supercomputing Centre, 2018) at Forschungszentrum Jülich.

Personal

In particular, I'm very thankful to Domenico Taraborrelli for these three years of great supervision, which shaped my research. I value his support and positive criticism, especially the time for teaching me and many fruitful discussions. He always had an open door for me and an open mind for my ideas.

I would especially thank Prof. Andreas Bott for supervising my work at university Bonn, his interest in my work, his dedicated time and all his support. I would like to thank Prof. Andreas Wahner for offering me the opportunity to pursue this work, for his support, and for accepting to act as a referee. I would like to thank Prof. Astrid Kiendler-Scharr for offering me the opportunity to pursue this work, for her support, and for establishing the connection to Jaana Bäck.

I am very thankful to the co-authors of the study on dry deposition. Furthermore, I would like to thank Bruno Franco and Catherine Wespes for preparing the IASI retrievals and for further discussions on this. For using the TOAR data, I want to gratefully acknowledge the work of Martin Schultz and his team. Many thanks go to my colleagues Simon Rosanka, Astrid Kerkweg and Yen-Sen Lu for supporting my work with technical/scientific advice and interesting discussions. A special thanks go to Simon Rosanka who provided me with his script for calculating the odd oxygen budget.

Many thanks to my friends for their sympathy and motivating conversations. A special thanks go to my twin sister Yvonne for her belief in me, for her support and

the capability to open my eyes to solutions. In particular, I'm deeply grateful to my parents, who always carry me through stressful times, give me the confidence to follow my interests and encourage me to tackle challenges that ultimately let me step into the field of atmospheric sciences.